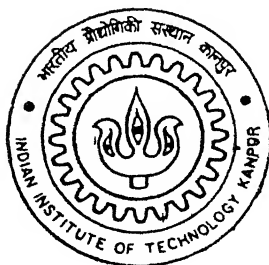# EXPERIMENTAL CHARACTERIZATION OF UNHEATED AND HEATED BLUFF BODY WAKES

By

SUSHANTA DUTTA
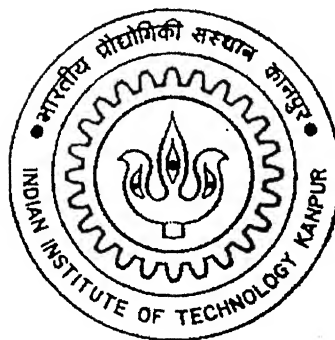
DEPARTMENT OF MECHANICAL ENGINEERING

Indian Institute of Technology Kanpur
DECEMBER, 2001

EXPERIMENTAL CHARACTERIZATION OF UNHEATED AND HEATED BLUFF BODY WAKES

A THESIS SUBMITTED
IN PARTIAL FULFILMENT OF THE REQUIREMENTS
FOR THE DEGREE OF
MASTER OF TECHNOLOGY

by
SUSHANTA DUTTA

DEPARTMENT OF MECHANICAL ENGINEERING
INDIAN INSTITUTE OF TECHNOLOGY KANPUR
December 2001

CERTIFICATE

It is certified that the work contained in the thesis entitled *"Experimental Characterization of Unheated and Heated Bluff Body Wakes"*, by *Mr. Sushanta Dutta*, has been carried out under our supervision and that this work has not been submitted elsewhere for a degree.

Dr. K. Muralidhar
Dept. of Mechanical Engineering
I.I.T. Kanpur 208016

Dr. P. K. Panigrahi
Dept. of Mechanical Engineering
I.I.T Kanpur 208016

December, 2001

Abstract

This work reports the experimental results of flow behind heated and unheated bluff bodies. A square cylinder is used for the unheated bluff body case and a constant temperature circular cylinder is used for the heated bluff body case. Constant Temperature Hotwire Anemometry is primarily used for the unheated bluff body investigation and Laser Schlieren Technique is used for the study of heated bluff body case. The effect of orientation of the square cylinder and the effect of buoyancy on the wake behaviour are reported.

In square cylinder experiments, main objective is to study the interdependence between the attack angle with the wake characteristics and the drag coefficients. Angle of incidence in the range of 0-60 degrees have been considered in the present set of experiments. Results for three Reynolds numbers namely, 1340, 4990 and 9980 are reported. Velocity measurements have been carried out using an X-wire hotwire anemometer. Global properties such as the Strouhal number and the drag coefficient are computed from the measurements. Utilizing the velocity traces in the near and the far wake, turbulent statistics such as the normal and the shear stresses are obtained. Results obtained in the present work reveal the following: For inclinations greater than 0, the points of separation on the cylinder move downstream, the wake size increases, but the separated shear layer rolls up over a shorter distance. These factors lead to a reduced drag coefficient and a higher Strouhal number. The velocity fluctuations decay in the downstream direction. The decay rate depends on Reynolds number, but the role of the cylinder orientation is only secondary. However, the cross-correlation function strongly depends on the cylinder orientation, particularly at Re=4990 and 9980, before diminishing to zero along the wake centerline. In the near wake, the spectra of both components of velocity are dominated by the contribution of the vortex shedding frequency. The peaks are sharper in the v-component and persist even till $x = 18$.

The laser schlieren measurements behind the heated circular cylinder showed the distinct difference of the wake behaviour between the free convection and

mixed convection case. The overall wake size in the transverse and streamwise direction is higher for the mixed convection case than that of the free convection case. The photodiodes are used to study the transient wake behaviour. It is observed that the horizontal knife edge setting is more sensitive to transients than that of the vertical knife edge setting. The flow is observed to stabilize the unsteadiness of the wake. The average Nusselt number results obtained in the present work compares well with the existing correlation in literature.

ACKNOWLEDGEMENT

Contents

List of Figures

Nomenclature

A_c	Excess projected area of an inclined cylinder with respect to the straight, $= (D - B)/B$ %
B	Edge of the square cylinder, m.
D	Projected area normal to the flow direction,$= B(\cos\theta + \sin\theta)$, m.
C_D	Drag Coefficient based on the upstream velocity and D, Drag per unit length$/\frac{1}{2}\rho U^2 D$.
Eu	Dimensionless power spectrum of the u-component of velocity.
Ev	Dimensionless power spectrum of the v-component of velocity.
f	Dimensionless frequency variable, frequency (Hz) $\times$ B/U.
f_u	Frequency of vortex shedding based on the u-trace, Hz.
f_v	Frequency of vortex shedding based on the v-trace, Hz.
Re	Reynolds number, $\rho UB/\mu$.
Su	Strouhal number based on the u-signal, $f_u B/U$.
Sv	Strouhal number based on the v-signal, $f_v B/U$.
u	x-component velocity, m/s.
v	y-component velocity, m/s.
U	Upstream velocity, m/s.
u'	x-component velocity fluctuation, m/s.
v'	y-component velocity fluctuation, m/s.
$\overline{u'v'}$	Dimensionless turbulent shear stress, $100 \times \left[\frac{1}{N} \sum_i u'_i v'_i\right] \frac{1}{U^2}$.
x, y	Dimensionless coordinates from the cylinder center scaled by B.
X, Y	Dimensional coordinates from the cylinder center, m.
Gr	Grashoff Number, $g\beta(T_s - T_\infty)d^3/\nu^2$.
Pr	Prandtl Number, $\mu C_p/k$.
Nu	Nusselt Number, hd/k.
h	Average heat transfer coefficient, W/m^2K.

Greek Symbols

ρ	Fluid density, kg/m^3.
μ	Dynamic viscosity, Pa-s.
θ	Orientation of the cylinder with respect to the incoming flow.
ω	In-plane component of vorticity scaled by U/B.
σ	Stefan Boltzmann constant.
ϵ	Emissivity.

Chapter 1

Introduction

Flow past a bluff body has wide spread application in engineering. Most of the structures we encounter are bluff body like high rise buildings, ships, submarines where flow past over it. Starting from heat transfer, the forces acting on the body and flow induced vibration are the few major study. Recent application in signature analysis has made this study attractive. Heat transfer from electronic component is a major challenge since large heat is generated in a small area.

The research and development in experimental fluid flow has innovated and used a great number of methods, instruments and techniques. Today a choice among these is available, one being more suitable for a specific type of measurement than the other. Most of these methods and instruments have been developed and are used for measuring velocities in flows that are either laminar or assumed to be laminar. In fact only a few are suitable for making measurements in turbulent flows.

The major problems in measuring any complex flow particularly turbulence are caused by the fact that turbulence is a random, fluctuating flow and three-dimensional. This wide range of frequency components present in velocity fluctuations make it very difficult for a measuring instrument to satisfy in every respect the basic requirements. The recordings of the quantity to be measured must be as free as possible from distortion.

Broad classification of the various methods, techniques and instruments shows two major groups, namely (i) optical methods and (ii) intrusive methods.

Advanced flow visualization techniques have facilitated the efficient measurement of flow properties like velocity, density and temperature distributions prevailing in a flow field. In visualization to the conventional methods, the optical

methods are more advantageous as these are non-intrusive in nature and hence do not disturb the flow field itself under study. Without any loss in accuracy, the light beam can also be considered as inertia less, so very rapid transients can be studied which is not the case with the conventional methods which take some finite time to respond. Three most widely used non intrusive techniques are Laser Doppler Velocimetry (LDV), Particle Image Velocimetry (PIV) and Index of Refraction method.

LDV is the measurement of fluid velocities by detecting the Doppler frequency shift of laser light that has been scattered by small particles moving with the fluid. This particular technique demands the seeding of the flowing fluid for creating frequency shift. It can measures velocity in both isothermal and non isothermal flows and is independent of fluid temperature which is the major advantage over the thermal transducer. Other advantages of LDV are (i) easier to use (ii) non intrusive (iii) low velocity measurement (iv) give the velocity directly and (v) high accuracy. The limitations of the LDV are (i) very costly (ii) poor frequency response (iii) poor resolution and (iv) needs clean environment.

Particle Image Velocimetry (PIV) is a technique that measures the motion of small, marked regions of a fluid by observing the locations of the images of the markers at two or more times. This method returns to the fundamental definition of velocity and estimate the local velocity u_i from

$$u_i(x_i, t) = \frac{\Delta x_i(x_i, t)}{\Delta t}$$

where Δx_i is the displacement of a marker, located at x_i at time t, over a short interval Δt separating observations of the marker images. As this technique involves recording of flow frames at different times, it demands a good image capturing and processing unit. The light source generally used is pulsed laser. Like LDV, this technique also require seeding to illuminate the flow with proper tracer particle.

Optical techniques employing the index of refraction methods can be broadly classified into three main categories; (a) Interferometry, (b) Schlieren and (c) Shadowgraphy. With these methods one can easily visualize the flow fields and hence measure their density and temperature distributions. In interferometry, the changes in the refractive index with respect to a reference medium leads to the formation of images and give a direct measure of the values of refractive

index in the flow field. Schlieren employs the principle of light deflection in a field of variable refractive index. The output is in the form of distribution of light intensity i.e. change in intensity in relation to the original intensity. This gives the measure of the first derivative of refractive index which is to be integrated once to get the value of refractive index. Shadowgraphy is based on the reduction in light intensity as the beam diverges in its path through the field of variable refractive index. Here also the output is in the form of light intensity and gives the measure of second derivative of the refractive index. The sensitivities of these three methods are quite different, so they can be used to study a variety of systems. Thus, interferometry is used where the density gradients are small, while schlieren and shadowgraphy are employed where the density gradients are large like studying shock and flame phenomena. Despite the difference in the working principles of these methods, they are essentially integral; they integrate the quantity measured over the length of the light beam. For this reason they are well suited to measurements in two-dimensional fields, where there is no index of refraction or density variation in the field along the light beam.

In intrusion methods, a detecting element is introduced into the flowing fluid, and the turbulence quantities are measured by the changes of a mechanical, physical and chemical nature that occur in this element. As regards this group, there are a number of requirements that must be satisfied by the detecting element and the rest of the measuring apparatus before turbulence can be measured reliably:

- The detecting element introduced into the flowing fluid must be so small that it causes only the minimum admissible disturbance of the flow pattern.

- The instantaneous velocity distribution must be uniform in the region occupied by the element. This means that the detecting element must be smaller than the dimensions of the smallest eddies of the turbulence.

- The time constant of the probe must be low, so that response to even the most rapid fluctuations is practically instantaneous.

- The instrument must be sufficiently sensitive to record small differences in the fluctuations.

- The instrument must be stable, so that no noticeable change occurs in the calibration parameters during at least one test run.

- The instrument must be sufficiently strong and sufficiently rigid to exclude vibrations or motions caused by the turbulent flow.

There is one instrument whose development and application for measuring turbulent flow have far outstripped those of other instruments up to now, namely, Hotwire anemometer. Hotwire anemometer measure both fluid velocity and temperature by sensing the changes in heat transfer from a small, electrically heated sensor exposed to the fluid motion. This sensor is very small in size and has a very high frequency response. Its popularity for making turbulence measurements will be easily understood if it is realized that this is an instrument that reasonably satisfies all the above-mentioned requirements – although, of course, it has limitations.

The limitations of the hotwire anemometer are as follows: (i) it is not suitable for very small velocities unless proper attention has been given for calibration (ii) it is insensitive to direction of velocity (iii) for velocity measurement, constant temperature of the fluid is essential (iv) sensor is intrusive (v) very difficult to use because it is very fragile and sensitivity to contamination and (vi) velocity is not measured directly.

Quantitative schlieren technique used for flow past a heated cylinder. This is because of the lower instrumentation cost and better adaptability to high temperature problems. Using the experimental measurements of the fluctuating properties of turbulent flows have mainly been obtained by the use of the hot wire anemometer system. Hot-wire anemometry have been quite successful in flows where the dynamic pressure and total temperature of the fluid are not excessive. But the fragility of the detection probes has prohibited their application to a number of flow conditions, which are of interest in the study of power plant and flight propulsion systems. The development of some alternative approach (schlieren technique) is therefore of considerable importance in regard to the study of the properties of the flow in these more adverse environments. Schlieren methods were originally used in Germany for the detection of inhomogeneous regions in optical glass which are often in the form of streaks (schlieren in German). The Schlieren technique thus derives its name from the word schlieren . The penalties which, the application of the simple schlieren technique incurs are the inevitable integration of the measured signal along the beam path and the relatively low

signal-to-noise ratios which can be achieved in some applications.

1.1 Literature Review

1.1.1 Unheated Cylinder

Okajima (1982) carried out an experimental study of flow past square and rectangular cylinders in the Reynolds number range of 70 - (2 $\times 10^4$). This study established the variation in Strouhal number, that is the non dimensional vortex shedding frequency, with Reynolds number. These experiments have shown that there is a abrupt change in Strouhal number when the aspect ratio of the cylinder is reduced to the range 2 − 3. This is reflected as a corresponding change in the wake pattern.

Durao *et al.* (1988) conducted LDV measurements for flow past a square cylinder at a Reynolds number of 14,000, in a water tunnel. They have separated the periodic and random components of velocity fluctuations. These measurements show that the kinetic energy associated with the random components is about 40% of the total.

Lyn *et al.* (1995) carried out LDV measurements in the wake of a square cylinder in a water tunnel at a Reynolds number of 21, 400. The experiments were carried out in a closed and constant head water tunnel. Their results showed a relationship between the flow topology and the turbulence distribution. Vorticity saddles and streamlines saddles were clearly distinguished. A distinction was identified between the flow in the base region and the near wake. Differences in the length and velocity scales, and celerity of the vortices of flows around a circular and a square cylinder have also been compared.

Knisely (1990) did extensive study on Strouhal numbers for a rectangular cross-section as a function of their orientation.

Norberg (1993) reported a more detailed study relating the forces and shedding frequencies to the flow details. The role of confinement effects and the free stream turbulence intensity on the forces has been brought out in this study.

Sohankar *et al.* (1998) have carried out numerical calculations at low Reynolds numbers (< 200) to study the influence of the cylinder orientation on the macroscopic flow properties such as forces, moments and the Strouhal number.

Saha *et al.* (2000a) carried out experiments for flow past a square cross-section

cylinder. The literature can be classified into low, intermediate and high Reynolds number regimes. The wake becomes unsteady even at relatively low Reynolds numbers and displays complex vortical structures closer to the cylinder body. The range of parameters of the present set of experiments places the study in the moderate-to-high Reynolds number regime. Experiments that characterize the effect of the cylinder orientation on the wake properties have not been reported.

1.1.2 Heated Cylinder

Davis (1970) applied the schlieren technique in an axisymmetric subsonic turbulent jet. He related the unsteady flow density gradients to the variation of light intensity in a schlieren image and presented the fluctuating density gradient across the jet. He (1972) also reported the density fluctuations in the supersonic axisymmetric turbulent jet using a single beam schlieren system and presented the difference in the distribution of fluctuating density between the supersonic and subsonic jet.

Chang and SA (1990) has investigated numerically the vortex shedding for flow past a heated/cooled circular cylinder in the mixed natural and forced convection regimes.The role of heating the cylinder on the vortex shedding and average Nusselt number reported.

Kiefer and Hajdak (1990) reviewed the laser schlieren technique for applications on determination of the net rate of endothermic reaction and primary dissociation parameters like relaxation times and rates of primary dissociation, etc. They discussed the accuracy with which the signal generated by differential detector will reproduce the variation of the refractive index gradient in a reactive shock.

Kosugi, Maeno, and Honma (1993) measured the gas temperature profiles in the discharge regions of the excimer laser cavity by laser schlieren method. The diffraction of the laser beam due to the motion of discharged hot gas was used to measure the temperature distribution.

Koreeda et al. (1995) experimentally investigated the thickness of shock waves and the density profiles at high Mach numbers (between 16 and 34) by means of the schlieren technique. While analyzing the schlieren signal, they took into account the detector response, which was crucial in the case of strong shock waves

(M>16), as the signal must be obtained in a few micro-second.

Bystrov et al. (1998) presented a new approach to the problem of density reconstruction behind the shock front, where the beam diffraction in the non-uniform medium and the distortion of the signals in electric circuit were taken into account. They concluded that their approach has better spatial resolution than traditional beam optics approach and is suitable to investigate the density distribution in the vicinity of the shock front where the characteristic length is considerably small compared to the beam diameter.

Greenberg, Clime and Bushel (1995) discussed color schlieren method, where a continuously graded rainbow filter is placed in the back focal plane of the decollimating lens. The colour CCD camera and the video digitizer was used to quantify accurately the colour attributes of the resulting image and hence the associated ray deflections. They concluded that the rainbow schlieren deflectometry provides sensitivity comparable with that of conventional interferometry, while being less sensitive to mechanical misalignment.

Al-Ammar et al. (1998) used rainbow schlieren deflectometry technique to measure the oxygen concentrations in an axisymmetric helium jet. The concentration distributions were inferred from the schlieren image by taking into account the sampling interval and noise in measurements. Excellent quantitative agreement was reached between measurements from schlieren and a continuous sampling probe.

Agrawal et al. (1998) presented quantitative rainbow schlieren deflectometry with tomography for measurements of temperature in 3D gas flows. The results agreed quite well with the thermocouple measurements.

Shenoy, Agrawal, and Gollahalli (1998) computed field distributions of species concentration and temperature of an isothermal helium jet and hydrogen jet diffusion flame and compared quantitatively by inverting the experimental schlieren results. Their results demonstrated the effectiveness of the rainbow schlieren technique for validating the CFD models of reacting and non-reacting steady flows in axisymmetric systems.

Fu and Wu (1998) presented a novel technique of analysis of velocity distribution of a fluid field using image sequences taken from a Schlieren apparatus. The Schlieren setup for the study was a modified positive-negative grid system. The velocity distribution obtained from the image analysis technique was compared

with the experimental study of the flow field.

Agrawal, Albers and Griffin (1999) presented an Abel - inversion algorithm to obtain mean and RMS refractive index profiles from deflectometric measurements in time-dependent flows. The algorithm was validated by synthetic data and then applied to investigating an oscillating gas jet diffusion flame.

Albers and Agrawal (1999) investigated the flow structure of a flickering gas-jet diffusion flame using quantitative rainbow schlieren deflectometry. They described the flame structure by mean, root mean square (RMS) and probability density function profiles of temperature. Their results showed global oscillations in the flow field of the flame at a frequency varying linearly with the operating pressure.

1.2 Objective of Present Work

Unlike a circular cylinder, the separation points for square cylinder are fixed. For a square cylinder at zero angle of incidence, these points are at the leading edge. Thus the flow characteristics are relatively insensitive to Reynolds number, but will depend on the orientation of the cylinder with respect to the approach flow. The configuration considered in the present work is depicted in Figure 1. A fixed square cylinder with side B is positioned at an angle θ with respect to the uniform upstream velocity U. The primary objective is to study the effect of orientation on the wake dynamics with respect to the approach flow direction. The turbulent statistics, Strouhal number and drag coefficient variation for different angle of attack is presented with the help of hotwire anemometry.

The wake dynamics behind the circular cylinder kept at constant temperature is studied for investigating the effect of the buoyancy on the flow separation and the instability. The effect of buoyancy for flows past a heated horizontal cylinder is studied using photo-diode and CCD camera. CCD camera is used for steady state analysis and photodiode is used for transient analysis of the schlieren signal. Both the steady and temporal behaviour of the wake behind the heated cylinder are discussed. The Nusselt number is also calculated and compared with the existing correlations.
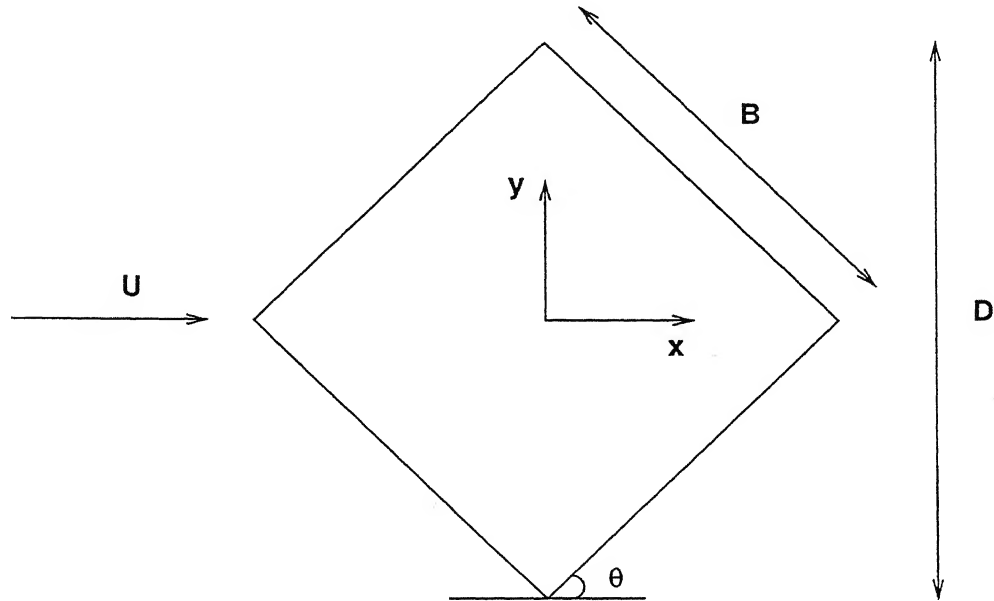
Figure 1.1: Schematic drawing of a square cylinder placed at an angle θ to the incoming flow

1.3 Thesis Outline

Subsequent chapters have been arranged in the following way:

Chapter 1 presents the introduction, the literature survey and the importance of the problem. Chapter 2 explains the experimental setup for both heated and unheated bluff body and the instrumentation used for experiments. Chapter 3 discuss about the principle of measurement techniques and empirical relations used for calculating the parameters used for characterization of the wake. In chapter 4, the results for heated and unheated cylinder are presented. Overall conclusions are summerised in Chapter 5.

Chapter 2

Apparatus and Instrumentation

2.1 Wind Tunnel

All the experiments were conducted in a low speed open circuit wind tunnel. Figure 2.1 shows a schematic of a low speed wind tunnel used for experiments. The test cells have been designed to achieve required flow and temperature conditions with minimum power consumption . The major parts of the test cell are (i) entrance cone containing honeycomb and filter (ii) development section (iii) measurement section (iv) passive protection section (v) blower and (vi) traversing mechanism.

The function of honeycomb is to straighten the flow by damping the other two transverse components of velocity and to reduce the turbulence level by suppressing the turbulence scales whose wavelengths are larger than the size of honey combs. The filters are used to suppress the small disturbances generated at the outlet tips of the honeycomb by modifying the shear layers and the instabilities. The entrance cone which has two parts namely the settling chamber and contraction cone upstream of the working section reduces the spatial irregularities considerably in the velocity distribution and helps in the decay of remaining turbulence intensity present in the upstream by the proper stretching of the smaller vortices present therein. The flow development section is generally used to manipulate the flow condition entering into the measurement section. The measurement section for wind tunnel has a dimension of 3 m×40 cm×40 cm. The wind tunnel has been provided with a narrow slots on the top of the measurement sections to incorporate the hotwire probes. Proper care has been taken to ensure minimal disturbances caused by these slots. The measurement section has also a diver-
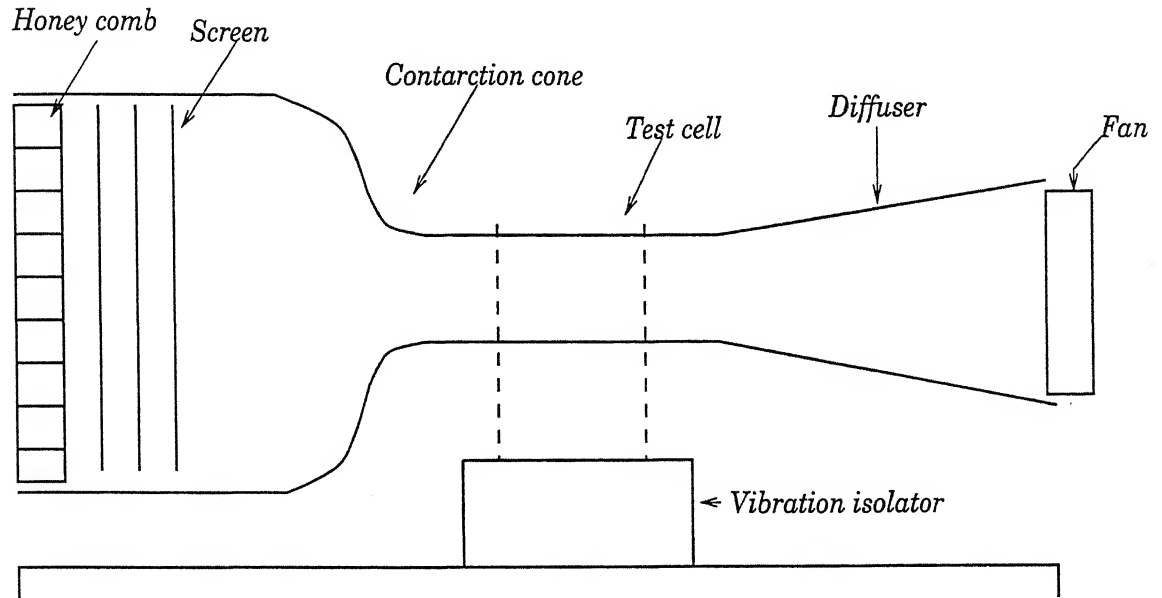
Figure 2.1: Schematic of a low speed open circuit wind tunnel.

gence angle of 4° to account for the pressure loss and boundary layer growth. It has been found that the pressure across the test sections is fairly constant.

A long passive section in the wind tunnel following the measurement section. The specific purpose of these sections is to protect the flow field in the measurement section from disturbances from the blower. This also helps in increasing the overall resistance of the tunnel and to produce stable velocities. The diverging adapter has been incorporated in the wind tunnel just after the passive section to adjust the bigger diameter blower and to recover the pressure loss within the wind tunnel.

The flow in the wind tunnels has been achieved through the use of a blower. The blower is connected to the suction or exit side of the wind tunnel. The velocity variation during an experiment running for a duration of three hours is within ±0.5%. However, the speed control of the wind tunnel is achieved through the use of an electronically controlled speed regulator giving the maximum variation of ±1 RPM of the motor giving a velocity variation of ±0.07%. The last important accessory is the traversing mechanism.It has all the three degrees of freedom with accuracy of ±0.1 mm and manually operated.

2.2   Vertical Test Cell

Figure 2.2 shows a schematic of Vertical Test Cell and the coordinates of the heated cylinder inside the test section is shown in Figure 2.3.

The major components of the experimental setup are (i) vertical wind tunnel (ii) blower (iii) heating arrangement for cylinder (iv) data acquisition setup and (v) optical arrangement for Schlieren. As shown in Figure 2.3, the measurement region has a 400 mm×400 mm cross-sectional area and the cylinder is placed in cross flow direction. Flow in the test region is maintained by a low speed vertical wind tunnel. Steady flow is achieved with a 0.5 hp blower giving a maximum air speed of 0.35 m/s. Flow inside the test cell is measured by a pitot static tube and a micro manometer (19.99 mm of H_2O). The cylinder (6mm dia) under study placed horizontally in the test cell along the laser beam.

2.3   Heating Arrangement

The cylinder kept at a fixed surface temperature with the help of a heating arrangement within an accuracy of $\pm 1^\circ$C. The schematic diagram of the temperature controlling unit is shown in Figure 2.4. Cylinder heating is switched on/off by a solid state relay. Regulated power is supplied by a variac to the heating element. Temperature of the cylinder is measured by a thermocouple whose output is amplified by a signal conditioning circuit which gives temperature readings in terms of millivolts.

2.4   Laser Schlieren Optical Set-up

The optical arrangement mainly consists of the basic Schlieren set-up. The Schlieren methods depend on deflection of a ray of light from its undisturbed path when it passes through a medium in which there is a component of the gradient of refractive index normal to the ray. A typical Schlieren apparatus is sketched in Figure 2.5.

A He-Ne 15 mW laser is used as a light source, which directs the beam on a concave mirror through a plane mirror such that the test region is illuminated by a parallel beam of light. A second concave mirror is placed beyond the test section such that the image of the source is produced at the focal plane of the
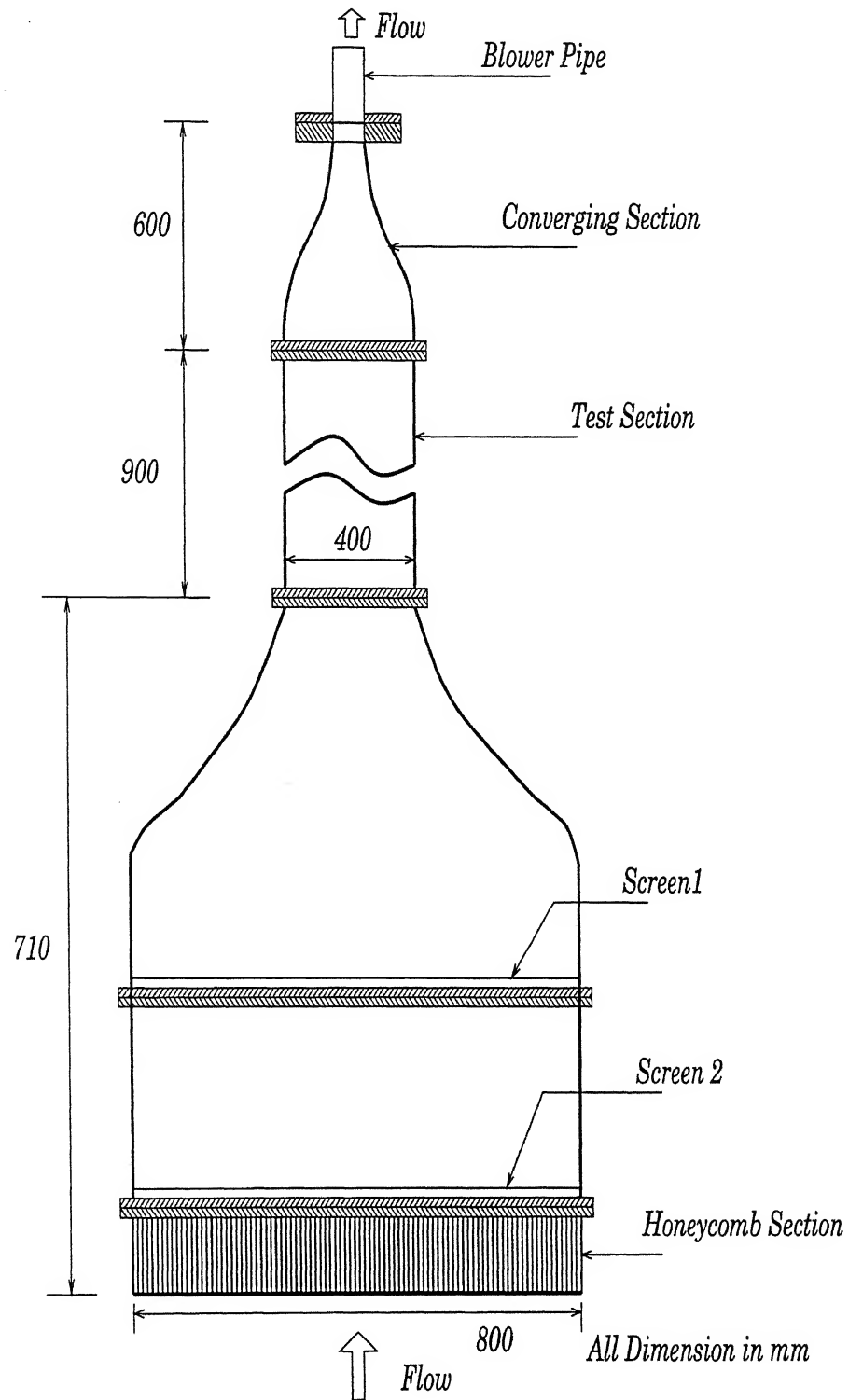
Figure 2.2: Sketch of vertical test cell.
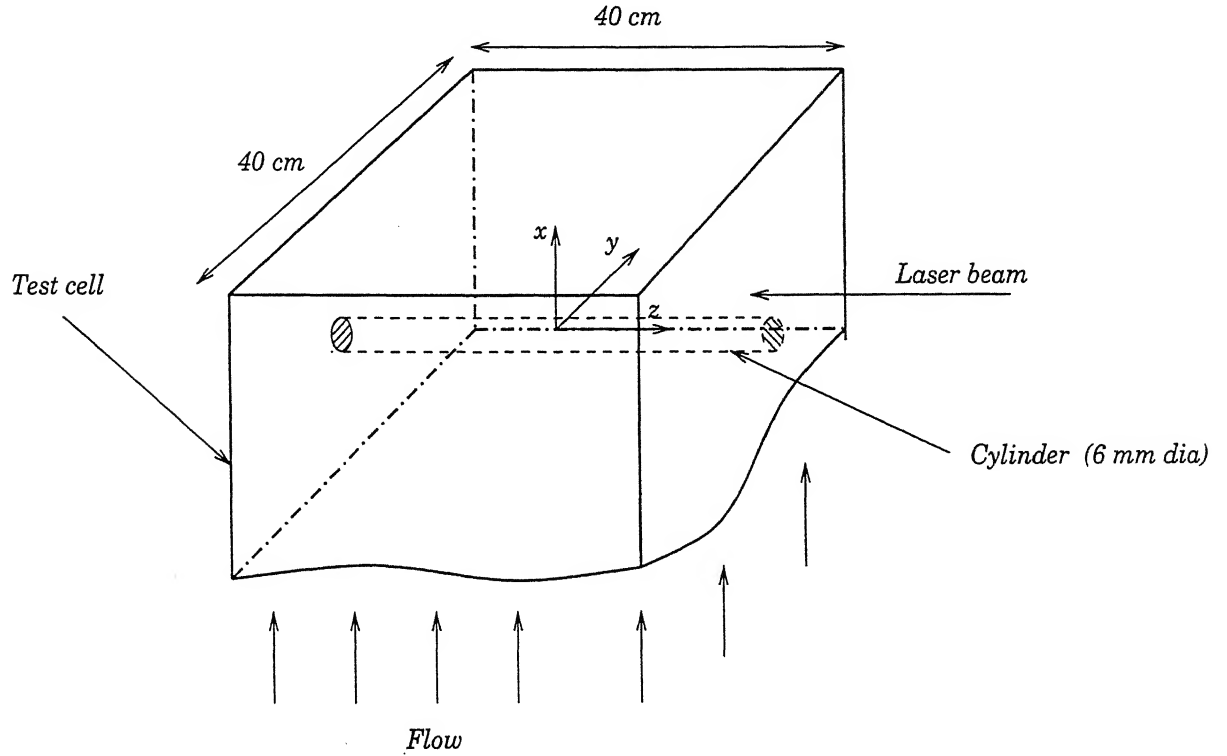
Figure 2.3: Schematic diagram showing the coordinates of the heated cylinder inside the test cell.

2nd mirror where the knife-edge is placed. If there is no gradient in refractive index, all light from a point of the source is brought to a focus on the viewing screen. Due to the presence of the knife-edge, the displacement of the image of the source inside the test region results in a change of illumination on the screen. The knife-edge is so adjusted that in the absence of the optical disturbances, part of the light from the image of the source is cut off so that the illumination on the screen is reduced uniformly. When the optical disturbance is introduced, part of the image source is displaced and the illumination of the corresponding part of the image will decrease or increase according to whether the deflection is towards or away from opaque side of the knife edge. Displacement of the image of the source parallel to the knife-edge produces no effect at the screen and the edge must therefore be set perpendicular to the direction in which the density gradients are to be observed.

The diffraction affects the accuracy of the quantitative Schlieren methods. The magnitude and extent of its effects increase as the proportion of the source
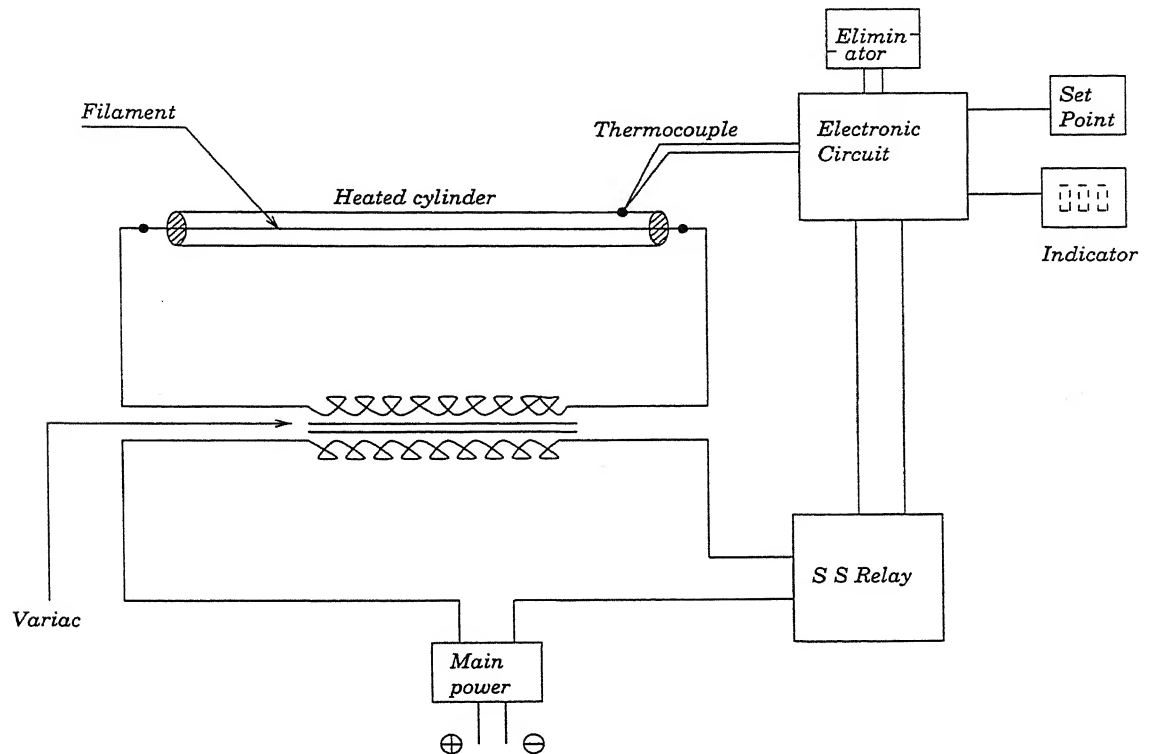
Figure 2.4: Schematic diagram of heating arrangement.

cut off by the knife-edge is increased. It is found that although the illumination
on the viewing screen is approximately constant in the absence of the knife-edge,
this is no longer the case when knife-edge is present. The effects of diffraction then
usually results in increased illumination on the viewing screen as the boundaries
of the aperture are approached . The illumination does not fall sharply to zero
at the boundaries, but dies away gradually.

2.5 Hotwire Anemometry

A hotwire anemometer responds principally to the velocity magnitude and is
based on the principle of heat transfer. Hence for using a single sensor hotwire
anemometer, the flow direction must be known. If three sensors of the hotwire
are arranged in such a way that they provide independent output signals, the
three components of velocity can be measured and the velocity vector can be
determined. In a two-dimensional turbulent flow, a two sensor hotwire known
as crosswire can measure two components of velocity. The velocity measured by
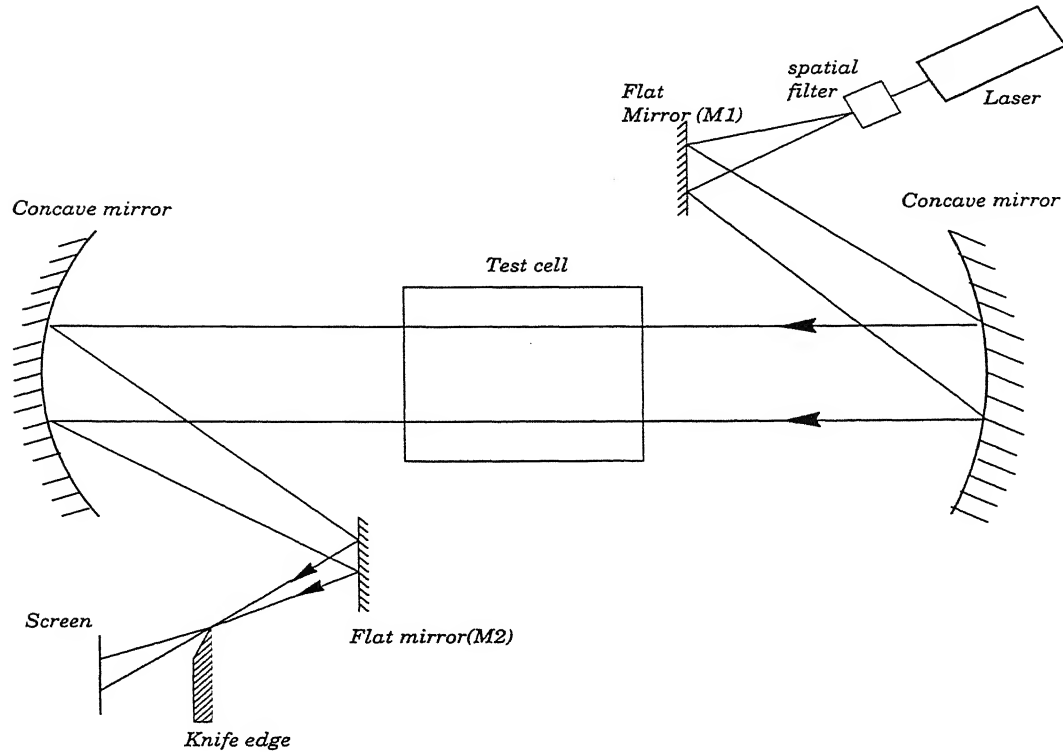
Figure 2.5: Schematic diagram showing Laser Schlieren set-up.

each wire is different from the component of velocity along laboratory coordinates. The velocity sensed by each wire is known as the effective cooling velocity.

In two-dimensional measurements, calculation of velocity components involves solving of a pair of non-linear, simultaneous equations. Velocity measurements in varying temperature flows require special calibration. Thus the accuracy of hotwire measurements are affected by the accuracy of calibration procedure and accuracy of solution procedure that is used to solve the nonlinear simultaneous equations. The hotwire is basically a thermal transducer. Simply stated its principle of operation is as follows. An electric current is passed through a fine filament (5 μ m diameter and 5 mm length), which is exposed to cross flow. As the flow rate or flow temperature varies the heat transfer from the filament varies. This in turn causes a variation in the heat balance of the filament. The filament is made from platinum coated tungsten which posses a high temperature coefficient of resistance. The variation of resistance is monitored by a feedback circuit which passes additional current till the wire temperature is maintained constant independent of the flow velocity or temperature. The hotwire and feedback circuit

combination is referred to as a Constant Temperature Anemometer (CTA). This temperature is usually much higher than the room temperature typically 100-200 °C in air flow measurements. Higher temperatures enhances the sensitivity of wire but make the wire fragile.
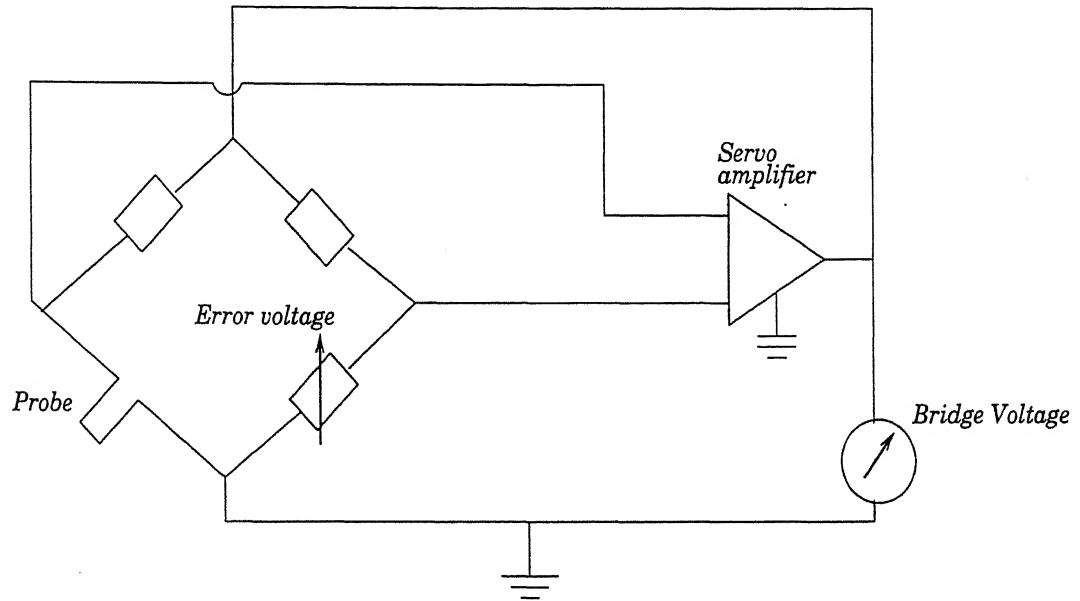
Figure 2.6: Electric circuit for Constant Temperature Anemometer(CTA).

As shown in Figure (2.6) the constant temperature anemometer (CTA) consists of a Wheatstone bridge and servo-amplifier. The temperature of the problem will cause a change of voltage at the servo-amplifier inputs. The output voltage of the servo-amplifier is applied to the bridge so that the original temperature of the hotwire is maintained by varying the bridge operating voltage. Higher the gain of the servo system, more rapidly the amplifier responds and lower will be the error voltage across the horizontal diagonal of the bridge, which is to be compensated for a temperature change in the sensor. The feed back circuit plays an important role in improving the frequency response of the hotwire from about 100 Hz to 10kHz.

Another mode of operation is constant current operation. In this operation the current through the hotwire is constant while the resistance of the wire changes according to the nature of forced convection. Thus voltage fluctuations occur due to change in wire resistance. These are amplified and fed into a thermo-couple type mean square meter. A manual compensation is required because of the

thermal inertia of the wire which in turn attenuates the amplitude response of the anemometer at high frequency fluctuations.

2.5.1 Arrangement for Hotwire Experiments

A square cylinder placed in the wind tunnel horizontally. The cylinder is long in the axial direction, in relation to its edge B. The aspect ratio in the present experiments was close to 15. The square cylinder used was made of Perspex, 25 mm $\times$25 mm in cross section. The use of Perspex was advantageous since (1) good quality smooth surfaces were attainable over the entire cylinder, and (2) precise sharpness of the cylinder edges could be maintained. The cylinder length was 40 cm, thus spanning the entire width of the wind tunnel. Upstream velocities of 0.86, 3.1 and 6.2 m/s were utilized to produce Reynolds numbers of 1300, 4990 and 9980 respectively, in the experiments. The room temperature during all the experiments was $30(\pm 2)^o$ C.

Velocity was measured using a two channel hot wire anemometer along with an X-wire probe. The X was formed in the vertical plane, with the cylinder placed in a horizontal position. The probe was mounted on a traversing mechanism that facilitate all three orthogonal movements, to a positional accuracy in the most significant direction, namely the vertical at ± 0.1 mm. The commercially available DANTEC anemometer and probes were employed in the present work. The two wires of the probe were calibrated in the wind tunnel itself. Small changes in room temperature ($\pm 1^o$C) were compensated through the use of a correction formula that assumes a constant heat transfer coefficient.The probe was recalibrated for larger changes in temperature. Both wires were operated at 150°C, and there calibration curve were seen to be almost identical.The assumption of equal sensitivity coefficients of the two wires was occasionally employed during data reduction.The calibration curves were smoothed using a fifth order polynomial. A pitot tube with a 19.99 mm of H_2O (Furness Controls) digital manometer used for calibration. Both DC and rms values of voltages were recorded using "true" voltmeters supplied by Dantec. Integration time of typically 100 s were used to obtain all time-averaged quantities. The cross-correlation between the voltage fluctuations was determined by collecting long time traces. Thus the configuration may be taken to be nominally two dimensional. For the range of velocities

considered, incompressible flow conditions can be assumed to prevail.

2.5.2 DANTEC CTA Bridge and Accessories

The DANTEC model 56 C 17 CTA is described in the present notes. The main unit 56 C 01 CTA delivers the servo voltage as the output of the instrument. This voltage is a measure of the fluid velocity. The feed-back circuit of the CTA plays an important role in improving the frequency response of the hotwire from about 100Hz to 10 kHz.

The 56 C 01 CTA contains a function switch with three modes for operation, namely TEMP, STD.BY and FLOW. In TEMP position the resistance of the connected probe can be measured in terms of a current supplied to it. In STD.BY position no current flows through the bridge. In FLOW setting the CTA starts operating with the function of the servo amplifier. A setting named BRIDGE ADJ enables the adjustment of bridge balance for measurement of probe.resistance and setting of the desired overheat resistance. This BRIDGE ADJ has a switch pair for coarser adjustment of overheat resistance and a screw for fine adjustment. Resistance settings ranging from 0-30 Ω in steps of 0.001Ω are possible. This adjustment is crucial for adjusting the overheat resistance for the calibration procedure. CTA in TEMP mode produces a voltage proportional to resistance of wire. Calibration of this voltage with known temperature can be directly used to measure instantaneous temperature of the probe. Mean value unit 56 N 22 is a 5.5 digit display voltmeter. The primary purpose of this module is to measure the d.c. component of output signal from 56 C 01 CTA. This module has a 100 μV resolution, 1-1000 seconds integration times and switch selectable 14 inputs. The module 56 N 23 Analog Processing Unit (APU) is an analog signal processing module for use with two 56 C 01 CTA modules. The 56 N 23 APU allows the formation of sums and differences of two input signals as well as a derivative with a variable time step. The 56 N 20 signal conditioner is a module which amplifies and filters a.c. output signals from 56 C 01 CTA. It contains low-pass and high-pass filters which can filter the signal in the required range of frequencies. 56 N 20 signal conditioner can selectively amplify the input signals with gain factors ranging from 1-900. This amplification is very important in the measurement of temperature signals.

In the present work we have used three 56 C 01 CTA modules which make a 3-channel CTA. Each channel has a separate 56 N 20 signal conditioner and 56 N 23 APU. A 3-wire probe can be connected to this setup and outputs of 3 wires can be measured simultaneously. Only 2-wire measurements are reported in this work. We used 56 N 22 to measure mean voltage of each channel with integration time constant of 10 seconds. The signal conditioner is set to a.c. mode in which the mean of the signal removed from the instantaneous voltage signal. RMS values and other statistics are measured with a digital oscilloscope and a spectrum analyzer.

2.6 Instrumentation

Details of instrumentation used for hotwire and laser schlieren experiments are discussed in the present section. These modern instrument will have variety of special features. Instruments manufactured by specific companies are discussed here.

2.6.1 Digital Oscilloscope

A Gould 1602 two channel digital storage oscilloscope with a sampling speed of 20 Ms/sec and an operating frequency range of 0-20 MHz has been used in this work. The 1602 can operate in storage as well as non-storage mode. It has advanced features such as menu controlled memory, acquisition/ trigger menu and optional features like GPIB (IEEE 488) and RS423 input/output ports for external control by a host computer. A Gould waveform processor 460 provides enhanced measurements and trace processing.

The oscilloscope can acquire very long signal containing data points as many as 10240, simultaneously from two channels. This facility can be used to collect long signals of u' and v' measured simultaneously. This oscilloscope with the waveform processor does on-line calculation of rms values of signals in storage mode.

2.6.2 Spectrum Analyzer

The ADVANTEST R 9211 E is a digital spectrum analyzer that works based on FFT. Wide band as well as high sensitivity measurements can be performed

with the frequency range being 10 mHz-100kHz and input voltage range being 1μVrms-31.6 Vrms. Time area analysis, frequency analysis, frequency response, time-frequency analysis and function measurement are available in the analyzer.

The analyzer has four different modes of operation. The waveform and spectrum modes are important ones generally used in turbulence measurement. In waveform mode the spectrum analyzer does on-line measurement of the time signal, histograms (PDF), autocorrelation and cross-correlation functions. In spectrum mode it measures power spectrum and complex spectrum. The analyzer has two single ended/differential input channels. The analyzer also has multi-screen function through which 1-4 screens can be selected simultaneously. It has different menus such as Math, Setup, Device and Copy. The Math menu does arithmetic operations between two arrays and integration and differentiation of an array. This facility can be used for the measurement of average of product of two-wire signals. The device menu operates the floppy drive and GPIB connections. All traces shown on the screen can be stored on a floppy and processed whenever required. This facility has helped in collecting a large volume of data.

The spectrum analyzer has been used mainly for data collection, ensemble averaging and determination of statistics. Instantaneous traces of statistics can be ensemble averaged. The averaged spectra, PDF, correlation functions can be transferred to a PC over a GPIB interface.

2.6.3 LabVIEW Software with DAQ

The graphical programming concept introduced the possibility of creating a new type instrumentation, not in hardware but rather in software. This new instrument is called Virtual Instrumentation (VI). It is a simulation tool. It is a method of developing instrument using standard Data Acquisition Cards. Very complex instruments and control systems can be developed efficiently using VI tools. LabVIEW (Laboratory Virtual Instrument Engineering Workbench) is a program development environment, much like modern C or BASIC development environments. LabVIEW is different from those applications in one important respect. Other programming systems use text-based languages, G, to create program in block diagram form. The principle of data flow, in which functions execute only after receiving the necessary data, governs execution in a straight

forward manner.

LabVIEW, like C, Pascal, or BASIC, is a general-purpose programming system with extensive libraries of functions for any programming task. LabVIEW includes libraries for data acquisition, VXI, GPIB and serial port instrument control, data analysis, data presentation, and data storage. LabVIEW also includes conventional program development tools, so we can set breakpoints, animate program execution to see how data passes through the program, and single step through the program to make debugging and program development easier.

The A/D card used for experiments is a PCI- MIO- 16E-1 series card of resolution 12 bit for ADC. Input-voltage range is $\pm 10 volts$. It have gains of $0.5, 1, 2, 5, 10, 20, 50, 100$ and suited for a wide variety of signal levels. Precision of the card for a gain of 1 is $4.88 mv$. Card has connected with the instrument by a 50 pins connector block (CB 50). Driver software used NI DAQ software.

2.6.4 Photodiode

Study of temporal wake behaviour is done by a highly optical sensitive photodiode (Jain lasertech, model PD-10). The photodiode is placed behind the knife edge on a optical mount. The output of the photodiode is of the order of few millivolts. So it is amplified with photo amplifier (Jain lasertech, model PA-10). The photo amplifier is connected to PC based DAQ (NI) through a terminal block. Since photodiode gives point measurement its positional accuracy is very important. The optical mount on which the photodiode was mounted has a positional resolution of 0.1 mm.

2.6.5 CCD Camera

To do qualitative measurement a SONY CCD (charged coupled device) camera was used. It has a maximum spatial resolution of 764×574 pixel. This camera is connected to a PC-based image processing system through an 8-bit A/D card. The image stored in the form of a matrix of integers, with intensities varying between 0 and 255, where 0 indicates black and white is 255. The frame grabber used has a image acquisition rate of 50 images per second.

2.6.6 Pressure Transducer

The velocity in the wind tunnel and vertical test cell was measured by pitot tube and micro manometer (Furness Controls) pressure transducer. A Maximum pressure of 19.99 mm of water head can measure. The micro manometer gives the digital as well as analog output. It has in built integrated circuit which measures velocity (m/s) and pressure (mm of water head) directly. It has both auto and manual mode with resolution of 0.01 m/s. Averaging also can be done through a selectable knob. It is precalibrated so it requires correction chart to compensate change in ambient temperature.

Chapter 3

Data Analysis

3.1 Hotwire Measurements

3.1.1 Principle of Operation

Heat transfer from hotwire is mainly by convection. With the assumption of uniform radial temperature distribution within a fine wire, the thermal equilibrium of the wire placed in a fluid gives the following heat balance relation.

$$H + E = i^2 R_w \tag{3.1}$$

where $H = hA(T_w - T_f)$ and E is the change in internal energy of the wire.

A is the area of hotwire per unit length, m,

h is the convective heat transfer coefficient, $W^\circ C^{-1} m^{-2}$,

T_w is the temperature of wire, $^\circ C$,

T_f is the temperature of fluid, $^\circ C$,

i is the current flowing through wire, Amp, and

R_w is the resistance of wire, Ω.

We can write

$$E = mC \frac{dT_w}{dt} \tag{3.2}$$

where m is the mass of wire per unit length, kg/m,

C is the specific heat of the wire material, $J kg^{-1 \circ} C^{-1}$

The governing convective heat transfer equation is

$$mC\frac{dT_w}{dt} + Ah\left(T_w - T_f\right) - i^2 R_w = 0 \qquad (3.3)$$

Convective heat transfer coefficient h is the major quantity to measure. The rate of change of internal energy is practically zero for CTA mode hotwire. This gives,

$$H = 2\pi K_f l\left(T_w - T_f\right) \text{Nu} \qquad (3.4)$$

where, $\text{Nu} = \frac{hd}{K_f}$ is the Nusselt number,
d is the sensor diameter,
K_f is the thermal conductivity of fluid,
$2l$ is the length of sensitive area of hotwire.

The term which contains the effects of fluid velocity, temperature of wire and temperature of fluid is Nusselt number. The general expression for forced convection Nusselt number in the case of incompressible flow is given by,

$$\text{Nu} = f\left(\text{Re}, \text{Pr}, a_1, \text{Gr}, \text{Ma}, \gamma, a_T, 2l/d, K_f/K_w\right) \qquad (3.5)$$

where $\text{Re} = \frac{U_c d}{\nu}$ is the Reynolds number,
$\quad U_c$ is the effective cooling velocity,
$\quad \nu$ is the kinematic viscosity of fluid,
$\quad Pr$ is the Prandtl number,
$\quad C_p$ is the specific heat of fluid at constant pressure,
$\quad a_1$ is the angle between free stream flow direction and normal to wire,
$\quad \text{Gr}$ is the Grashoff number,
$\quad \text{Ma}$ is the Mach number,
$\quad \gamma = \frac{C_p}{C_v}$,
$\quad C_v$ is the specific heat of fluid at constant volume,
$\quad a_T = \frac{(T_w - T_f)}{T_f}$ is the temperature loading or overheat ratio.
$\quad K_w$,K_f are the thermal conductivities of wire and fluid respectively.

Fortunately, most applications permit a significant reduction in the number of parameters that must be included. The reasons are stated below.

1. Forced convection parallel to the wire is small.

2. Pr depends only on fluid properties, and buoyancy effects can be neglected for $Gr \times Pr < Re^2$. For velocities of fluid greater than 5.2 cm/s, buoyancy effects can be neglected.

3. For low density and low velocities, Mach number is negligibly small and C_p and C_v can be assumed to be constant.

The general equation governing the operation of hotwire can be simplified as,

$$Nu = f(Re, a_T) \tag{3.6}$$

In isothermal flows measurements Equation 3.6 can be further simplified as

$$Nu = f(Re) \tag{3.7}$$

Analytical derivation of functionality between Nu, Re and a_T is very difficult. Simple analytical solution of Equation 3.7 shows that a power law relation is generally valid. The value of exponent depends on geometric and physical properties of wire and physical properties of fluid. An empirical correlation derived using individual calibration of wire is generally recommended in hotwire applications.

Collis and Williams (1959) suggested an accurate formula for Nusselt number which accounts for the change in properties of the fluid. The expression can be stated as,

$$Nu = (A + BRe^n) \left[1 + \frac{a_T}{2} \right] \tag{3.8}$$

They evaluated the constants in the above formula from the calibration of the wire at different velocities and temperatures. The values of the constants are,

$$A = 0.24, \quad B = 0.56 \quad \text{and} \quad n = 0.45 \quad \text{for} \quad 0.02 < Re < 44.$$

$$A = 0.00, \quad B = 0.48 \quad \text{and} \quad n = 0.57 \quad \text{for} \quad 44 < Re < 140.$$

Koch and Gartshore (1970) suggested a different formula, namely,

$$Nu \left(\frac{T_m}{T_f} \right)^a = A + BRe^n \tag{3.9}$$

where $T_m = \frac{T_w + T_f}{2}$, $A = 0.24$, $B = 0.56$, $n = 0.45$ and a = 0.67.

The correlations given above are in terms of non-dimensional parameters. It is convenient to work in dimensional form as,

$$\frac{E^2}{R_w\,(T_w - T_f)} \;=\; A\left(\frac{T_m}{T_f}\right)^{a1} + B\left(\frac{T_m}{T_f}\right)^{a2} U_c^n \qquad (3.10)$$

Collis and Williams (1959), Koch and Gartshore (1970), Davies and Fisher (1964) and Bearman (1971) suggested widely differing values for these constant of calibration surface given by Equation(3.9).

The values of these constants depend on l/d ratio of the wire, material of the wire and fluid properties. The choice of the numerical scheme, number of calibration points and range of variable also affect the overall accuracy of the calibration procedure. The need to generate flows at different velocities and temperatures for calibration is a second source of error. As a result, overall accuracy of calibration for non-isothermal problems have been reported in the range 90-95%, implying an error of 5-10%.

Koch and Gebart (1972) suggested an indirect method which does not require uniform flows of different velocities and temperatures, but is valid primarily at low velocities. This method has been extended in the present work and the calibration errors are seen to be less than 1% for a wider range of velocities and temperatures.

3.1.2 Hotwire Calibration

General calibration of hotwire involves two major steps, namely Data-generation and Curve-fitting.

Data-Generation

Calibration data is generated by measuring the output of wire when it is subjected to a fluid with known velocity. Specially designed apparatus are used to generate high quality flow with uniform velocity, temperature and very low turbulence level ($< 0.1\%$). DANTEC Instruments supply calibration equipment which produce a flow with qualities mentioned above. One can build their own test cell which can produce good quality flow.

Hotwire to be calibrated should be kept firmly in the calibration apparatus such that the direction of velocity of uniform flow should be normal to the wire.

The velocity of the flow should be steady. The apparatus should be able to produce uniform flow with variable velocity. Output of the wire is noted at zero velocity and at various velocities of flow. Measurements can be repeated at a given velocity and average output of the wire can be taken as representative voltage. However, the data should be repeatable with very low scatter.

In the present study, calibration has been performed in the wind tunnel itself due to its high quality inflow. The maximum turbulence level is 0.01% . The velocity profiles are uniform within 2% of the 90% cross section of the inflow section.

Isothermal Calibration of Hotwire

DISA hotwire equipment uses a linearizer card (56 N 21) which produces a voltage signal linearly proportional to flow velocity. The mathematical curve used by this card is given below.

$$y = 10^{A+Bx+Ey} + Cx + D \tag{3.11}$$

Here A, B, C, D and E are constants. Normally constants are selected to give a fluid velocity equal to 10m/sec for a wire output of 10 V. y is the linearizer output equal to normalized velocity of fluid defined as,

$$y = 10 \times \frac{U}{U_{max}} \tag{3.12}$$

and x is normalized voltage defined as,

$$x = 10 \times \left[\frac{V - V_0}{V_{max} - V_0} \right] \tag{3.13}$$

where V_0 is the output of wire measured at zero velocity of fluid and V_{max} measured at maximum velocity of fluid U_{max}.

The constants A, B, C, D and E are obtained by means of iterative least square error approach. For any calibration point (x_i, y_i) Equation 3.11 will produce an error ϕ_i given by

$$\phi_i = y_i - \left[10^{A+Bx_i+Ey_i} + Cx_i + D \right]. \tag{3.14}$$

The least square approach requires the sum of errors at all calibration points to

be minimum *i.e.*,

$$\Phi = \sum_{i=1}^{n} \phi_i = \sum_{i=1}^{n} \left\{ y_i - \left[10^{A+Bx_i+Ey_i} + Cx_i + D \right] \right\}^2 \qquad (3.15)$$

and

$$\frac{\partial \Phi}{\partial A} = \frac{\partial \Phi}{\partial B} = \frac{\partial \Phi}{\partial C} = \frac{\partial \Phi}{\partial D} = \frac{\partial \Phi}{\partial E} = 0. \qquad (3.16)$$

Let I be any of the parameters A, B, C, D or E, then

$$\frac{\partial \Phi}{\partial I} = 2 \sum_{i=1}^{n} \phi_i \frac{\partial \phi_i}{\partial I} = 0 \qquad (3.17)$$

Hence A, B, C, D and E can be calculated using iterative least squares.

Table(I) shows a typical calibration data and 3.1 shows calibration curve used for data analysis. All the data have been nomalised for a wire output of $0 - 10$ volts and velocity normalized for $0 - 10$ m/sec. Before normalization the data are fitted to a curve for linearization.

Table I:Normalized Calibration data for hotwire measurement.

Sl.no.	Volts	True(m/s)	calib(m/s)	% error
1	0.00000	0.79726	0.73765	7.47715
2	1.60543	1.38091	1.44705	-4.78995
3	3.08366	2.16534	2.20584	-1.87026
4	3.94008	2.71000	2.71793	-0.29266
5	4.98869	3.47402	3.44935	0.71035
6	6.13058	4.45860	4.42351	0.78720
7	6.96156	5.30813	5.28485	0.43851
8	7.83776	6.36478	6.36590	-0.01760
9	8.88355	7.90788	7.93135	-0.29678
10	9.20011	8.44893	8.47095	-0.26063
11	10.00000	10.00000	9.98116	0.18836

Calibration of hotwire in isothermal flow measurement is relatively easy. Measurement of non-isothermal flows requires a calibration curve which can include effect of fluid temperature.

To check the correctness and accuracy of the calibration procedure, the following tests were carried out. Uniform flow with adjustable temperature was produced in the test sections. The free-stream turbulence was less than 0.5%. The fluid velocity was measured with the hotwire as well as a pitot-static tube connected to a digital manometer readings. A comparison between the two sets of measurements is shown in Table (II).
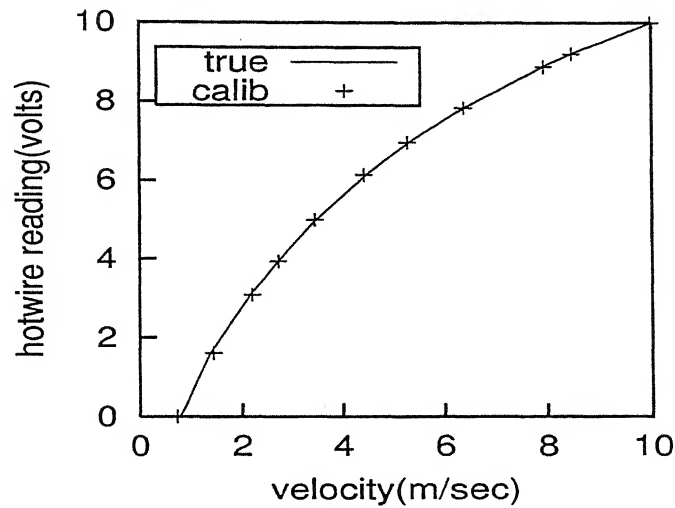
Figure 3.1: Normalized calibration plot for hotwire measurements.

Table II: Testing of calibration procedure

Room Temperature 19 °C					
T °C	34.3	39.0	41.5	43.2	43.8
Pitot Static Tube	3.65	4.14	3.75	4.26	3.22
Hotwire	3.67	4.06	3.74	4.30	3.21

This table shows an error of 1% in the hotwire measurements with respect to the pitot tube. This is an improvement over errors of 5-10% reported in the literature.

3.2 Data Reduction

For a single sensor hotwire normal to the flow with its prongs parallel to the flow, substitution of hotwire output or hotwire output and local fluid temperature in calibration curve directly gives the velocity of flow. For measurements in two and three dimensions, the contribution to the heat loss by the component of velocity normal to the wire and prongs and velocity component parallel to the wire must be included. A cross-wire sensor with two or three wires is designed for use in two and three dimensional flow measurements. Each wire is separately calibrated

and corresponding calibration curve and constants are evaluated. Substitution of output of a wire in its calibration gives effective cooling velocity sensed by the wire. The definition of effective cooling velocity is as follows. The components of velocity can be resolved into components normal to the wires and parallel to them. The effect of cooling by other two components of velocity can be accounted for by using sensitivity coefficients K_N and K_T. Experiments of Butler and Wanger (1982) and many others suggested a value of K_N ranging from 1.0-0.85 and K_T ranging form 0.1 to 0.25. A value of K_N=0.9 and K_T=0.20 are found to be optimum. The effective cooling velocity sensed by each wire is

$$V_e^2 = V_N P^2 + K_N^2 V_N N + K_T^2 V_T^2 \qquad \text{Three-dimensional flow} \qquad (3.18)$$

$$V_e^2 = V_N P^2 + K_T^2 V_T^2 \qquad \text{Two-dimensional flow} \qquad (3.19)$$

where V_e is the effective cooling velocity, $V_N P$ is the velocity component normal to the wire but parallel to the prongs, V_T is the velocity component tangential to the wire and $V_N N$ is the velocity component normal to both wire and prongs. Measurement of two and three dimensional flows involves calculation of components of velocity along laboratory coordinates. Many techniques are available in literature to get the components of velocity from known effective cooling velocities. Only two-dimensional flow measurement techniques are described in this chapter.

3.2.1 Hotwire Signal Analysis

Chew and Simpson (1988) have proposed an explicit non-real time method of reducing triple sensor hotwire anemometer data to obtain the three mean velocity components and six Reynolds stresses in 3-dimensional flow. This method does not require instantaneous signal to calculate parameters referred above. This method has been applied to a two-wire probe in the present chapter.

With reference to Figure 3.2, for wire 1 the normal velocity component V_{NN} is $(u \cos\alpha - v \sin\alpha)$ and the tangential velocity component V_T is $(u \sin\alpha + v \cos\alpha)$. The heat transfer coefficient associated with each velocity component is different. Hence the effective velocities v_1 and v_2 sensed by wire 1 and wire 2 are written
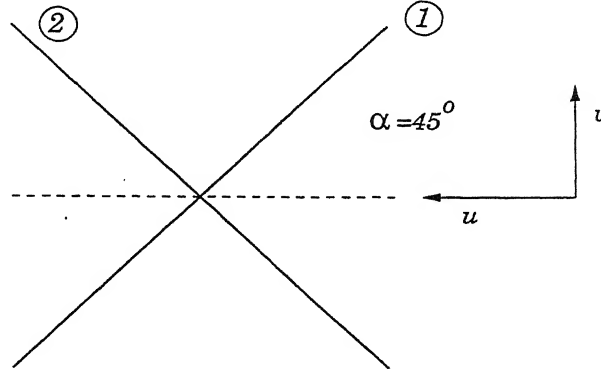
Figure 3.2: Cross wire probe and velocity components

as,

$$v_1^2 = \left[(u\cos\alpha - v\sin\alpha)^2 + K_T^2(u\sin\alpha + v\cos\alpha)^2\right] \qquad (3.20)$$

$$v_2^2 = \left[(u\sin\alpha + v\cos\alpha)^2 + K_T^2(u\cos\alpha - v\sin\alpha)^2\right] \qquad (3.21)$$

Generally cross-wires manufactured with the angle between wires $2\alpha = 90°$. With $\alpha = 45°$ above equations can be simplified as,

$$v_1^2 = \frac{1}{2}\left[(u - v)^2 + K_T^2(u + v)^2\right] \qquad (3.22)$$

$$v_2^2 = \frac{1}{2}\left[(u + v)^2 + K_T^2(u - v)^2\right] \qquad (3.23)$$

The factor K_T takes into account the differences in the heat transfer coefficient between cross flow and parallel flow. Let $v_x = \frac{u+v}{\sqrt{2}}$ and $v_y = \frac{u-v}{\sqrt{2}}$. Substituting in Equations 3.22 and 3.23, we get

$$v_1^2 = v_y^2 + K_T^2 v_x^2 \qquad (3.24)$$

$$v_2^2 = v_x^2 + K_T^2 v_y^2 \qquad (3.25)$$

Hence, inversion of Equations 3.24 and 3.25 gives,

$$v_x^2 = a_1 v_1^2 + a_2 v_2^2 \qquad (3.26)$$

$$v_y^2 = b_1 v_1^2 + b_2 v_2^2 \qquad (3.27)$$

where $a_1 = b_2 = \frac{1}{1-K_T^4}$ and $a_2 = b_1 = \frac{-K_T^2}{1-K_T^4}$.

The instantaneous velocity components u and v can be calculated using v_x and v_y as,

$$u = \frac{v_x + v_y}{\sqrt{2}}$$

$$v = \frac{v_x - v_y}{\sqrt{2}}$$

The instantaneous components of velocity signals $u(t)$ and $v(t)$ can be used to calculate the time averaged quantities. Any variable in above equation can be split into a mean and a fluctuating part as $v = V + v'$. Splitting all variables in Equations 3.26 and 3.27 and carrying out a time average, we get,

$$V_x^2 + \overline{v_x'^2} = a_1 \left(V_1^2 + \overline{v_1'^2} \right) + a_2 \left(V_2^2 + \overline{v_2'^2} \right) \tag{3.28}$$

$$V_y^2 + \overline{v_y'^2} = b_1 \left(V_1^2 + \overline{v_1'^2} \right) + b_2 \left(V_2^2 + \overline{v_2'^2} \right) \tag{3.29}$$

Let

$$V_{x0}^2 = a_1 V_1^2 + a_2 V_2^2 \tag{3.30}$$

$$V_{y0}^2 = b_1 V_1^2 + b_2 V_2^2 \tag{3.31}$$

$$\overline{v_{x0}^2} = a_1 \overline{v_1'^2} + a_2 \overline{v_2'^2} \tag{3.32}$$

$$\overline{v_{y0}^2} = b_1 \overline{v_1'^2} + b_2 \overline{v_2'^2} \tag{3.33}$$

Then

$$\overline{v_x'^2} = \overline{v_{x0}^2} + V_{x0}^2 - V_x^2 \tag{3.34}$$

$$\overline{v_y'^2} = \overline{v_{y0}^2} + V_{y0}^2 - V_y^2 \tag{3.35}$$

Rewrite Equations 3.28 and 3.29 as

$$V_x + v_x' = \left[V_{x0}^2 + 2a_1 V_1 v_1' + 2a_2 V_2 v_2' + a_1 v_1'^2 + a_2 v_2'^2 \right]^{1/2} \tag{3.36}$$

$$V_y + v_y' = \left[V_{y0}^2 + 2b_1 V_1 v_1' + 2b_2 V_2 v_2' + b_1 v_1'^2 + b_2 v_2'^2 \right]^{1/2} \tag{3.37}$$

Expanding in binomial series, taking time mean and neglecting terms higher than v'^2 gives

$$V_x = V_{x0} \left[1 + \frac{\overline{v_{x0}^2}}{2V_{x0}^2} - \frac{\sigma_x^2}{8V_{x0}^4} \right] \tag{3.38}$$

Here,

$$V_{x0} = \sqrt{a_1 V_1^2 + a_2 V_2^2}$$

$$\overline{v_{x0}^2} = a_1 \overline{v_1'^2} + a_2 \overline{v_2'^2}$$

$$\sigma_x^2 = 4 \sum_{i=1,2} \sum_{j=1,2} a_i a_j V_i V_j \overline{v_i' v_j'}$$

$$Similarly, V_y = V_{y0} \left[1 + \frac{\overline{v_{y0}^2}}{2V_{y0}^2} - \frac{\sigma_y^2}{8V_{y0}^4} \right] \tag{3.39}$$

where

$$V_{y0} = \sqrt{b_1 V_1^2 + b_2 V_2^2}$$

$$v_{x0}^2 = b_1 \overline{v_1'^2} + b_2 \overline{v_2'^2}$$

$$\sigma_y^2 = 4 \sum_{i=1,2} \sum_{j=1,2} b_i b_j V_i V_j \overline{v_i' v_j'}$$

The product of v_x' and v_y' can be calculated using the expression,

$$\overline{v_x' v_y'} = \frac{\sum_{i=1,2} \sum_{j=1,2} a_i b_j \left(V_i^2 V_j^2 + V_i^2 \overline{v_j'^2} + V_j^2 \overline{v_i'^2} + 4.0 V_i V_j \overline{v_i' v_j'} \right)}{4 V_x V_y}$$
$$- \frac{\left(V_x^2 V_y^2 + V_x^2 \overline{v_y'^2} + V_y^2 \overline{v_x'^2} \right)}{4 V_x V_y} \tag{3.40}$$

The velocity components in laboratory coordinates U and V and turbulence quantities u_{rms}, v_{rms} and $\overline{u' v'}$ can be calculated from the above variables using following formulae.

$$U = \frac{V_x + V_y}{\sqrt{2}} \tag{3.41}$$

$$V = \frac{V_x - V_y}{\sqrt{2}} \tag{3.42}$$

$$u_{rms}^2 = \frac{\overline{v_x'^2} + \overline{v_y'^2} + 2\overline{v_x' v_y'}}{2} \tag{3.43}$$

$$v_{rms}^2 = \frac{\overline{v_x'^2} + \overline{v_y'^2} - 2\overline{v_x' v_y'}}{2} \tag{3.44}$$

and

$$\overline{u' v'} = \frac{\overline{v_x'^2} - \overline{v_y'^2}}{2} \tag{3.45}$$

The method mentioned above does not require instantaneous signal and equipment to collect instantaneous signal, but involves complex mathematical equations. This method requires measurement of mean output of wire 1 and 2 namely V_1 and V_2, RMS values of their fluctuations $v_{1\,rms}$ and $v_{2\,rms}$ and the cross product

$\overline{v_1' v_2'}$. Inaccurate measurement of these turbulent quantities will produce imaginary numbers owing to the square root sign. Simple method which indirectly calculate components of velocity along laboratory coordinate is discussed below. This will contain simple mathematics but is an approximate method. However when turbulence levels are low this will predict the answers with a small error.

3.2.2   Strouhal Number

The frequency of vortex shedding has been measured by collecting a long signal and doing Fast Fourier Analysis (FFT) on it. Signal has been collected through A/D card using LabVIEW software. Strouhal number has been measured at $X = 5B$ and at $X = 10B$ location. The FFT algorithm has also been used to calculate power spectra . For both the cases long signal, 10,000 data points with sampling frequency of 10,000 were used.

$$Strouhal \ \ number = \frac{fD}{U_\infty}$$

where f is the vortex shedding frequency.

D is the projected area normal to the flow direction.

U_∞ is the free stream velocity.

3.2.3   Time Averaged Quantities

In experiments with low as well as high velocities, the velocity fluctuations close to the cylinder are expected to be large. Under these conditions, data reduction using the fixed operating point approach for gradient calculation is questionable. In the present experiments, the first measurement location was at $x=3.0$ and a definite positive value of the mean velocity was recorded. Hence on no occasion was the calibration curve utilized close to zero velocity. Secondly, the instantaneous voltage signal of the anemometer was converted to pointwise velocity and subsequently the time-averaged values were computed. This procedure circumvented the need to differentiate the hotwire calibration curve. The conversion of anemometer voltages to velocities was accomplished through an explicit non-real

time method developed by Chew and Simpson(1988). This technique has the advantage of determining the mean and the fluctuating components of velocity as well as their cross-correlations with very few assumptions regarding probe parity and the turbulence level.

Velocity and velocity fluctuations in the wake of the square cylinder were measured beyond a dimensionless distance of $x = 3.0$. In view of the insensitivity of the hotwire probe to reversed flow, measurements in the recirculation region of the cylinder are questionable. Earlier studies show the size of the base recirculation region at high Reynolds numbers to be in the range 1.3-1.4 (Lyn *et al.* (1995); Durao *et al.* (1988)). The recirculation zone has been established in these studies through alternative techniques such as the LDV and the flying hotwire. Additional discussion on measurements of large fluctuations in low velocity zones is provided by Swaminathan *et al.* (1986). These authors have shown that the turbulence correction factor in the time-averaged quantities to be less than 10 % for a turbulence intensity as high as 45 %. In the present work, the largest velocity fluctuation was recorded at the first station to be 30 %. Thus the choice of the measurement station for the time-averaged velocity as 3.0 can be taken as an acceptable starting point. All the quantities were averaged over 100 seconds.

3.2.4 Power Spectra

Power spectra were determined by first converting the anemometer voltage signals to velocity, and subsequently applying the FFT algorithm. A sampling frequency of 5 kHz was employed during A/D conversion. The total signal length was 13.2 seconds, yielding a total of 66,000 points in the time series. The data set was split into 8 parts for the calculation of the spectrum that was later averaged. This procedure was found to yield a useful frequency range of 0.1 Hz to 1 kHz. For Strouhal number calculations, the vortex shedding frequency was measured at an offset location of $x=5$, $y=1.2$. Here x and y have been nondimensionalized with respect to the cylinder size. The offset location was seen to produce clear peaks in the power spectra at the shedding frequency.

Errors in measurement can arise due to (i) positional accuracy in locating the probe, (ii) drift in electronics and consequent errors in voltage measurements, (iii) errors in calibration data and inadequate compensation for room temperature,

(iv) inadequate signal length and sampling rate, and (v) errors associated with neglecting the span-wise components of velocity during data reduction.

In a classical sense, it was not possible to repeat precisely identical experiments, mainly due to the difficulty in establishing identical inflow velocity and ambient temperatures. Instead, the approach adopted was to perform the experiments at a nearby Reynolds number approximately 10% away from the desired value. The two sets of data were then compared in terms of the dimensionless velocity and velocity fluctuations. The agreement between the two sets of data was found to be very good. In this sense the results reported in the present work have a high degree of repeatability. The difference in the time-averaged quantities between Re=4990 and 9980 is also quite small, indicating low levels of uncertainty in the present set of experiments. Based on this criterion, uncertainty levels of ± 5 % and ± 10 % can be assigned to the time-mean and RMS velocities.

3.3 Drag Coefficient

Mean velocity profile across the wake, distribution of the stream-wise momentum, and the loss of momentum are the three parameters that describe the mean flow structure in the near wake. In the present work, the momentum loss in the near wake has been measured and a dimensionless drag coefficients has been calculated by wake survey method. Generally this method is used to calculate drag coefficient from the velocity profiles measured at positions where there is no pressure variation across the wake. But in the case of a square cylinder, the static pressure variations have been observed even at twenty cylinder width downstream of the cylinder. Therefore it is necessary to consider the static pressure variation in the calculations. The drag coefficient is then given by the formula

$$C_d = \frac{\int_{\infty}^{\infty} (\rho u(y)(U_a - u(y)) + \Delta p) dy}{0.5 \rho U_a^2 D}$$

where $u(y)$ is the velocity profile in the wake, U_a is the approach velocity, D is the projected area of the cylinder normal to flow direction and Δp is the static pressure drop between the free stream and the point under consideration.

3.4 Laser Schlieren Principle

Schlieren method depends on deflection of a ray of light from its undisturbed path when it passes through a medium in which there is a component of the gradient of refractive index normal to the ray.

Relationship between the refractive index n and density ρ is

$$\frac{n^2 - 1}{\rho(n^2 + 2)} = \text{constant} \tag{3.46}$$

holds for transparent media. For gases, the refractive index is close to unity and the expression reduces to

$$\frac{n - 1}{\rho} = \text{constant} \tag{3.47}$$

where ρ is the density of the fluid. This relationship is called the Gladstone-Dale equation (Goldstein, 1983). It follows that $dn/d\rho$=constant. Now for moderate changes in temperature, density varies linearly with temperature as

$$\rho = \rho_o(1 - \beta(T - T_o)) \tag{3.48}$$

Hence dn/dT is also a constant. This implies that changes in temperature simultaneously result in changes in refractive index and this leads to changes in the phase of the wave.

The Schlieren method depends on deflection of a ray of light its undisturbed path when it passes through a medium in which there is a component of the gradient of refractive index normal to the ray. If the Z axis is taken of the direction of the undisturbed ray then the total angular deflection measured beyond the working section of the wind tunnel in XZ and YZ planes denoted respectively as ϵ_x and ϵ_y are:

$$\epsilon_x = \frac{1}{n_o} \int \frac{\partial n}{\partial x} dz$$

$$\epsilon_y = \frac{1}{n_o} \int \frac{\partial n}{\partial x} dz$$

where, n_o is the refractive index of the air surrounding the tunnel.

The contrast(C) of the image with respect to the background and the contrast sensitivity(S) are given by (Holder and North(1963))

$$C = \frac{\partial I}{I} = f_2 \frac{\partial \epsilon}{a}, S = \frac{\partial C}{\partial \epsilon} = \frac{f_2}{a}$$

where, f_2 is the focal length of the 2nd mirror, a is the height of the image not cut off by the knife edge and $\partial \epsilon$ is the angular deflection of the light ray. The range of angular deflection such that the image of the source is not completely displaced off (the illumination is same as in the absence of knife edge) or on the opaque side of the knife edge (complete dark on the screen) is given by (Holder and North(1963)): $Range = (h/f_1)$ Where, h is the height of the light source and f_1 the focal length of the first mirror. For two dimensional disturbances extending across the working section from one glass window to other, the light entering the disturbance remains within it, and are continuously deflected across the whole width of the tunnel. Thus the final deflection of the light rays is proportional to the tunnel width. Thus as the width of the tunnel is increased, the range of the deflections which the Schlieren apparatus has to detect become smaller and difficulties associated with the achievement of a satisfactory compromise between range and sensitivity become less severe.

3.4.1 Quantitative Analysis

Figure 3.3 shows a part of the Schlieren set-up that is just beyond the test- section region. As shown the knife-edge is placed on the focus of the lens. When the knife-edge is moved across the beam exactly at the focus, the illumination at the screen should decrease uniformly; if the knife-edge is not in the focal plane, then the image at the screen will not darken uniformly, rather the Schlieren pattern will be dominated by the shadowgraphy effects.

Let $\triangle a$ be the deflection of the light beam in the vertical direction above the knife-edge once the disturbance has been introduced in the test region. α be the angle that this deflected ray makes with the original light beam passing through the test region but without any disturbance.

For small deflection α,

$$\alpha'' = \beta - \gamma$$

$$= \frac{\triangle y}{f} - \frac{\triangle y}{q} = \triangle y \left[\frac{1}{f} - \frac{1}{q} \right]$$
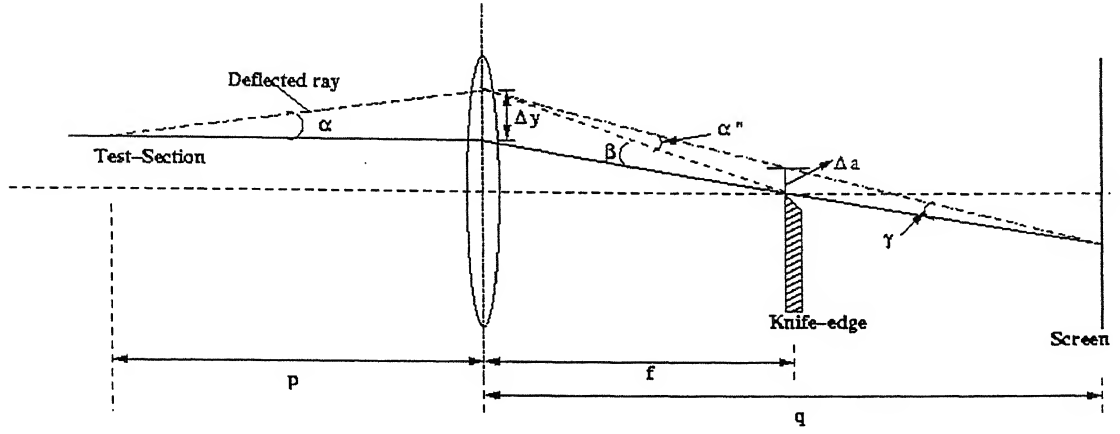
$$= \frac{\triangle y}{p} = \alpha$$

Figure 3.3: Schematic diagram showing region beyond the test section in a Schlieren set-up.

Now, the vertical shift of the light beam above the knife-edge due to the disturbance can be expressed in terms of the angular deflection as

$$\frac{\triangle a}{f} = \alpha'' = \alpha$$

$$\triangle a = \alpha \times f$$

The knife-edge is adjusted when no disturbance is present to cut-off approximately 50% of the original light falling on the screen.

Let I_o be the original intensity falling on the screen when no disturbance is present in the path of the laser beam and I_k be the intensity after putting the knife-edge to block a desired amount of light beam.

Let a_o be the original dimension of the beam perpendicular to the knife-edge and a_k be the corresponding dimension after cutting-off the light beam by the knife-edge (Figure 3.4).

Then,

$$I_k = \frac{a_k}{a_o} \times I_o$$

Now, if the light beam is deflected by an angle α after putting the test region, then the vertical shift of the beam above the knife-edge will be $\triangle a$(as calculated
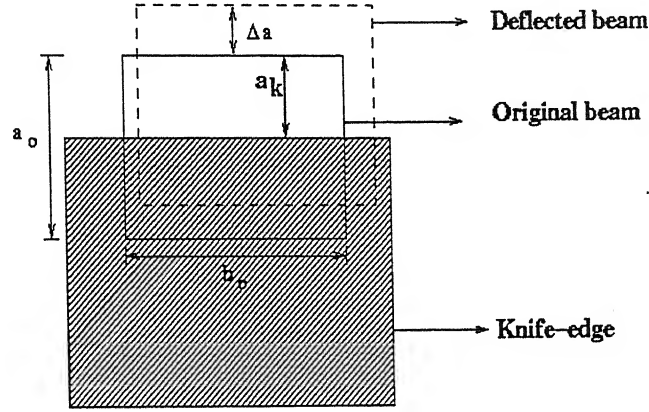
Figure 3.4: Schematic diagram showing the vertical shift of the beam above the knife-edge.

above). With the disturbance in place, the intensity on the screen will be

$$I_D = \frac{a_k + \triangle a}{a_k} \times I_k = \left[1 + \frac{\triangle a}{a_k} \right] \times I_k$$

Therefore, change in intensity, $\triangle I$

$$\triangle I = I_D - I_k = I_k \left[\frac{\triangle a}{a_k} \right]$$

The relative intensity or contrast is

$$\text{Contrast,} \quad \frac{\triangle I}{I_k} = \frac{\triangle a}{a_k} = \frac{\alpha \times f}{a_k}$$

For a given optical system, minimizing a_k by the movement of the knife-edge would maximize the contrast as seen from the above expression. However, this would limit the range for deflection of the beam towards the knife-edge as all the deflections lower than this maximum value of α would give no illumination on the screen since these will be blocked by the knife-edge itself before falling on the screen.

Now suppose that half of the light beam is blocked by the knife-edge i.e. $a_k = \frac{a_o}{2}$. Then,

$$\frac{\triangle I}{I_k} = \frac{2f\alpha}{a_o} \tag{3.49}$$

$$\tag{3.50}$$

Let Z be the direction of propagation of the light beam and X and Y are the other two perpendicular axes. Initially let us assume that the disturbance in the test region is purely one dimensional and is in the Y-plane vertically upwards the knife-edge.

Using the principles of ray-optics, it can be shown that the small angular deflection, $d\alpha$ of the light ray as it passes through the test region can be expressed as,

$$d\alpha = \frac{1}{n_o}\frac{\partial n}{\partial y}dz = \frac{\partial ln(n)}{\partial y}dz$$

where n_o is the refractive index of the medium under study.

Let L be the length of the test section along the direction of the beam in which it encounters a change in the refractive index, then the total angular deflection α can be expressed as

$$\alpha = \frac{1}{n_o}\int_0^L \frac{\partial ln(n)}{\partial y}dz$$

Using Equation 3.49,

$$\alpha = \frac{a_o}{2f}\frac{\Delta I}{I_k} = \frac{1}{n_o}\int_0^L \frac{\partial ln(n)}{\partial y}dz$$

$$\frac{\Delta I}{I_k} = \frac{2f}{a_o}\frac{1}{n_o}\int_0^L \frac{\partial ln(n)}{\partial y}dz \tag{3.51}$$

Hence

$$\int_0^L \frac{\partial ln(n)}{\partial y}dz = \frac{\partial ln(n)}{\partial y}L$$

Therefore Equation 3.51 becomes

$$\frac{1}{n_o}\frac{\partial ln(n)}{\partial y}L = \frac{a_o}{2f}\frac{\Delta I}{I} \tag{3.52}$$

The above equation corresponds to the knife-edge orientation kept horizontal and assuming that the disturbance in the test region is purely one-dimensional. Now, if the disturbance in the test region is two-dimensional, then to capture the deflection of the beam in the X direction, the knife-edge is to be oriented in the vertical direction.

Following the same practice as described for the one-dimensional case and extending it to the other dimension, one can derive the similar expression as given by Equation 3.52,

$$\frac{1}{n_o}\frac{\partial ln(n)}{\partial x} = \frac{b_o}{2fL}\frac{\triangle I}{I}$$ (3.53)

where b_o is the dimension of the beam perpendicular to the knife-edge as shown in Figure 3.4 when the knife-edge is kept vertical.

In order to get the refractive index field in a two-dimensional field of disturbance, Equations 3.52 and 3.53 can be added and solved. Hence the final expression can be written as

$$\bigtriangledown ln(n) = f(x, y)$$ (3.54)

where $f(x, y)$ is the sum of the right hand sides of Equation 3.52 and 3.53. Equation 3.54 can be solved using any of the iterative numerical techniques.

3.5 Nusselt Number

The average heat transfer coefficient (h) of the cylinder is obtained by using :

$$h = (Q - Q_{rad} - Q_{endloss})/A(T_s - T_\infty)$$ (3.55)

where, Q is the energy input to the cylinder, T_s is the temperature of the cylinder, T_∞ is the temperature of the ambient air, Q_{rad} is the radiation loss and $Q_{endloss}$ is the end loss from the heated cylinder. Power supplied to the heating coil was measured by measuring current (I) and voltage (V) from the ammeter and voltmeter respectively connected to the heating arrangement. Experiments were carried out for a long period (400 sec) so that uncertainty in the experiment is minimum. Total amount of time for which the heater was on was observed from a LED display and recorded by a stop watch. Power input Q is calculated using:

$$Q = C \times V \times I$$ (3.56)

where, $C = t_{on}/(t_{off} + t_{on})$, t_{on} is the total time for which heater is on and t_{off} is total time for which the heater is off. Radiation losses is calculated from using:

$$Q_{rad} = \sigma\epsilon A(T_s^4 - T_\infty^4)$$ (3.57)

where σ is the Stefan Boltzmann constant, ϵ is the emissivity of the heated cylinder and A is the surface area of the cylinder. Nusselt number values obtained from the present study are compared with that from the empirical correlation:

$$\mathrm{Nu}^3 = \mathrm{Nu}^3_{forced} + \mathrm{Nu}^3_{free} \tag{3.58}$$

$$\mathrm{Nu}_{forced} = 0.683 \times \mathrm{Re}^{0.466} \times \mathrm{Pr}^{1/3} \tag{3.59}$$

$$\mathrm{Nu}^{1/2}_{free} = 0.60 + 0.387 \left(\frac{GrPr}{\left(1 + (0.559/Pr)^{9/16}\right)^{16/9}} \right)^{1/6} \tag{3.60}$$

where Grashoff number $(Gr) = g\beta(T_s - T_\infty)d^3/\nu^2$, Prandtl number $(Pr) = \mu C_p/k$, Reynolds number $(Re) = vd/\nu$, $\beta = 1/T_f$. C_p, ν and k are the fluid properties at the specified temperature.

3.6 Uncertainty Analysis

3.6.1 Uncertainty in Hotwire Experiment

It was not possible to produce identical velocity due to ambient temperature variation from day to day. The Reynolds number variation between any two days was approximately 10%. The two sets of data were compared in terms of dimensionless velocity and velocity fluctuations. The agreement between two sets of data was found very good. The repeatability of data over the Reynolds number range studied $1340 - 9980$ was found to be $\pm 5\%$ in time-averaged quantities and $\pm 10\%$ in rms quantities, (95% CI).

The sources of error in the experiments are: (i)errors in calibration data and inadequate compensation for room temperature (ii) positional accuracy in positioning the probe in the wind tunnel (iii) drift in electronics (iv) inadequate signal length and sampling rate mainly in rms component measurement (v) errors associated with assuming the flow as two dimensional. Due to this uncertainty the results obtained here can be considered to be qualitatively meaningful.

3.6.2 Uncertainty in Laser Schlieren Experiment

The factors responsible for error in laser schlieren measurements are: (i) parallelism of the light beam to the cylinder axis, But this could not achieved due to:

(a) building vibration (the laser beam which is very small in dia $(1-2mm)$ shifts and temperature variation causes sagging of base on which laser is placed), and

(b) positioning of the test cell

(ii) outside noise (The line voltage contaminate the signal as the signal strength is very low of the order of few millivolts),

(iii) diffraction effect from the knife edge and the model boundary,

(iv) variation of the cylinder temperature (There was a variation of $\pm(1-2)^{o}C$),

(v) drift in photodiode, photo amplifier, DAQ card and signal conditioner of temperature controller,

(vi) room temperature fluctuation, and

(vii) reflection from the optical window of the test cell.

Chapter 4

Results and Discussion

4.1 Unheated Cylinder

The wake behaviour behind the unheated square cylinder at different attack angle to the main flow is presented in the following sections. The Drag coefficient, Strouhal number, Reynolds stresses, time-averaged stream wise and transverse velocities, velocity time traces and power spectra results are presented and discussed. When ever possible, the results obtained in this work is validated and compared with the results from earlier investigations. Flow visualisation results are presented to corroborate or analyze the quantitative results.

4.1.1 Drag Coefficient

Time-averaged drag coefficients for a square cylinder at zero angle of incidence reported by various authors are summarized in Table 1. The highest Reynolds number in the referred studies is 13,000. For comparison, the drag coefficient obtained for the highest Reynolds number of the present work has also been included in Table 1. The agreement among the listed values including the present work is quite satisfactory. As discussed by Saha *et al.* (2000a), the dimensionless flow fields in the wake of a square cylinder are practically Reynolds number independent. It is primarily because the points of separation are fixed by its sharp corners facing the incoming flow. The near-constancy in the drag coefficient between Reynolds numbers of 500 and 13,000 can be traced to this factor.

A comparison of the time-averaged drag coefficients with the experiments of Norberg (1993) for cylinders at various angles of incidence is presented in Table 3. For a cylinder placed at an inclination to the main flow, the drag coefficient is

based on the projected dimension D, rather than the cylinder size B. All Reynolds numbers in the present work are based on the cylinder size B. At both Reynolds numbers considered Table 3, the drag coefficient shows a reduction with respect to the zero angle configuration, being a minimum at 45°. The reduction is around 40 % with respect to the zero angle configuration. It is practically equal to the increase in the projected area that is 41 %. Thus, in dimensional terms, there is no change in the drag force with the angle of incidence, at a given upstream velocity. Table 3 supports the result that the first order correction to the drag coefficient is contained in the change in the projected area. Factors such as the Reynolds number and the wake properties contribute to the second order.

4.1.2 Strouhal Number

The Strouhal numbers for the square cylinder wake at the lower and the higher ends of the Reynolds number range are summarized in Table 2. The angle of incidence is once again zero in this discussion. The vortex shedding frequency in the definition of Strouhal number is based on the time trace of the y-component of velocity. Table 2 shows that the extent of variation in the Strouhal number is greater, when compared to the drag coefficient. This can be explained by the fact that the shedding frequency in the near wake, and in turn the wake size is influenced by the upstream turbulence level and confinement effects. Moreover, frequency measurement in experiments is affected by probe-interference effects and the probe location. Table 2 however shows that the change in the Strouhal number is only marginal, when the Reynolds number is increased by as large a factor as 20. It is indicative of a nearly constant wake width, and is related to the fixed position of the separation points. The corresponding Strouhal numbers (based on B) as a function of angle and Reynolds number are presented in Table 4. The variation of Strouhal number with the angle θ is not monotonic. A change in the angle from 0 to 22.5° leads to a sharp reduction in the Strouhal number. Smaller changes are to be seen for other values of θ. For θ is 45°, the Strouhal number is high, but not necessarily a maximum. These results are quite visible in Norberg's experiments as well.

To examine the sensitivity of the measurement of vortex shedding frequency to the probe location, experiments were carried out at stations $x=5$ and 10 respec-

tively. Table 6 shows that the difference is quite small, particularly for higher Reynolds numbers. At Re=1340, the wake is in the transitional zone and exhibits dependence on the probe location. During experiments, it was found that the vortex shedding frequency at the lowest Reynolds number exhibited time-dependence as well, that in turn was a source of scatter. The flow complexity in the lower range of Reynolds numbers has been discussed by Saha *et al.* (2000b), and the references therein.

Table 6 records the Strouhal numbers Su and Sv when the vortex shedding frequency is obtained by locating the peak in the power spectrum of the u and v velocities respectively. For an object symmetric about the x-axis, it is to be expected that the two sets of Strouhal numbers would be equal. When the cylinder is oriented at an angle, a loss of symmetry is introduced and the two values may be unequal. Table 6 shows that the extent of variation between Su and Sv is quite small at angles other than zero as well. Measurable differences are seen only at the lowest Reynolds number studied. The orientation of 0 and 45° are both symmetric configurations, and the two Strouhal numbers are mostly equal. The greatest difference is to be seen at Re=1340, for an angle of 30°. The magnitude of the difference is however uniformly small. One can thus conclude that the time-dependent pressure field in the wake is set up for the cylinder as a whole. Under these circumstances, vortex shedding takes place with respect to the object as a whole, in the sense that the individual geometric features are not preserved.

To explain the trends in the drag coefficient and the Strouhal number with the incidence angle, flow visualization studies were carried out in a flow visualization facility at a Reynolds number of 3920. The recorded images are shown in Figure 4.1. A conclusion that emerges clearly from the figure is the following: For $\theta = 0$, the point of separation is at the left corners of the cylinder, namely those exposed to the approach flow. At higher angles, flow separation is delayed up to the cylinder corners on the downstream side. Hence, for all angles greater than zero, there is a reduction in the drag acting on the cylinder. The increase in the Strouhal number with the angle θ can be interpreted along the following lines. The movement of the separation points increases the wake size. On the other hand, the separated boundary layer from an inclined cylinder rolls up over a shorter distance in comparison to the wake size. The vortex shedding frequency correlates with the smaller of the length scales, namely the size of the rolled up

shear layer, as against the wake width. For $\theta = 0$, the wake width is the smaller length dimension and the vortex shedding frequency scales with this length scale. Thus, for angles of inclination greater than zero, the effective length scale of the shed vortex decreases, correspondingly increasing the shedding frequency and the Strouhal number. There are minor changes in the Strouhal number when θ increases from 22.5^o to higher values, but these changes are of smaller significance.

4.1.3 Time Averaged Wake Properties

The variation of the RMS lift coefficient with the cylinder orientation has been reported by Sohankar *et al.* (1998), and is reproduced in Figure 4.2. This result is numerically derived, and is applicable for Re=200. It can be seen that the RMS lift coefficient increases initially with θ, and levels off in the range 30-45°. Thus the wake may be considered to become increasingly vigorous for $\theta > 0$, reaching a maximum in the range 30-45°. The above result can be compared with the measurements of the present work by examining the variation of the RMS velocity fluctuations with θ. This comparison has been carried out with measurements at the location $x = 5$, and $y = 1.5$, where the vortex shedding frequency was determined. The x and y-components of velocity fluctuations as a function of the incidence angle are shown in Figure 4.2(b-d) for the three Reynolds numbers. At the lowest Reynolds number, u' increases with θ up to 30°, and subsequently decreases. On the other hand, v' remains relatively constant. At Re=4990, both fluctuations increase with θ up to 45°, and decrease for higher angles. However, at Re=9980, the velocity fluctuations show a monotonic reduction with the incidence angle. Thus a degree of similarity is to be seen between the numerical predictions Figure 4.2(a) and the experiments for Reynolds numbers up to 5000 Figure 4.2(b-c). The intensification of the wake for angles between 0 and 45° can be inferred from Figure 4.1 as well, by noting that the the size of the rolled up shear layer decreases for angle greater than zero, in comparison to $\theta = 0$. The deviation from this trend at the highest Reynolds number can be related to a a faster decay rate of the velocity fluctuations. The decay referred here is partly due to viscous dissipation; more importantly the transport of kinetic energy from the core of the wake to the outer flow is Reynolds number dependent (Saha *et al.*, 2000b).

The center-line recovery of the time-averaged velocities and their respective

RMS fluctuations are presented in Figure (4.5-4.9). Data has been presented beyond the base region of the cylinder ($x > 3$), for a dimensionless downstream distance of up to $x=20$.

The recovery of the time-averaged x and y components of the fluid velocity are shown in Figure (4.5-4.6). The x-velocity increases along the center-line and approaches an asymptotic value of unity, the approach velocity. The far wake tends to symmetric, irrespective of the object shape. Hence the y-velocity approaches zero in the downstream direction. The data in Figure (4.5-4.6) shows scatter, that tends to be higher at the lowest Reynolds number studied. A possible explanation for this trend could be the intrinsic three dimensionality and low frequency unsteadiness of the low Reynolds number wake, as well as probe interference effects. The recovery curves are more definite at higher Reynolds numbers. The overall trend seen in Figure 4.5 is that the x-velocity decreases initially beyond the base region of the wake, while the trend of recovery is initiated in the near wake, beyond $x=10$. It is in conformity with both experiments as well as computations over a wide range of Reynolds numbers, for an angle $\theta = 0$ (Lyn et al., 1995). The distance at which the recovery of the x-velocity is initiated is dependent on the incidence angle of the cylinder. The recovery rates in turn are also dependent on this angle, though in a non-monotonic manner. The slowest recovery is seen for $\theta = 45^o$, while the recovery rates are similar for the other angles. Figure 4.6 shows the recovery curves in the terms of the y-component of velocity for 5 orientations of the cylinder. The trends are seen to be quite similar, and a strong dependence on the incidence angle is not to be seen. A greater degree of scatter for the lowest Reynolds number is once again reproduced in the data.

The recovery of the time-averaged velocity components along the center-line is related quite closely to the wake dynamics. The loss of momentum of the fluid, that equivalently appears as forces acting on the cylinder, results in reduced velocities within the wake. For small values of x, the flow is dominated by transport of kinetic energy from the core of the wake to the outer flow (Townsend, 1949). While this factor leads to decay in velocity fluctuations, it can also result in a lowered time-averaged velocity. Farther away from the cylinder, the wake size and the center-line velocity increase, indicating that the wake entrains fluid from the outer flow. The transport of kinetic energy from within to the outer edges of the wake in the transverse direction generates non-zero vertical velocities, even

for the symmetric configuration of $\theta = 0$. For other angles, the transverse velocity is greater, but uniformly decreases with increasing distance from the cylinder.

The decay rates of the RMS velocity fluctuations u', v', and the time-average of $\overline{u'v'}$ are shown in Figure (4.7-4.9) respectively. The scale used for nondimensionalization is the approach velocity U, in all the figures. The decay rate of u' is marginally higher for the 45° angle, but the overall patterns in Figure 4.7 look similar for all angles and Reynolds numbers. The decay of v' is greater, as seen in Figure 4.8, but is the slowest for the 45° configuration. The cross-correlation $\overline{u'v'}$ is practically a constant at the lowest Reynolds number, but shows a strong dependence on the cylinder orientation at other Reynolds numbers. The magnitude of the cross-correlation however decreases in the downstream direction in all the experiments. The transverse profiles of the velocity fluctuations were seen to be flat at all measurement stations considered, except the first at $x = 3$. These profiles have not been reported in the present study.

The decay of fluctuations in the wake of the cylinder is partly due to viscous dissipation, but arises primarily from the transport of the kinetic energy of the fluctuations in the transverse direction. The transport is by the large scale vortices shed by the cylinder. This mechanism is also responsible for making the transverse profiles practically uniform. Marginal differences in the decay rates of the stream-wise fluctuation Figure 4.7 are related to (a) the shift in the point of separation, and (b) the change in the circulation strength of the shed vortices, with cylinder orientation. As seen in Figure 4.1, the separation point moves downstream for all angles greater than zero. The wake size increases with the angle θ, but the delay in the point of separation indicates a reduced drag (Table 5), a lowered momentum loss and hence a smaller velocity deficit in the wake. Since the strength of the circulation is roughly proportional to the flow blockage, factors (a) and (b) contribute to the decay rates of the fluctuations in conflicting terms. As a result, a dominant influence of the cylinder orientation is not felt in the evolution of the stream-wise velocity fluctuations. The transverse fluctuation essentially responds to changes taking place in the stream-wise component. At $\theta = 45^o$, the changes in the momentum deficit is a minimum, the time-averaged velocity undergoes smaller changes with distance Figure 4.5 and leads to lower decay rates in v' Figure 4.8.

The cross-correlation of the velocity fluctuations is related to the time-averaged

velocity gradient along the wake centerline only under (quasi-) fully developed conditions. The gradient goes to zero in the farwake, and consequently the cross-correlation attains small values. In developing flow, the correlation is determined by the individual mechanisms that produce u' and v'. The former is associated with the shear layer instability, while both components respond to the vortex transported from the base region of the cylinder into the far wake. Thus the correlation is retained when the vortex is strong, and weakens progressively in the farwake. Figure 4.9 shows that this picture is only marginally disturbed by a change in the cylinder orientation.

The time averaged velocity profile at two downstream location $x = 5, 18$ for all the angles $0, 22.5, 30, 45, 60$ and for all Reynolds number $Re = 1340, 4990, 9980$ are in Figure 4.3 and 4.4 respectively. At $x = 5$, the centerline velocity depends on the incident angle and Reynolds number as well. But at $x = 18$ this dependency become negligible as shown in figure (4.4).

The time-averaged vorticity profiles at three stream-wise distances are presented in Figure (4.10-4.12). Data has been presented for five cylinder orientations. Vorticity values have been derived by differentiating the time-averaged velocity data. Reynolds number of 1340, 4990 and 9980 has been considered. No significant change in the vorticity trends was seen at these Reynolds numbers. For all the cylinder positions, the vorticity profiles in Figure (4.10-4.12) show a maximum and a minimum, on each side of the centerline ($y = 0$). The magnitude of vorticity at these points diminishes with the x-distance, though gradually. The positions of the vorticity extrema are seen to shift with the stream-wise distance for $\theta = 0$, but for other cylinder angles the positions are practically fixed. This is an evidence of two oppositely oriented vortices being transported in the wake. The vortices are produced at the corners of the cylinder and have a tendency to get displaced inwards. owing to the lower pressures prevailing within the wake. This is counter-balanced by the growing wake size, which shifts the vortex centers outwards. Thus the vortices move practically along a straight path in the wake. For $\theta = 0$, the vortices emerge from the forward corners of the cylinder, as opposed to the rear corners for all other angles. The earlier separation for the non-inclined cylinder leads to a larger pressure deficit between the inner and the outer regions of the wake, and the vortices get visibly displaced towards the axis. Once the shed vortices come close to one another, they can be expected to merge

and move as a single entity. The peak in the vorticity profile would then be at $y = 0$.

4.1.4 Time Trace of Velocity Signal

Figure 4.17 shows the time trace of u and v component of velocity and corresponding power spectrum at $x = 18$ for $Re = 4990$. For $\theta = 60^\circ$, both the power spectrum and the velocity time traces show lower fluctuation magnitude than others. This indicates that the core region of the vortex is at a different transverse (Y) locations for $\theta = 60^\circ$ case. Figure (4.18-4.20) shows the time traces for $Re = 1340, 4990$ and 9980 at $x = 5, 10$ location. From the trace it shows that the v-fluctuation is more regular than the u-fluctuations. The u-fluctuations has more high frequency component superimposed on it than that of the v-component. The spectrum of the v-component of velocity is therefore seen to show the vortex shedding frequency in the far field region i.e. at x = 18, while there is no clear peak in the u-component of velocity. At $Re = 1340$ a low frequency unsteadiness is observed to be superimposed on top of the regular unsteadiness from the vortex shedding frequency, which is not seen at higher Reynolds number case.

4.1.5 Power Spectra

The dimensionless power spectra as a function of the dimensionless frequency are shown in Figure (4.13-4.15), for the three Reynolds numbers of the present study. Five angles of inclination have been included for comparison. The measured power spectra have been non-dimensionalized by the total area under the curve; thus in Figure (4.13-4.15), the area under the curve is unity. In this respect, the decay of the velocity fluctuations with distance is not visible in these figures. The vortex shedding frequency for all angles and Reynolds numbers is in the range 0.1-0.2, and is brought out by the spectral peaks. The peaks are quite clear at the two higher Reynolds numbers. At Re=1340, the peaks are smaller in comparison. The peaks of vortex shedding diminish rapidly with distance in the spectrum of the u-velocity, while they persist in the v-component of velocity. Thus, for all Reynolds numbers, the peaks in Ev are visible up to $x = 10$. Spectra in the v-component of velocity recorded at $x = 18$ continued to show peaks corresponding to vortex shedding, particularly at the two higher Reynolds numbers. A survey

of Figure (4.13-4.15) shows that the vortex shedding frequency is only a weak function of the angle θ and Reynolds numbers.

The wake at Re=1340 shows local peaks at higher frequencies at both locations x=5 and 10. These peaks were seen to persist farther downstream ($x = 18$). The spectra at higher Reynolds numbers did not show this behavior, and the high frequency data was reasonably monotonic. Recent literature on low Reynolds number wakes shows the possibility of three dimensional temporal structures even in nominally two dimensional geometries (Williamson, 1996). Thus it is likely that the energy cascade mechanism in the velocity fluctuations selectively energizes a few harmonics and the flow regime does not become turbulent in the classical sense. The inertial range of the spectra at higher Reynolds numbers shows a fully developed turbulent profile at $x = 10$ in the u-velocity and for $x > 20$ in the v-velocity, with no sign of vortex shedding. The influence of the cylinder orientation is only secondary in determining the shape of the spectra.
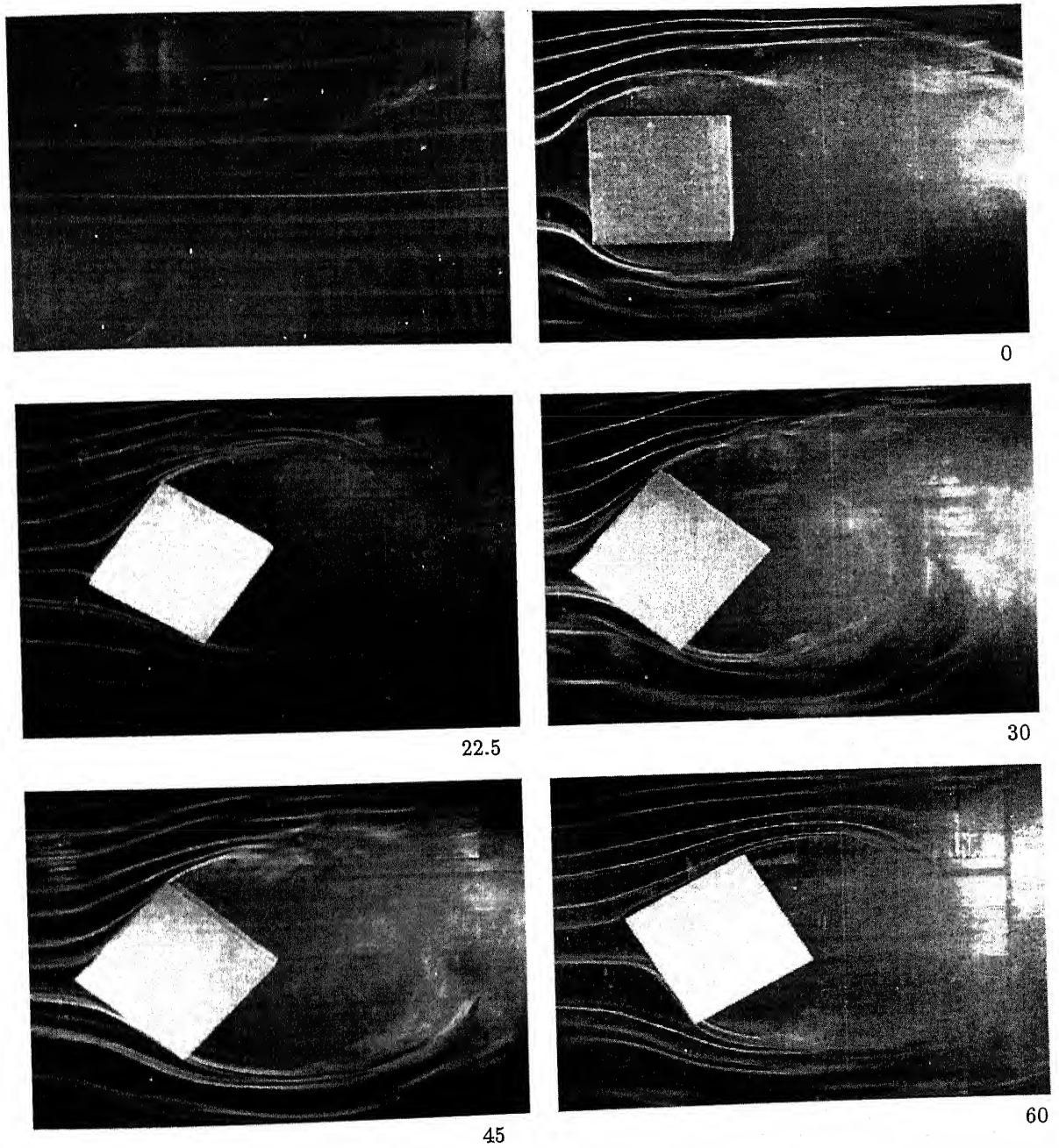
Figure 4.1: Visualization of flow around a square cylinder at various angles of incidence, Re=3920.
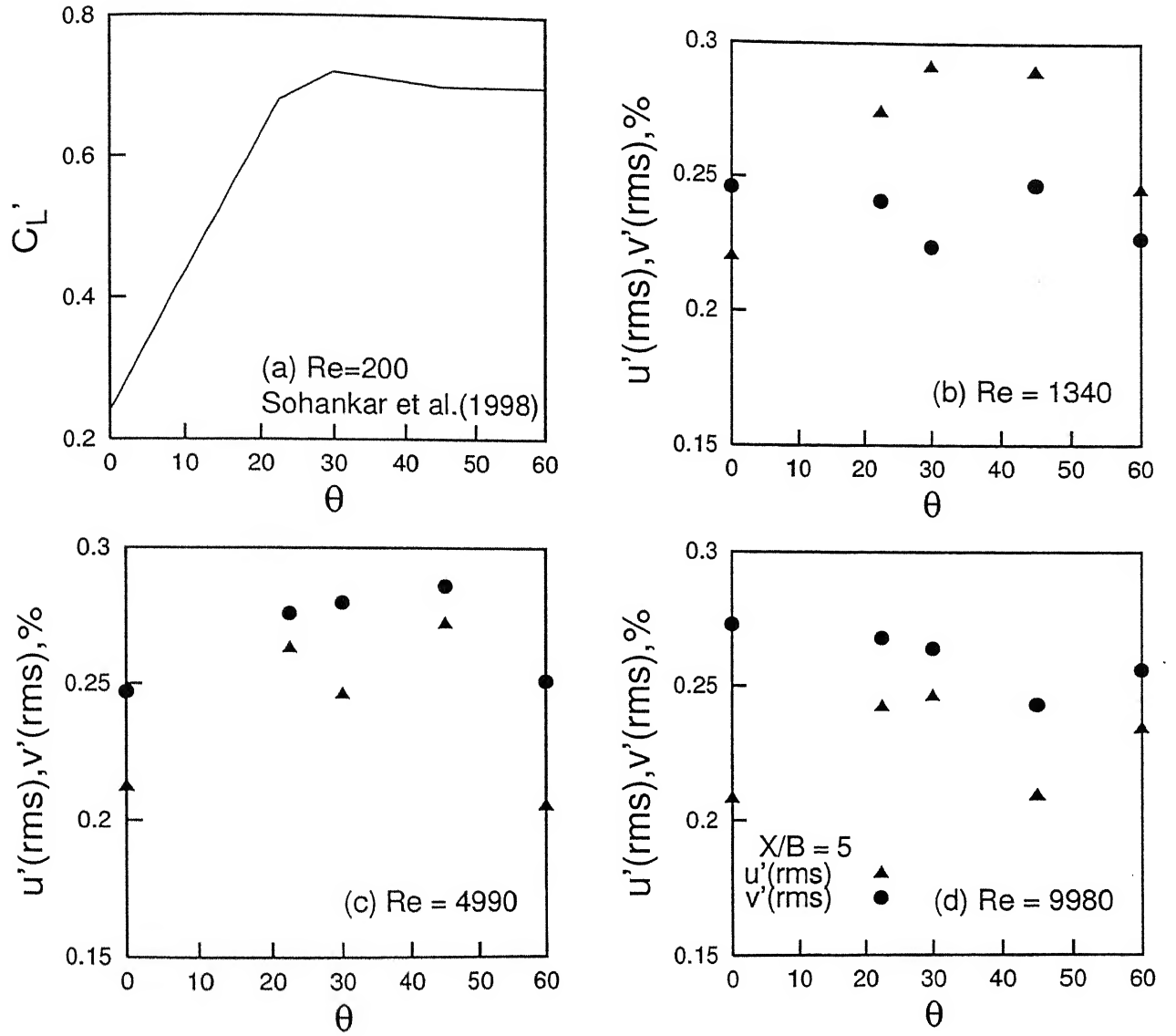
Figure 4.2: Comparison of the (a) numerically computed RMS lift coefficient at Re=200 (Sohankar et al.1998) with the RMS velocity fluctuations at Re=(b)1340, (c)4990 and (d) 9980.
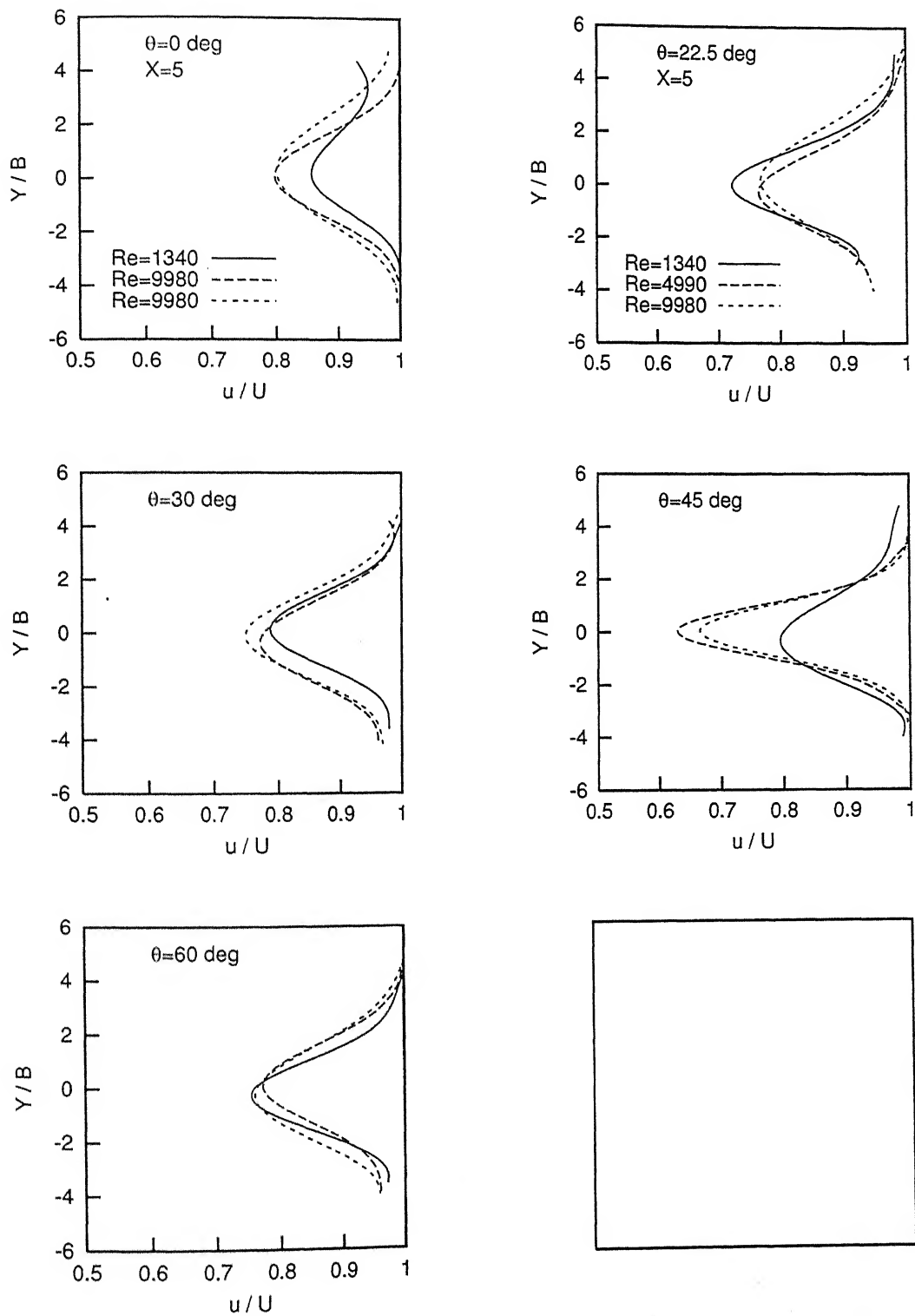
Figure 4.3: Velocity profile across the wake at $X = 5B$ for Reynolds Number 1340, 4990 and 9980 at angles θ=0, 22.5, 30, 45 and 60 deg.
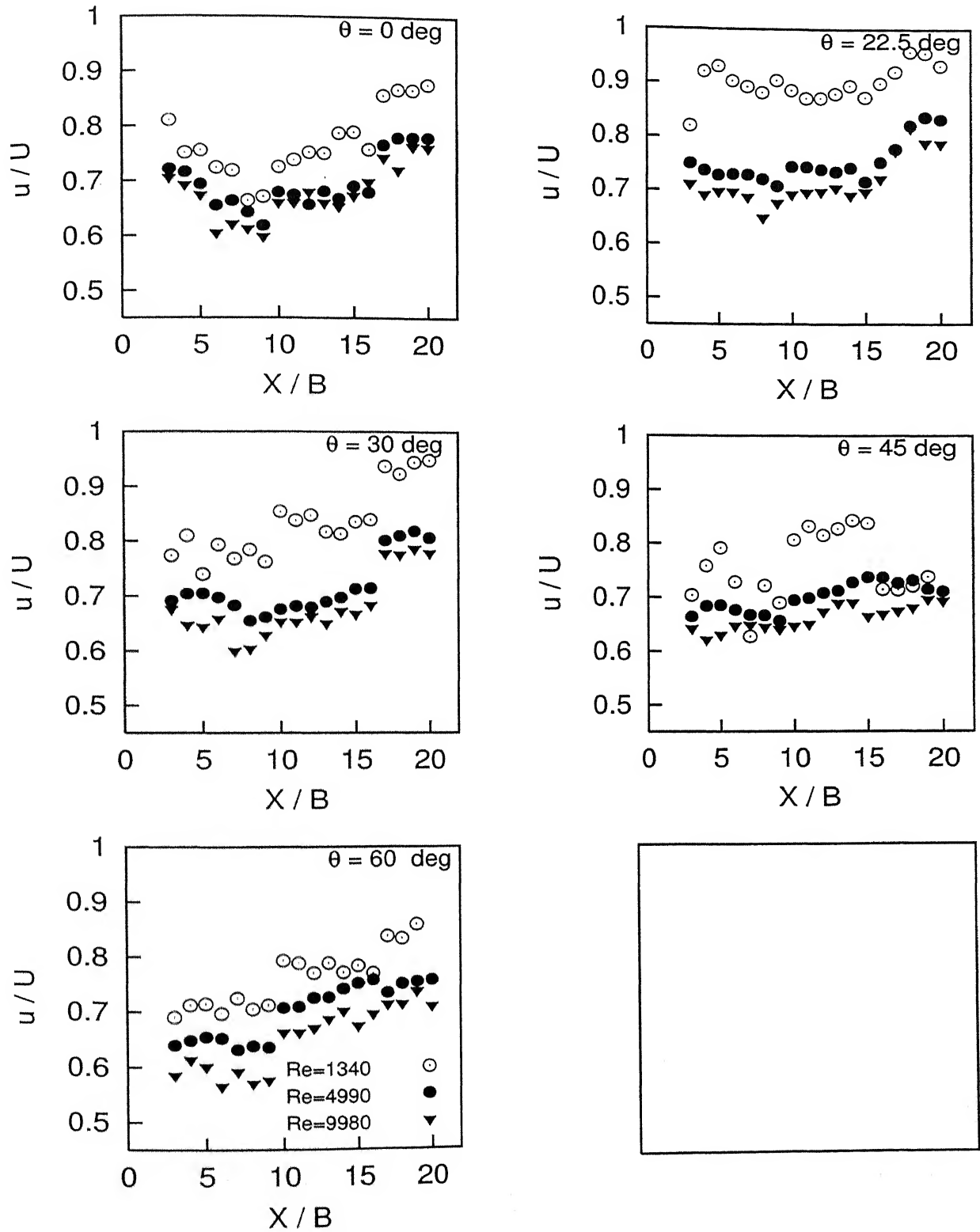
Figure 4.5: Center-line recovery of the time-averaged stream-wise component of velocity.
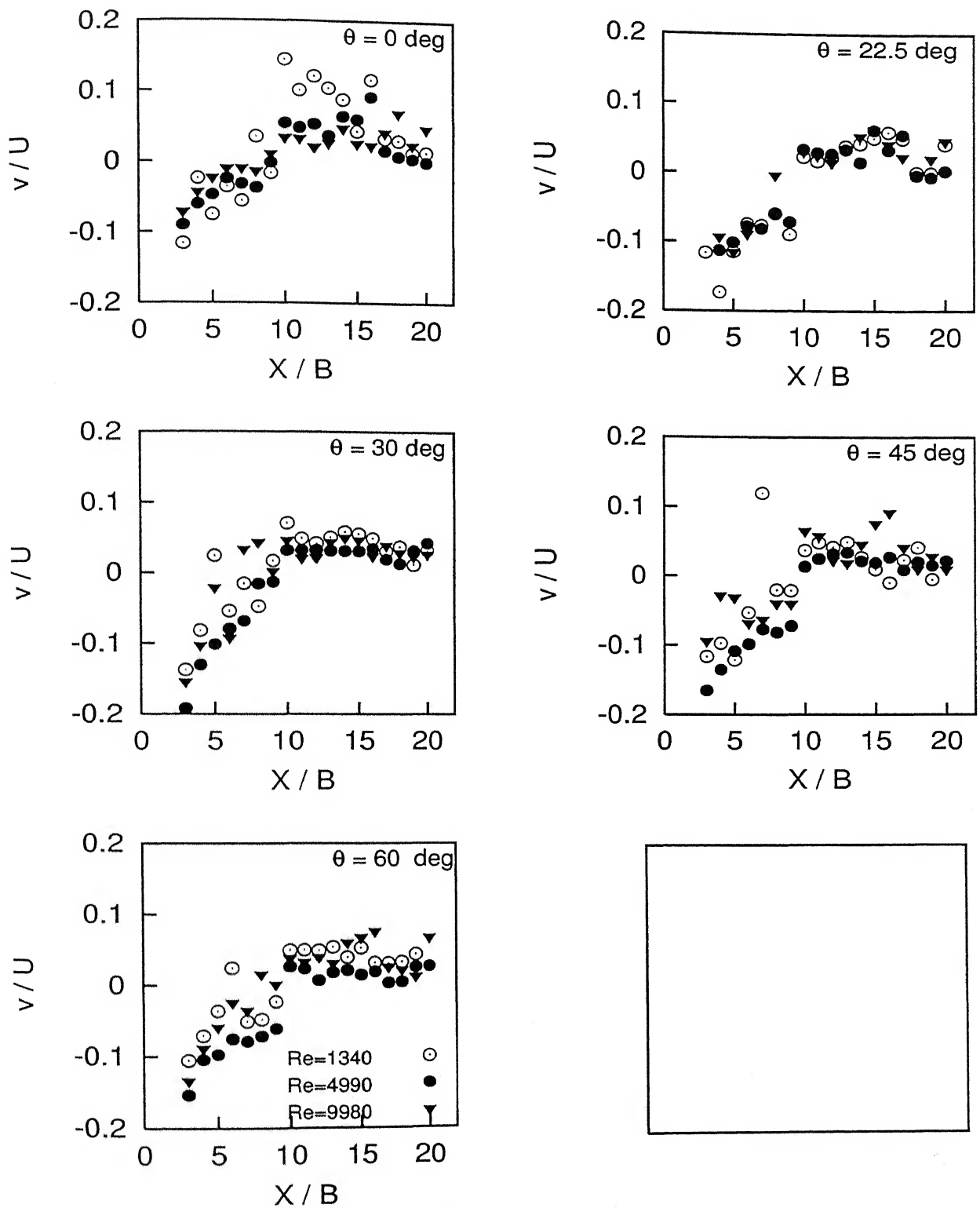
Figure 4.6: Center-line recovery of the time-averaged transverse component of velocity.
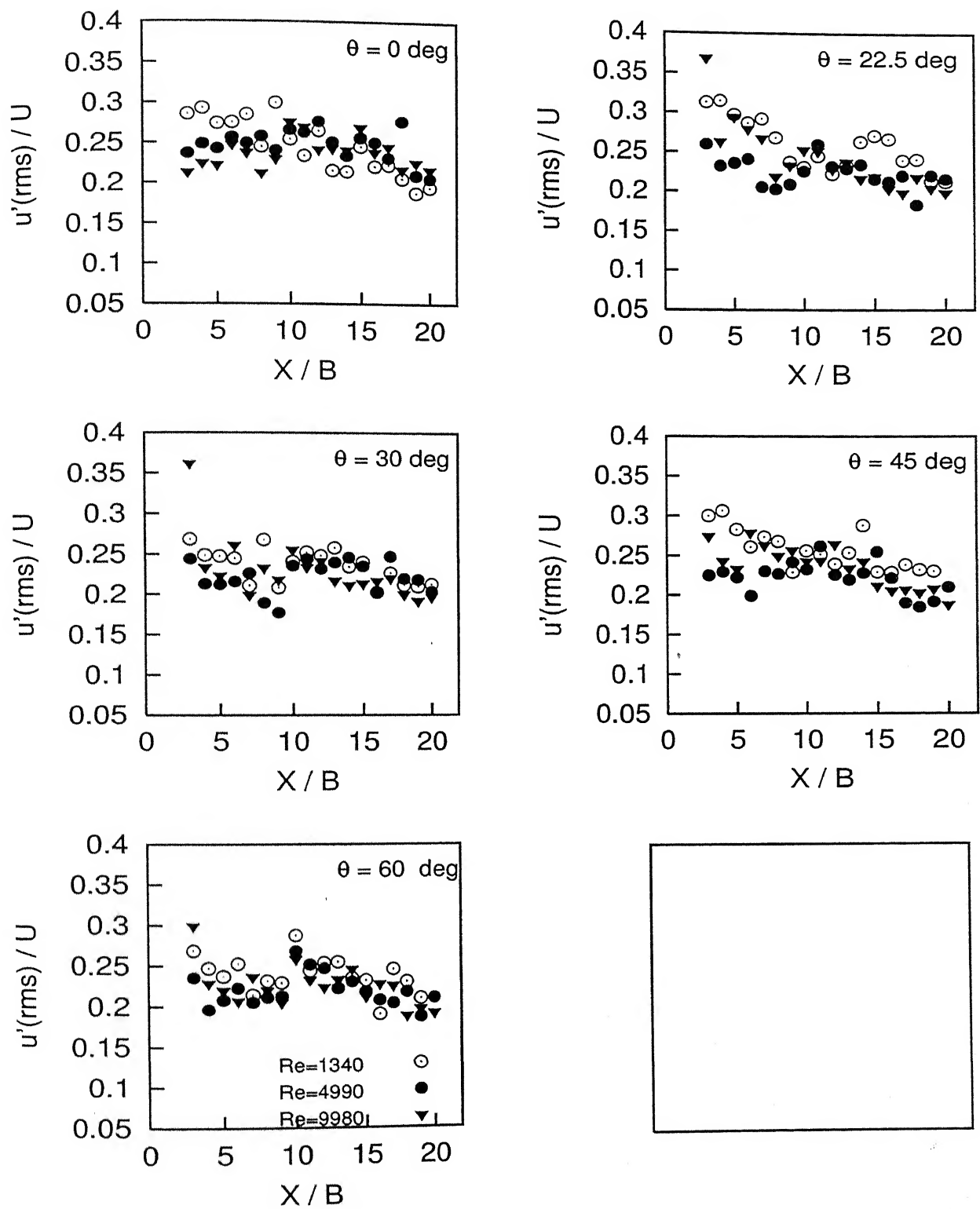
Figure 4.7: Center-line recovery of the RMS stream-wise component of velocity fluctuation.
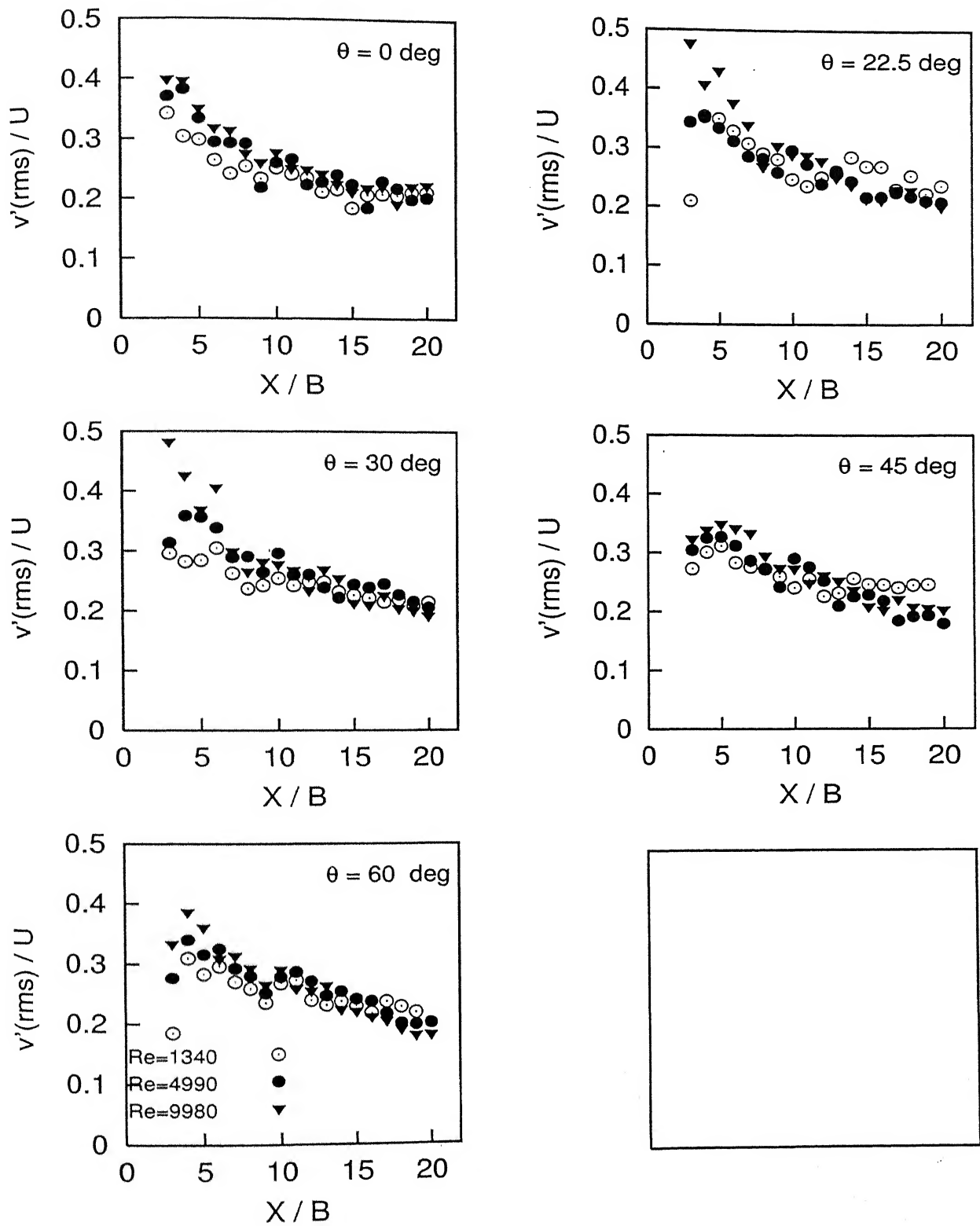
Figure 4.8: Center-line recovery of the RMS transverse component of velocity fluctuation.
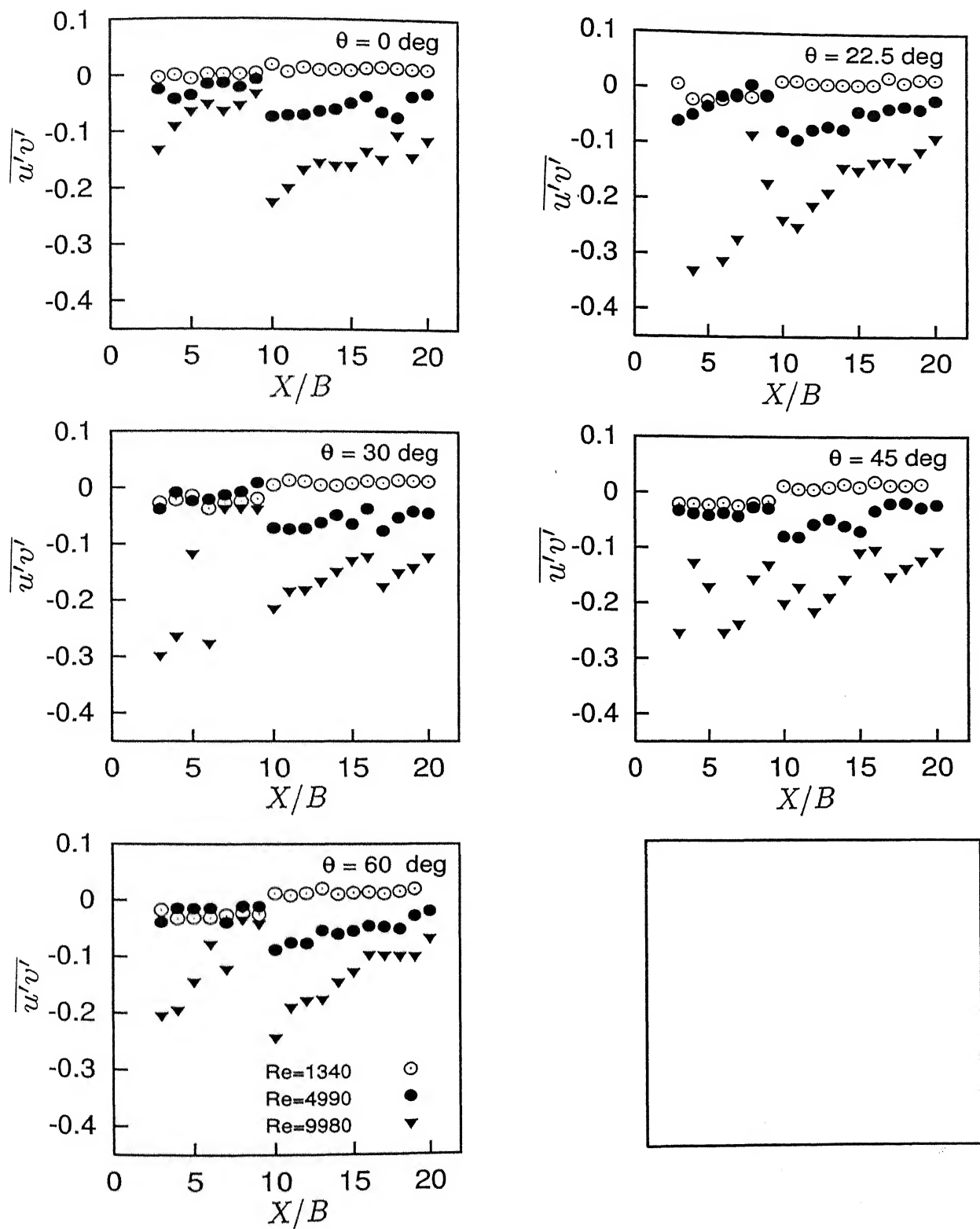
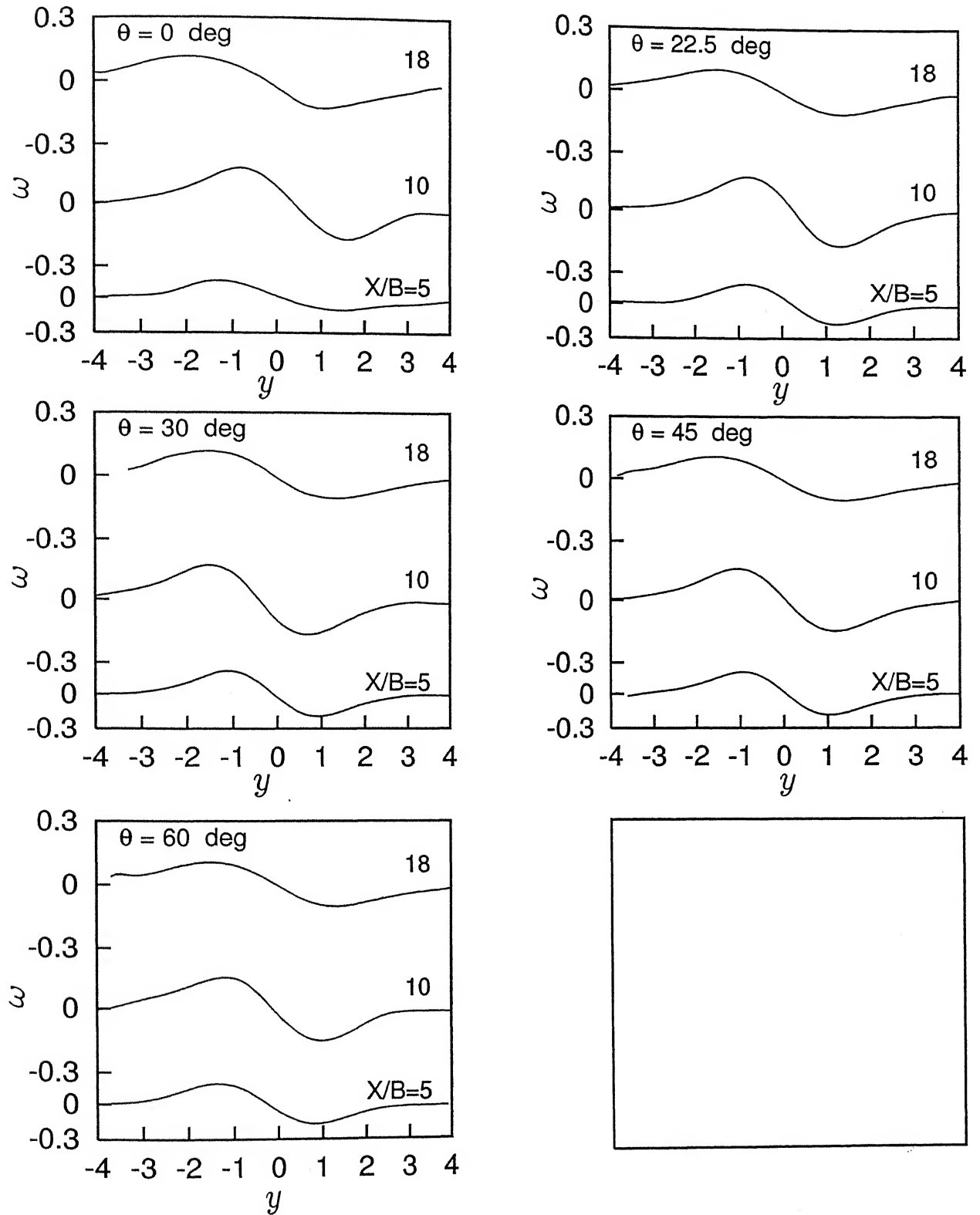Figure 4.9: Center-line recovery of the time-averaged cross-correlation of the velocity fluctuations.
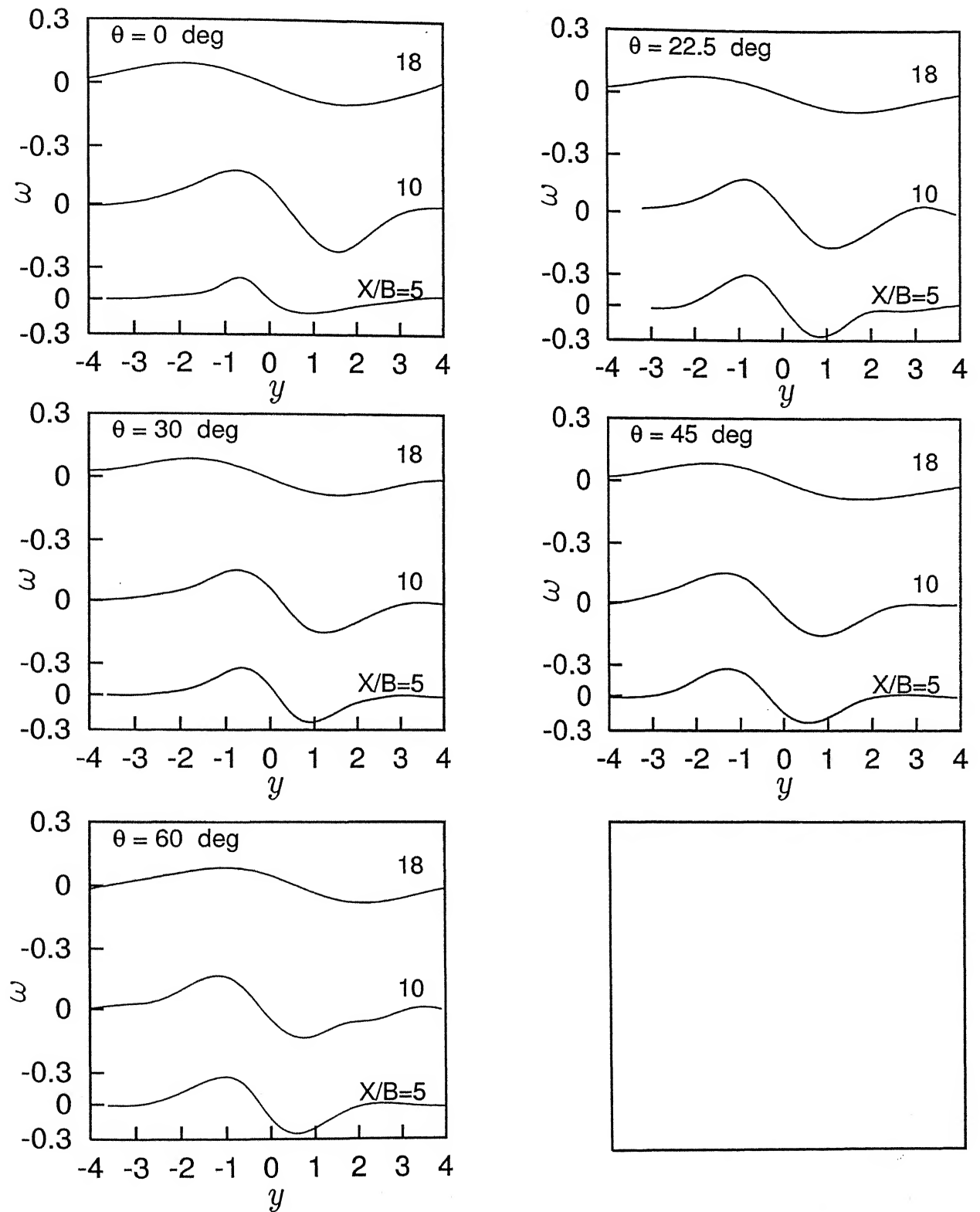
Figure 4.10: Time-averaged vorticity profiles as a function of the orientation of the cylinder; Re=1340.
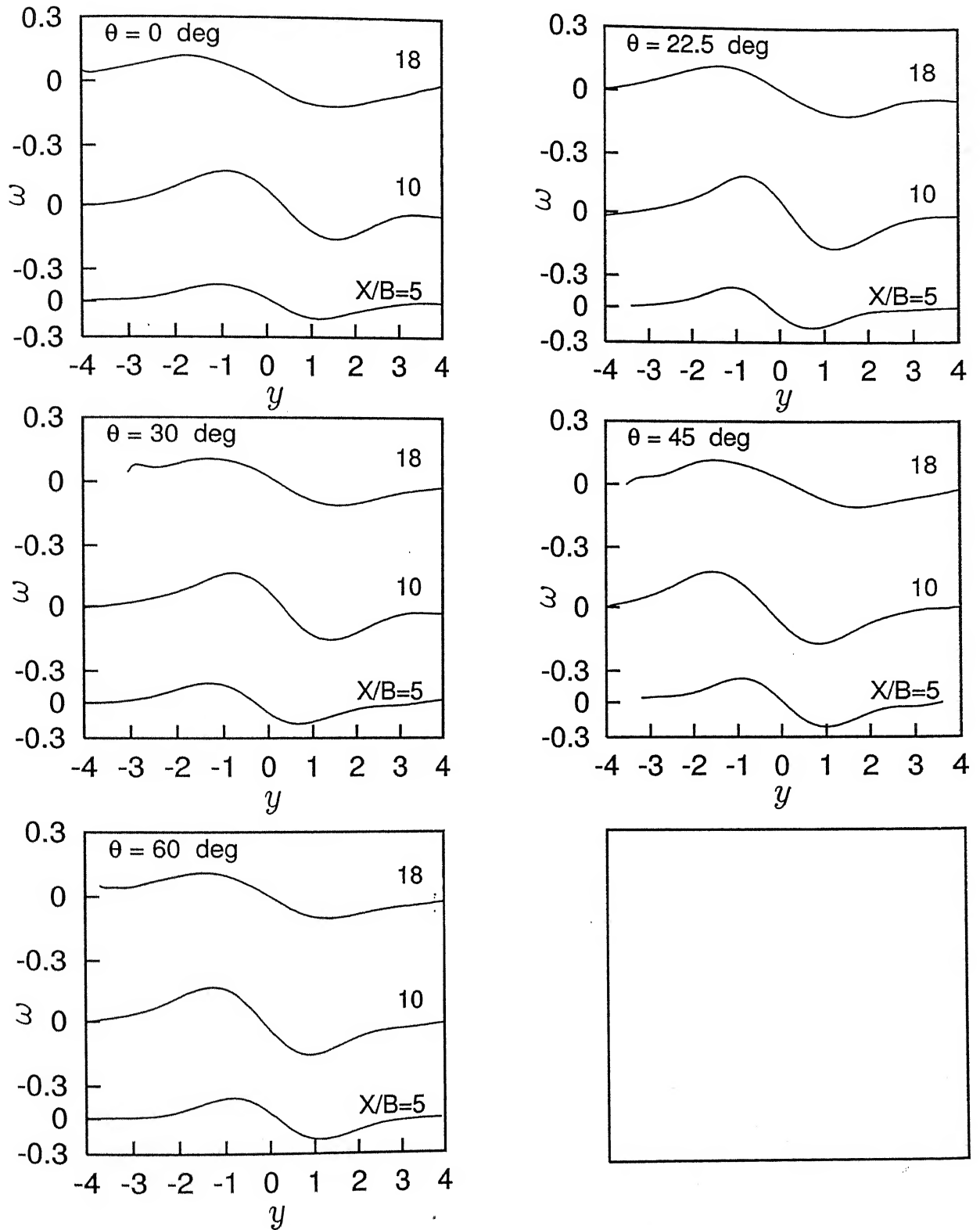
Figure 4.11: Time-averaged vorticity profiles as a function of the orientation of the cylinder; Re=4990.

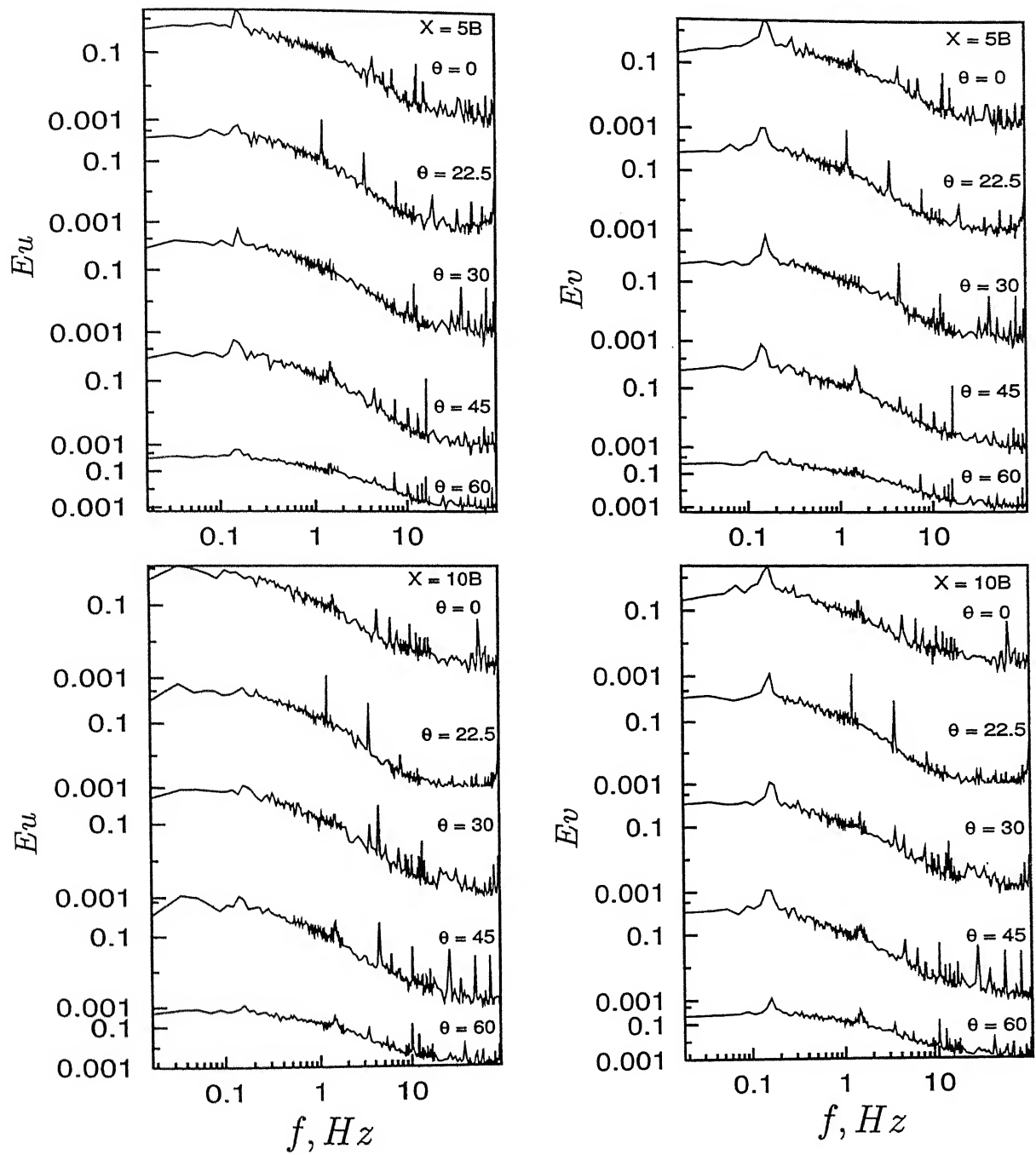Figure 4.12: Time-averaged vorticity profiles as a function of the orientation of the cylinder; Re=9980.

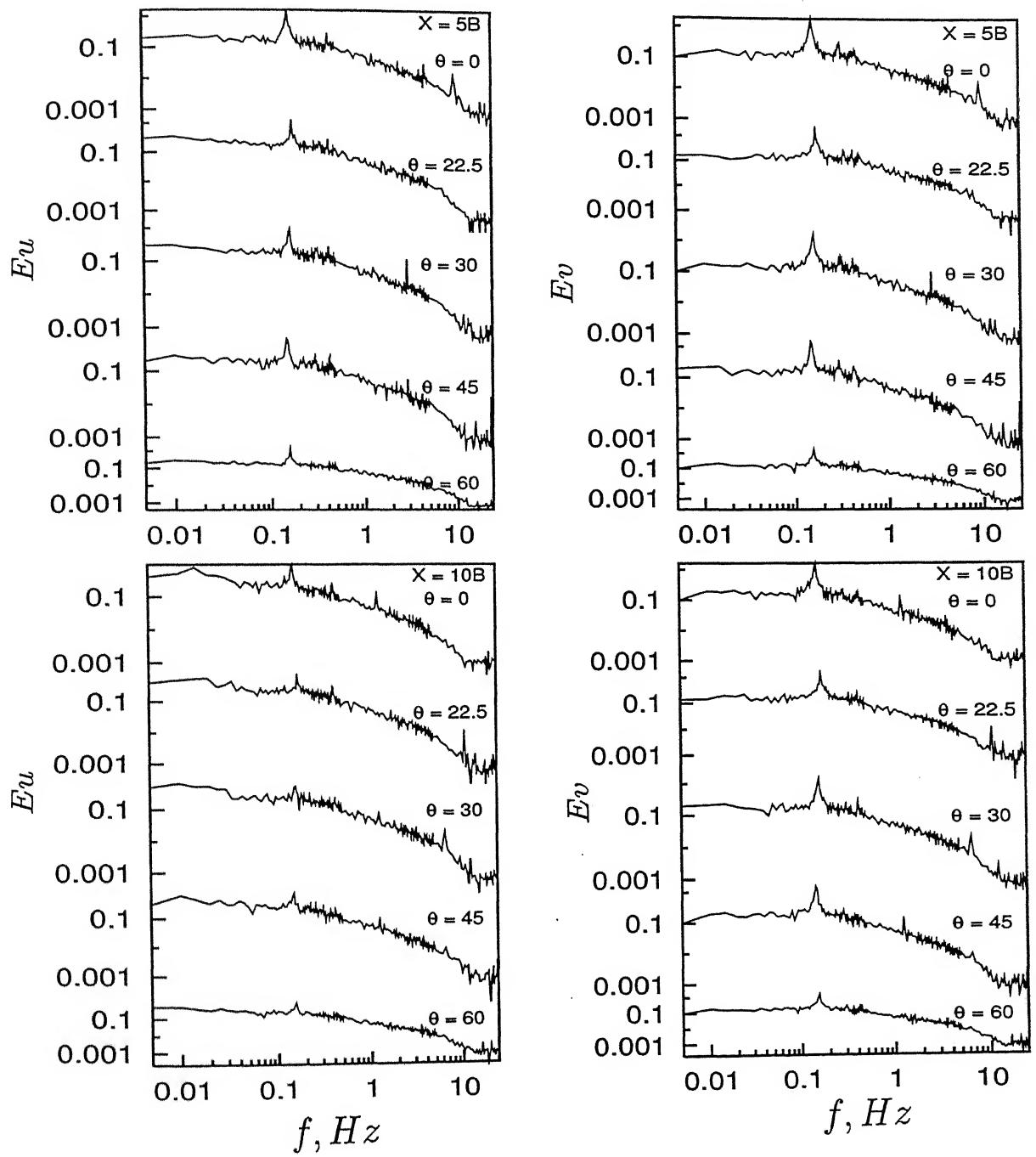Figure 4.13: Power spectra of the u and v components of velocity at X/B=5, 10; Re=1340.

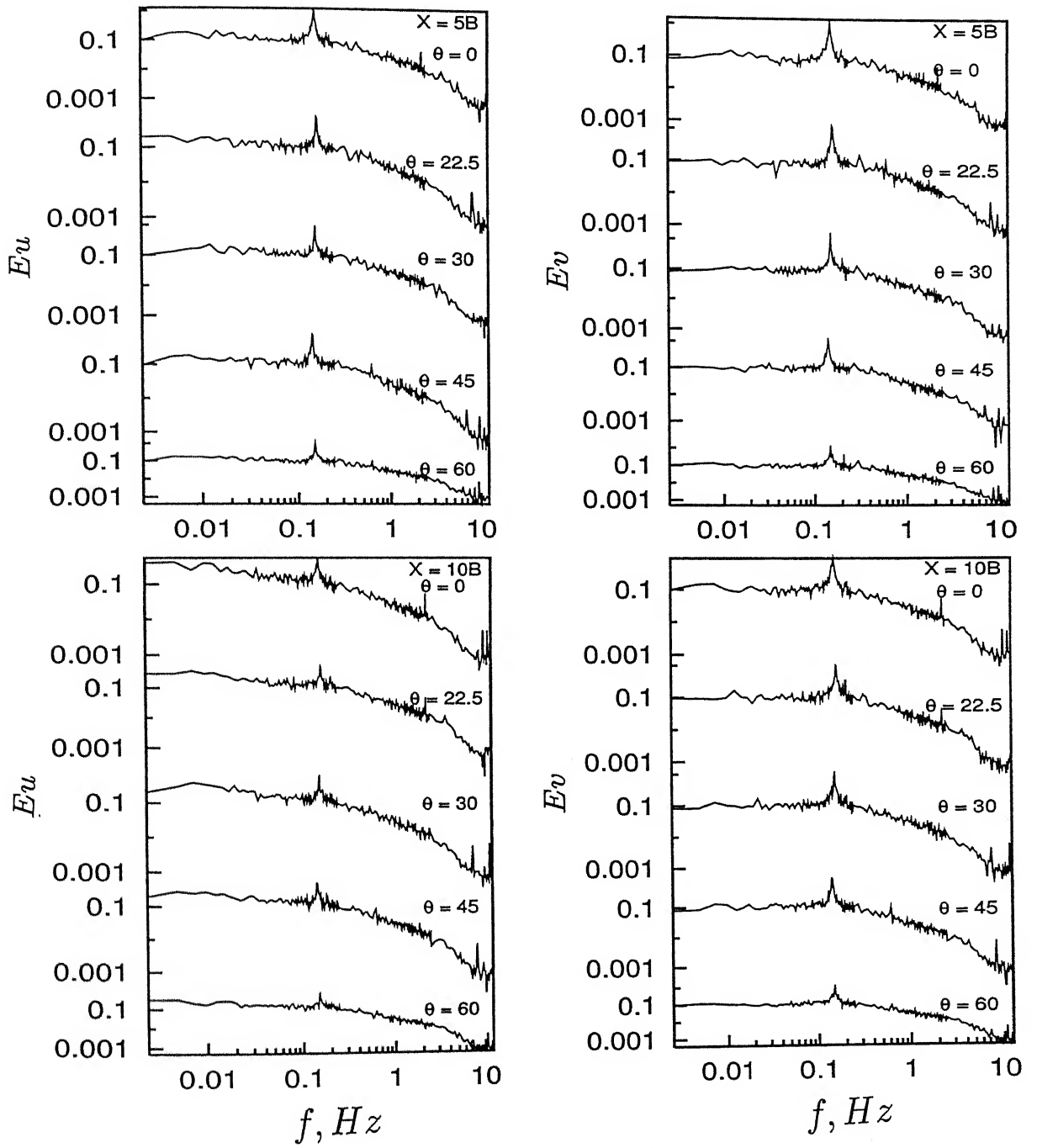Figure 4.14: Power spectra of the u and v components of velocity at X/B=5, 10; Re=4990.

Figure 4.15: Power spectra of the u and v components of velocity at X/B=5,10; Re=9980.
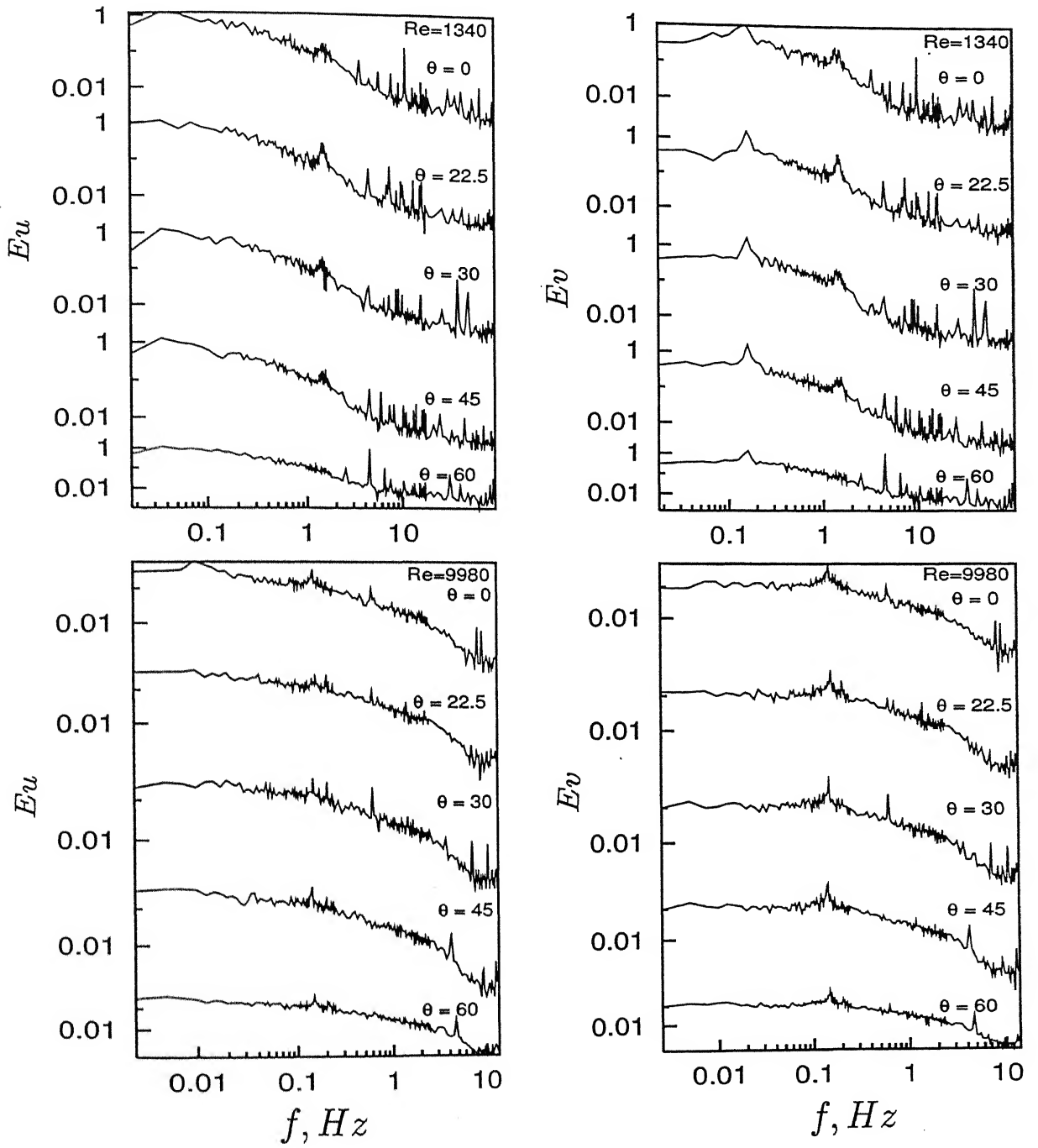
Figure 4.16: Power spectra of the u and v components of velocity at $x = 18$ location, for Re=1340 and Re=9980.
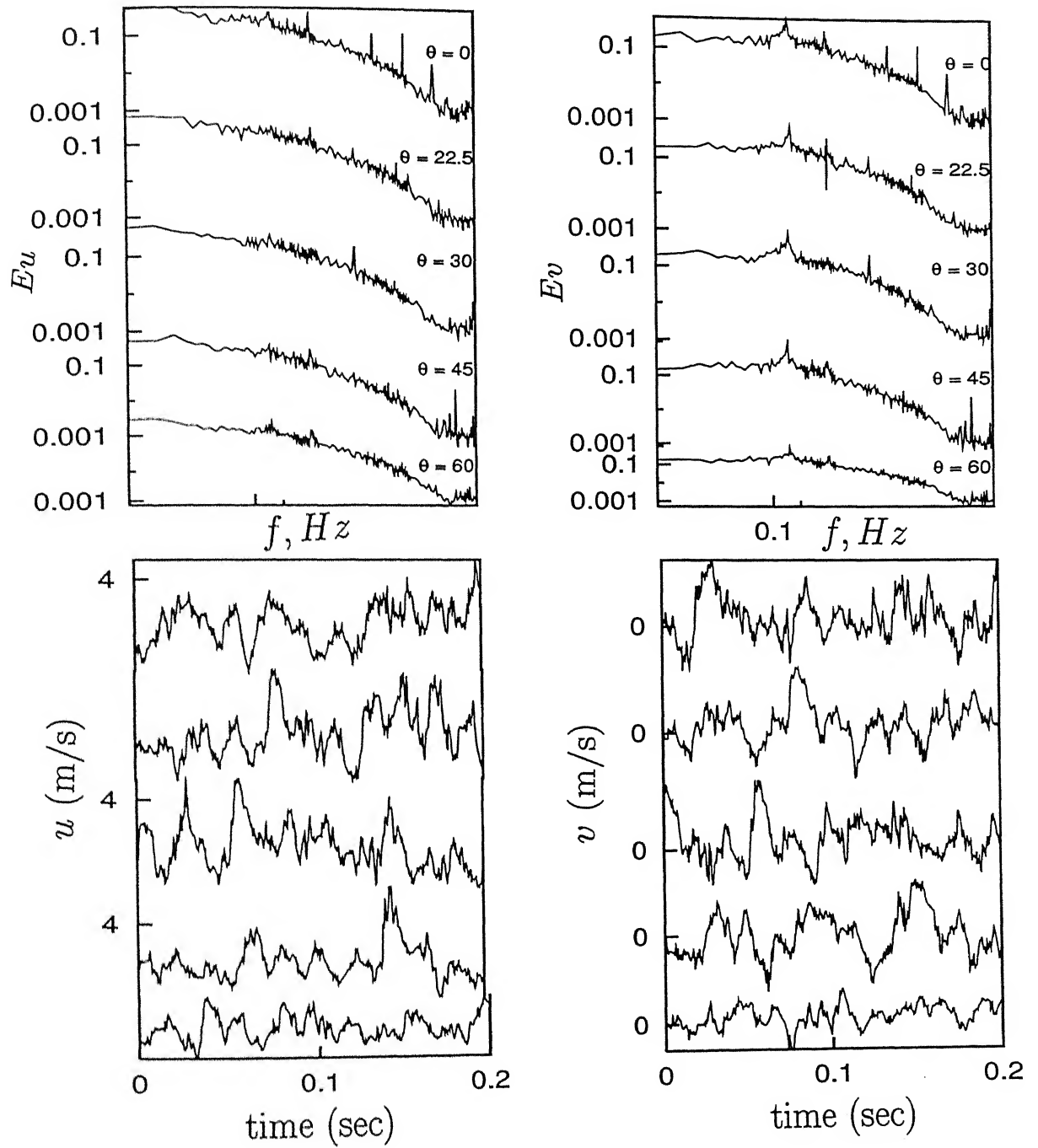
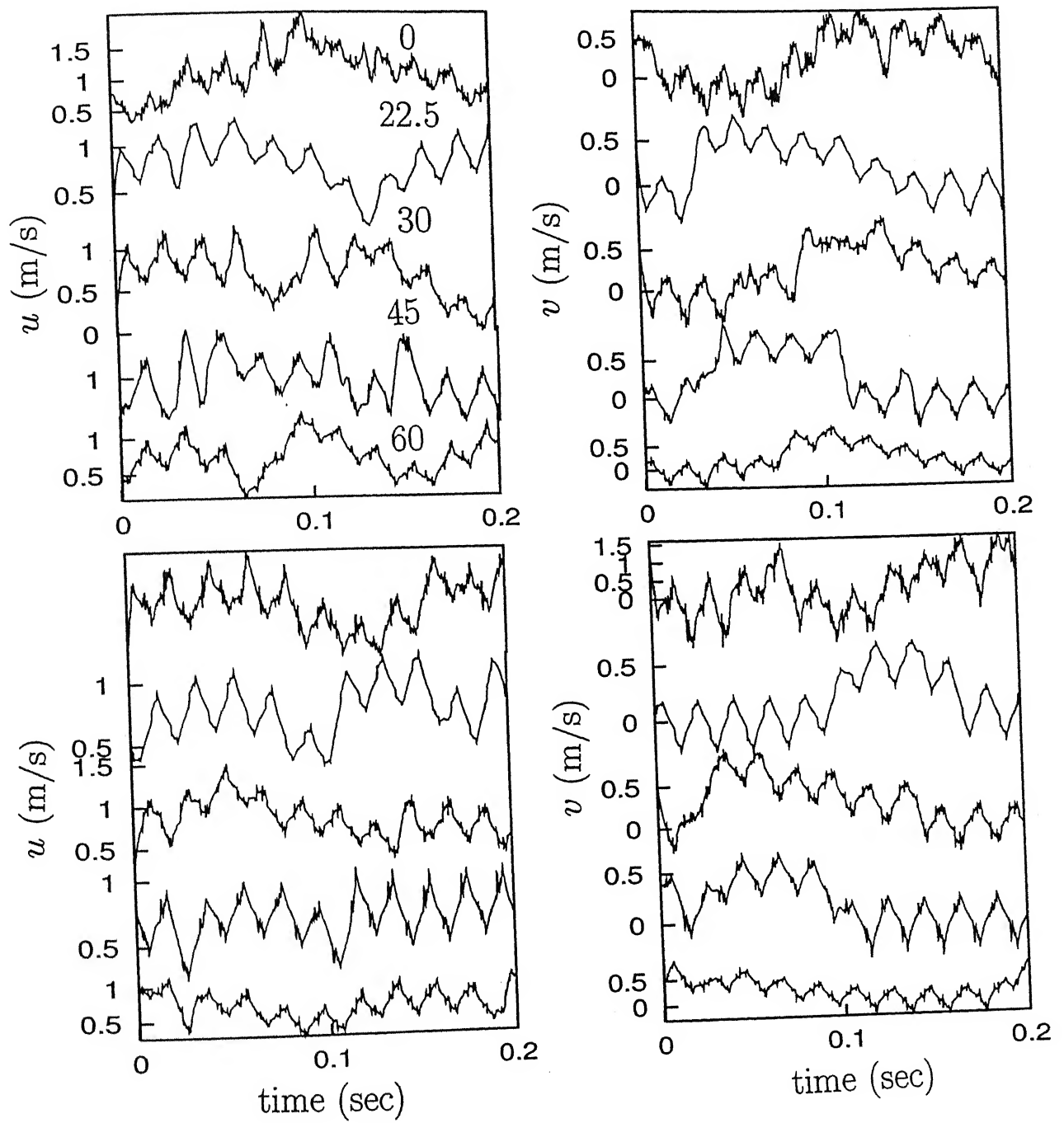Figure 4.17: Power spectra and time traces of u and v components of velocity at $x = 18$ location, for Re=4990.

Figure 4.18: Time traces of the u and v components of velocity at X/B=5, 10; Re=1340.
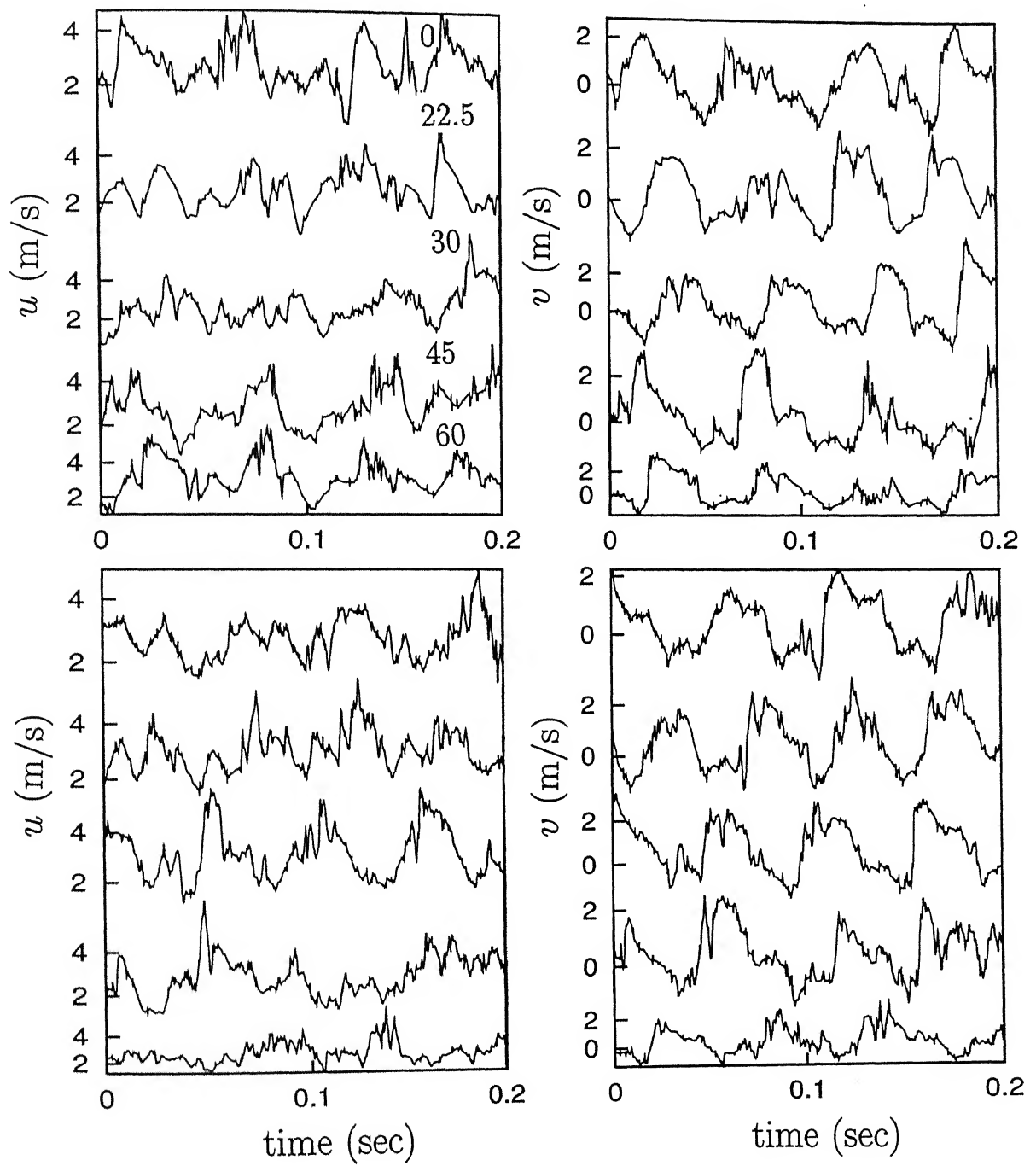
Figure 4.19: Time traces of the u and v components of velocity at $X/B{=}5$, 10; Re=4990.

Table 1: Comparison of the drag coefficients for a square cylinder at zero angle of incidence.

Authors	C_D	Reynolds number
Norberg (1993)	2.15	13,000
Knisely (1990)	2.00	500
Igarashi (1987)	2.20	5000
Nakaguchi *et al.* (1968)	2.10	40,000
Bearman and Trueman (1972)	2.00	13,000
Courchense and Laneville (1979)	2.40	1000
Present	2.207	9980

Table 2: Comparison of Strouhal numbers for a square cylinder at zero angle of incidence.

Authors	Strouhal number	Reynolds number
Kelkar and Patankar (1993)	0.122	1000
Norberg (1993)	0.132	1000
Franke *et al.* (1990)	0.130	1000
Okajima (1982)	0.125	1000
Okajima *et al.* (1990)	0.125	1000
Davis and Moore (1982)	0.142	1000
Durao *et al.* (1988)	0.138	14,000
Lyn *et al.* (1995)	0.132	21,400
Present	0.141	1340
Present	0.143	9980

Table 3: Comparison of drag coefficients of a square cylinder as a function of the angle of incidence with Norberg (1993).

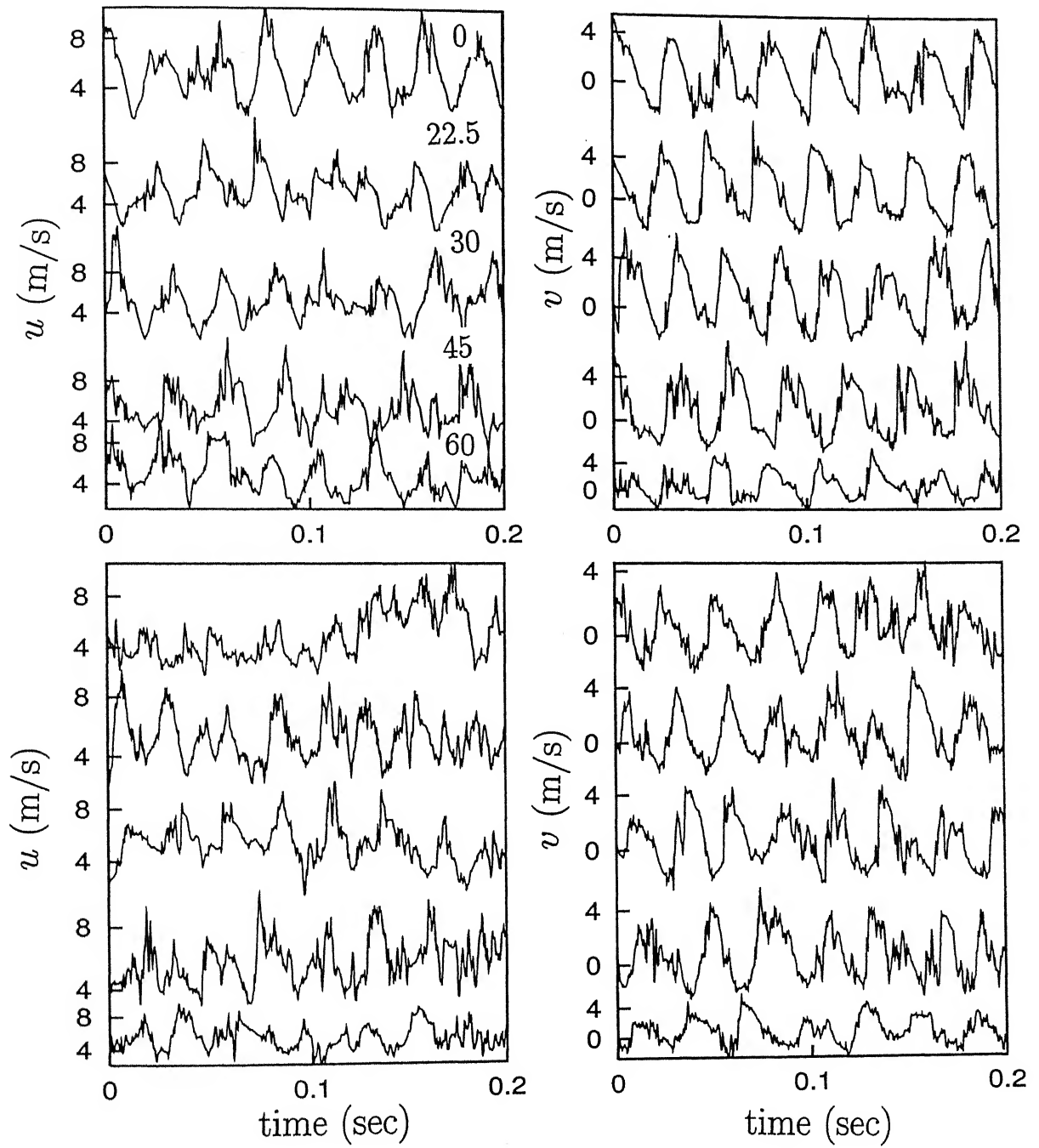| θ	Re=4990		Re=9980	
	Present	Reference	Present	Reference
0	2.49	2.15	2.21	2.20
22.5	1.53	1.54	1.61	1.54
30.0	1.65	1.60	1.62	1.60
45.0	1.43	1.60	1.58	1.60
60.0	1.65	1.58	1.64	1.58
67.5	1.53	1.54	1.61	1.54

Figure 4.20: Time traces of the u and v components of velocity at X/B=5, 10; Re=9980.

Table 4: Comparison of Strouhal numbers of a square cylinder as a function of the angle of incidence with Norberg (1993).

θ	Re=1340		Re=4990		Re=9980	
	Present	Reference	Present	Reference	Present	Reference
0	0.141	0.132	0.143	0.132	0.143	0.130
22.5	0.194	0.182	0.198	0.175	0.193	0.172
30.0	0.194	0.175	0.195	0.172	0.190	0.170
45.0	0.192	0.178	0.193	0.170	0.190	0.170
60.0	0.191	0.178	0.193	0.178	0.189	0.180
67.5	0.189	0.155	0.200	0.150	0.192	0.160

Table 5: Variation of the drag coefficient with orientation of the square cylinder at various Reynolds numbers.

θ	Re $= 1340$	Re $= 4990$	Re $= 9980$	A_c, %
0	2.270	2.490	2.207	0
22.5	1.580	1.537	1.693	30.6
30	1.604	1.651	1.617	36.0
45	1.375	1.435	1.580	41.4
60	1.708	1.643	1.642	36.0

Table 6: Variation of Strouhal number with orientation of the square cylinder at various Reynolds numbers.

Re=1340 $X = 5B$ $X = 10B$

θ	Su	Sv	Su	Sv
0	0.141	0.141	0.143	0.143
22.5	0.194	0.191	0.195	0.185
30	0.194	0.186	0.186	0.189
45	0.192	0.192	0.199	0.192
60	0.191	0.195	0.195	0.186

Re=4490 $X = 5B$ $X = 10B$

θ	Su	Sv	Su	Sv
0	0.143	0.143	0.140	0.141
22.5	0.198	0.198	0.197	0.198
30	0.194	0.186	0.186	0.189
45	0.193	0.192	0.192	0.191
60	0.193	0.194	0.193	0.193

Re=9980 $X = 5B$ $X = 10B$

θ	Su	Sv	Su	Sv
0	0.143	0.143	0.142	0.142
22.5	0.193	0.192	0.192	0.192
30	0.190	0.191	0.190	0.190
45	0.190	0.190	0.188	0.189
60	0.189	0.189	0.188	0.188

4.2 Heated Cylinder

The wake behind the constant temperature circular cylinder is studied by the laser Schlieren technique. The complete schlieren image is captured by the CCD camera and the pointwise intensity and its fluctuations are captured by the photodiode.

The results of this work is presented in the following sequence: (1) average Nusselt number (2) steady state wake behavior and (3) temporal wake behavior (4) power spectrum.

4.2.1 Average Nusselt Number

Table 7 summarizes the quantities measured for calculation of heat transfer rate under flow condition. Table 8 gives the measurements of non dimensional number frequently used for characterize the flow. Table 9 gives comparison of present experimental data with empirical relation of Nusselt number. It should be mentioned that the end-loss from the cylinder was neglected in the calculation of the experimental Nusselt number which may be responsible for some discrepancy. Hence, it may be concluded that the present experimental Nusselt number results compares well with that of the earlier correlations indicating the reliability of the instrumentation used in this work.

Table 7: Data related to heat transfer rate calculation.

Temp.of cylinder above atm. $(T_s - T_\infty)$ $in(^\circ C)$	Thermal conductivity (K)in (W/mK)	Kinematic viscosity(ν) in(m^2/sec) $\times 10^6$	Voltage(V) in (Volts)	Current(I) in (amps)	Time for which heater is on (t_{on}) in secs
18.2	0.0270	16.714	5.2	2.0	174.10
24.7	0.0273	17.044	5.2	2.0	269.19
32.3	0.0275	17.430	6.0	2.5	246.59
39.5	0.0278	17.790	6.0	2.5	329.89
45.6	0.0280	18.100	6.9	3.0	249.25
51.3	0.0283	18.390	6.9	3.0	310.37
55.5	0.0284	18.600	7.3	3.5	205.07
59.8	0.0289	18.820	7.3	3.5	319.09
62.5	0.0287	18.960	7.3	3.5	320.92
65.7	0.0288	19.120	8.0	4.0	295.84
69.4	0.0289	19.310	8.0	4.0	302.44
72.6	0.0291	19.478	8.0	4.0	316.26
75.3	0.0292	19.610	8.5	4.5	298.83
79.5	0.0293	19.820	8.5	4.5	361.40
86.5	0.0296	20.180	8.5	4.5	366.57

Table 8: Data reduction for heat transfer rate calculation.

Fraction of time heater is on	power supplied by heater in Watts	Radiation correction (Q_{rad}) in Watts	Heat transfer coefficients $(h)W/m^2K$	Reynolds number (Re)	Prandtl number (Pr)	Grashoff number (Gr)	$Gr./Re^2a$
0.435	4.524	0.725	27.68	107.7	0.7035	444.7	0.0380
0.673	6.999	1.015	32.13	105.6	0.7050	574.0	0.0514
0.616	9.240	1.378	32.28	103.3	0.7042	709.6	0.0660
0.825	12.375	1.745	35.69	101.2	0.7034	823.6	0.0800
0.623	12.896	2.075	31.47	99.45	0.7027	910.0	0.0920
0.776	16.060	2.399	35.31	97.87	0.7021	983.0	0.1020
0.513	13.110	2.649	24.99	96.77	0.7016	1033.0	0.1103
0.799	20.410	2.914	38.80	95.64	0.7012	1080.0	0.1180
0.802	20.490	3.085	36.93	94.94	0.7009	1107.6	0.1228
0.740	23.67	3.292	41.13	94.14	0.7005	1139.5	0.1285
0.756	24.19	3.539	39.46	93.21	0.7001	1173.6	0.1351
0.791	25.31	3.759	39.37	92.45	0.6997	1202.0	0.1406
0.747	28.57	3.949	43.36	91.79	0.6994	1224.0	0.1453
0.903	34.56	4.252	50.56	90.82	0.6990	1257.0	0.1524
0.916	35.04	4.781	46.39	89.19	0.6980	1306.0	0.1642

Table 9: Heat Transfer rates at different Grashoff numbers.

Grashoff Number	Nusselt Number	
	Present Study	Correlation
444.7	6.15	5.48
574.0	7.07	5.45
709.6	7.03	5.41
823.6	7.70	5.37
910.0	6.73	5.34
983.0	7.5	5.31
1033.0	5.28	5.29
1080.0	8.15	5.27
1107.6	7.73	5.25
1139.5	8.57	5.24
1173.6	8.18	5.22
1202.0	8.13	5.20
1224.0	8.92	5.19

4.2.2 Steady State Wake Behavior

Steady wake visualisation results have been presented in this section. Experiments were performed in the test cell described earlier in the paper and Schlieren
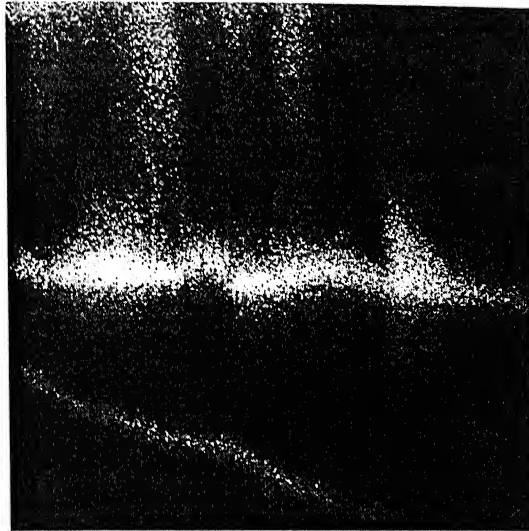
(a) Warm hand
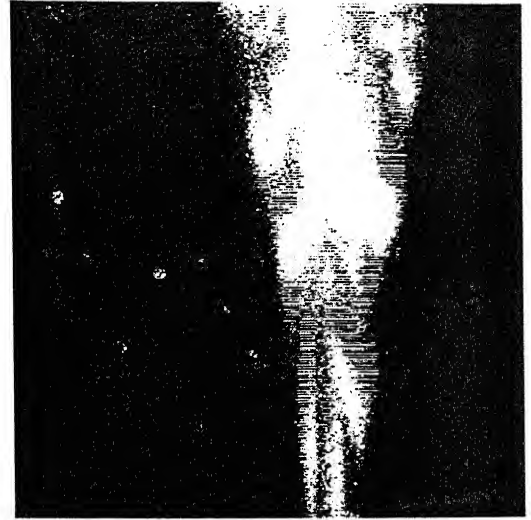
(b) Candle flame

Figure 4.21: Buoyancy driven flow patterns recorded using the experimental set-up present in the laboratory.
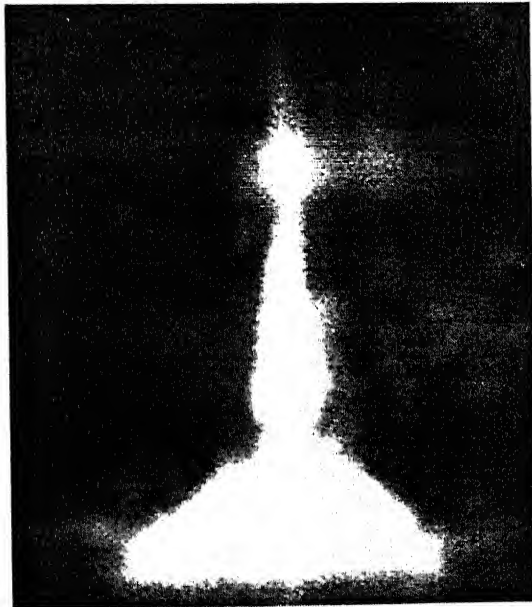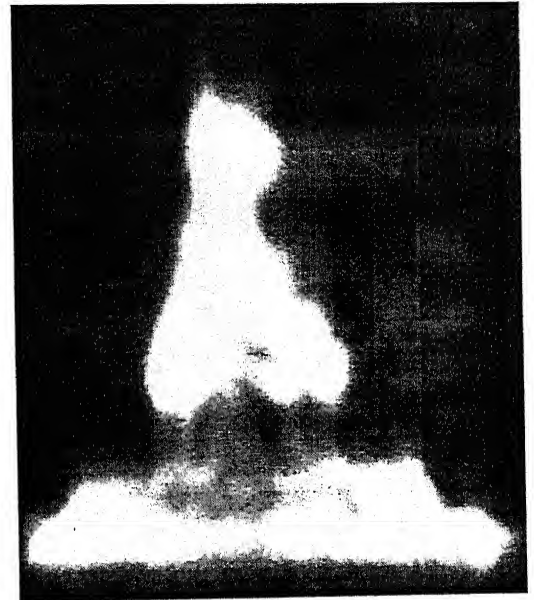

(a) Re=0.0

(b) Re=100.0

Figure 4.22: Wake above the heated horizontal cylinder for $Gr = 1300$.

technique was applied to visualize the flow. Figure 4.21 shows some qualitative pictures of free convection. Figure 4.21(a) shows the convection arising from a human hand. Here the density changes result from the changes in temperature.
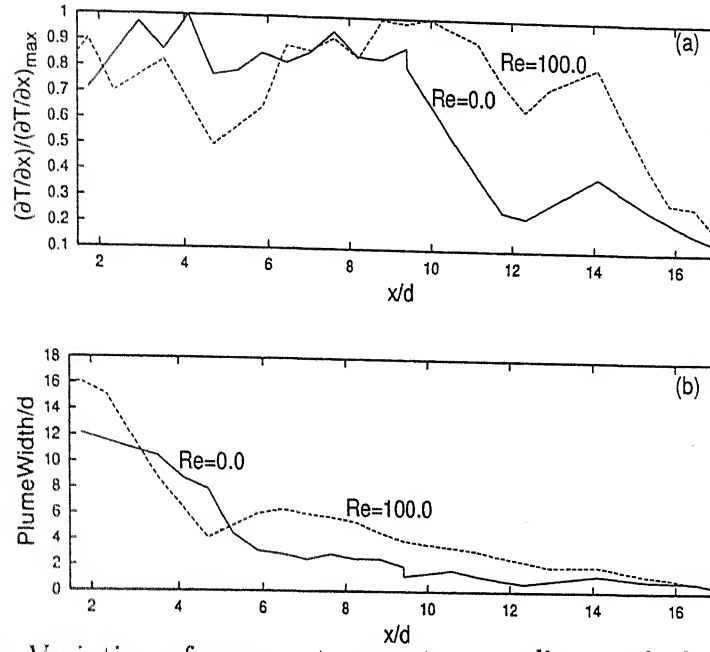
Figure 4.23: Variation of average temperature gradient and plume width with respect to the flow direction, Gr=1300.

These results can be used in gaining a better understanding of the interface between the air and the human body. Such issues can be used to study thermal comfort, protective clothing, the airborne spread of infections. Figure 4.21(b) shows the convection pattern of air above a candle flame indicating the potential of Schlieren application for combustion problems.

Figure 4.22 shows the convection pattern above the surface of a heated cylinder maintained at a temperature of around 80°C (Gr = 1300). The cylinder is kept parallel to the direction of the beam and hence gives the integrated information along the length of the cylinder. Figure 4.22(a) shows the no-flow case and Figure 4.22(b) shows the flow case at Reynolds number equal to 100.0. An appreciable difference in the two cases can be seen as far as the nature and the size of the plume is concerned, the plume width being more for Re = 100.0 case as compared to Re = 0.0 case. These differences are shown in Figure 4.23. The variation of average normalized temperature gradient with respect to the dimensionless distance (x/d) and variation of the dimensionless plume width with respect to the dimensionless distance (x/d)is shown in Figure 4.23(a) and (b) respectively. The temperature gradient at the far field region for the Re = 100 case is observed to be higher than that for Re = 0 indicating the effect of flow in stream-wise transport of energy.
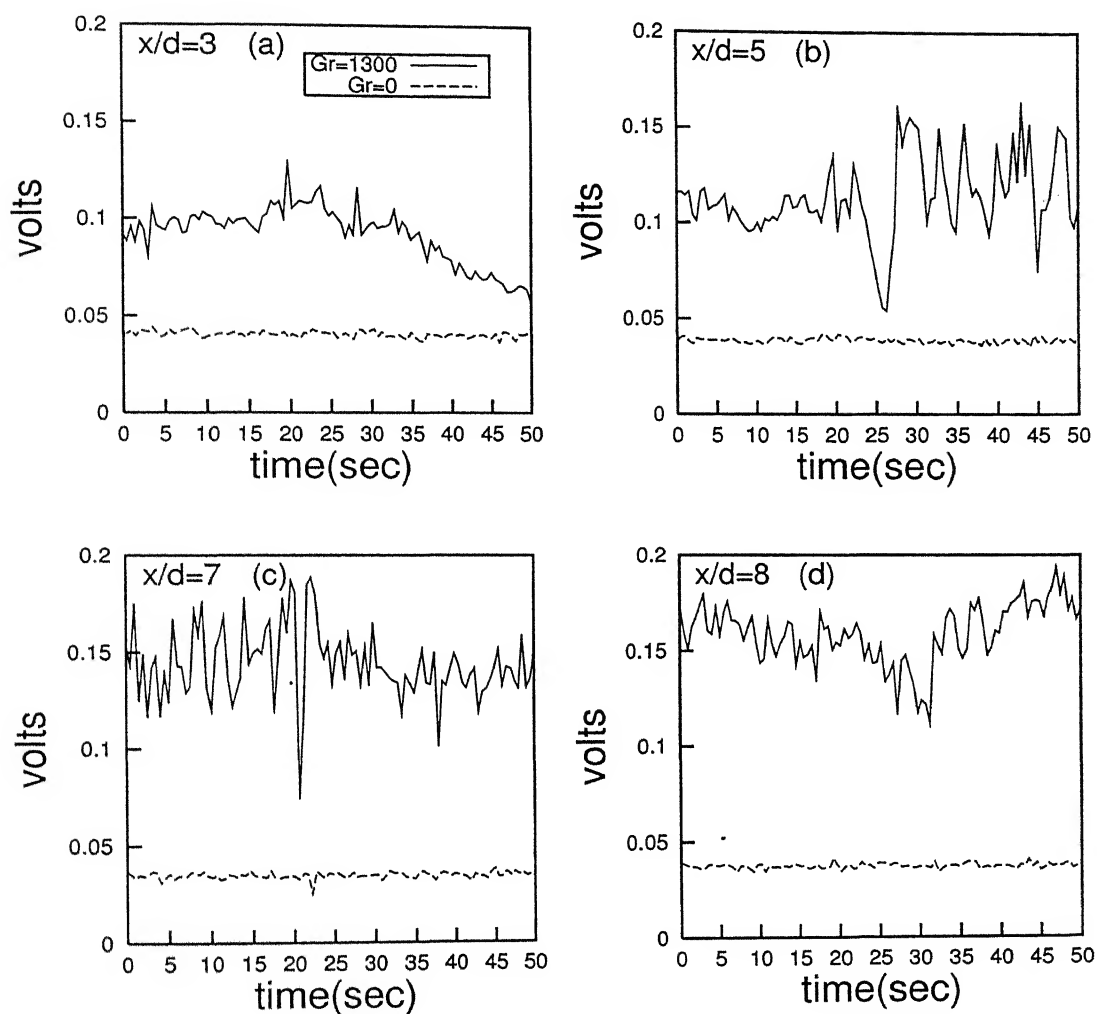
Figure 4.24: The photodiode signal at $y/d = 0.5$ for different stream-wise (x/d) locations with horizontal knife edge setting.

4.2.3 Temporal Wake Behavior

Temporal bahaviour of the wake above the heated cylinder is studied using the Schlieren signals recorded by the photodiode at different stream-wise (x/d) and cross-stream (y/d) locations. Flow was assumed to be two dimensional as the aspect ratio of the cylinder is very high (66). Reference signals in each case study were recorded before heating the cylinder and these were taken as reference values.

Figure 4.24 shows photodiode signals recorded at various downstream positions. The cylinder temperature was maintained at 80°C which corresponds to a Grashoff number, Gr = 1300. The cross-stream offset was kept at $y/d = 0.5$ and the signals were recorded along this offset position parallel to the length of the cylinder. Hence the photodiode records the integrated information in the form of intensity. Figure 4.24(a-d) show the variation and a gradual change in the signal recorded as one moves in the downstream direction in the wake region. Solid lines correspond to the cylinder temperature of 80°C and the dotted lines show the pattern of the signal when the cylinder is kept at the ambient (T=24°C) temperature. Flow is maintained at a constant speed of 0.34 m/s which corresponds to a Reynolds number, Re = 100.0. The average value of the photodiode signal is observed to be dependent on the downstream location. The nature of the fluctuation is also observed to be dependent on the downstream location. Similar variation of average temperature gradient with respect to stream-wise distance (x/d) was observed earlier from the steady state Schlieren image analysis. Figure 4.25 shows the variation in the temperature gradient in the form of photodiode signals as recorded with two settings of the knife-edge. Figure 4.25(a) shows the pattern recorded when the knife-edge was kept horizontal and Figure 4.25(b) represents the vertical knife- edge setting. Results for three values of Grashoff number are presented. The signals were recorded at a downstream offset of 5d and crosswise offset of 1.5d from the cylinder axis. As shown, the level of signal fluctuations is large in the vertical knife-edge setting as compared to the horizontal knife-edge position. This is because of the fact that the wake size is very less in the crosswise direction as compared to the downstream direction. Hence the flow meets the ambient conditions over a small distance which is equal to half the width of the wake. So the temperature drop is sudden in the crosswise direction whereas there is a gradual decrease in the temperature in the downstream direc-

tion over the full length of the wake which is more than its width. This leads to high temperature gradient in the crosswise direction which is shown in the form of large levels of fluctuations in Figure 4.25.

Figure 4.26 shows the behavior of recorded photodiode signals during transient blower operations for different offset positions both in downstream direction and in crosswise direction. Figure 4.24(a-d) shows the effect of forced convection on the buoyancy driven flow. The flow was kept on for an appreciable amount of time so that it reaches a steady state before it was turned off for a period of about 4-5 minutes. The effect of the this transient blower operation is evident in the figure. During the initial period in which the flow was kept ON, the nature of the signal reveals a steady behavior of the wake. The fluctuations are very small and the signal is almost constant. This observation shows that the air flow from the blower helps to stabilize the wake. As soon as the blower is turned Off, sudden fluctuations in the signal occur whose intensity is quite large as compared to the mean value. This is the time when the flow is totally buoyancy driven and is unsteady which can be seen by the large peaks of the signal in Figure 4.26. After this, the flow again becomes steady as soon as the blower is turned ON.

4.2.4 Power Spectra

Figure 4.27 shows the power spectrum at different streamwise locations for Grashoff number of 1300 and Reynolds number 100. The calculated vortex shedding frequency is 12 for $St = 0.2$ of circular cylinder. But, no clear peak is observed in the spectra indicating the absence of clear vortex shedding. The effect of unevenness of the cylinder surface may would have contributed to the 3-dimensionality before the separation with subsequent suppression of vortex shedding. The other possible reason is the fluctuation in the cylinder temperature i.e. the cylinder surface temperature fluctuation of 2° C was observed. This may would have affected the instability at separation and also the vortex shedding mechanism. Figure 4.28 shows the power spectra for both horizontal and vertical knife edge setting. No clear dominant peak is observed in either knife edge setting. But, the amplitude of the power spectra for the horizontal knife edge setting is seen to be higher than that of the vertical knife edge setting.
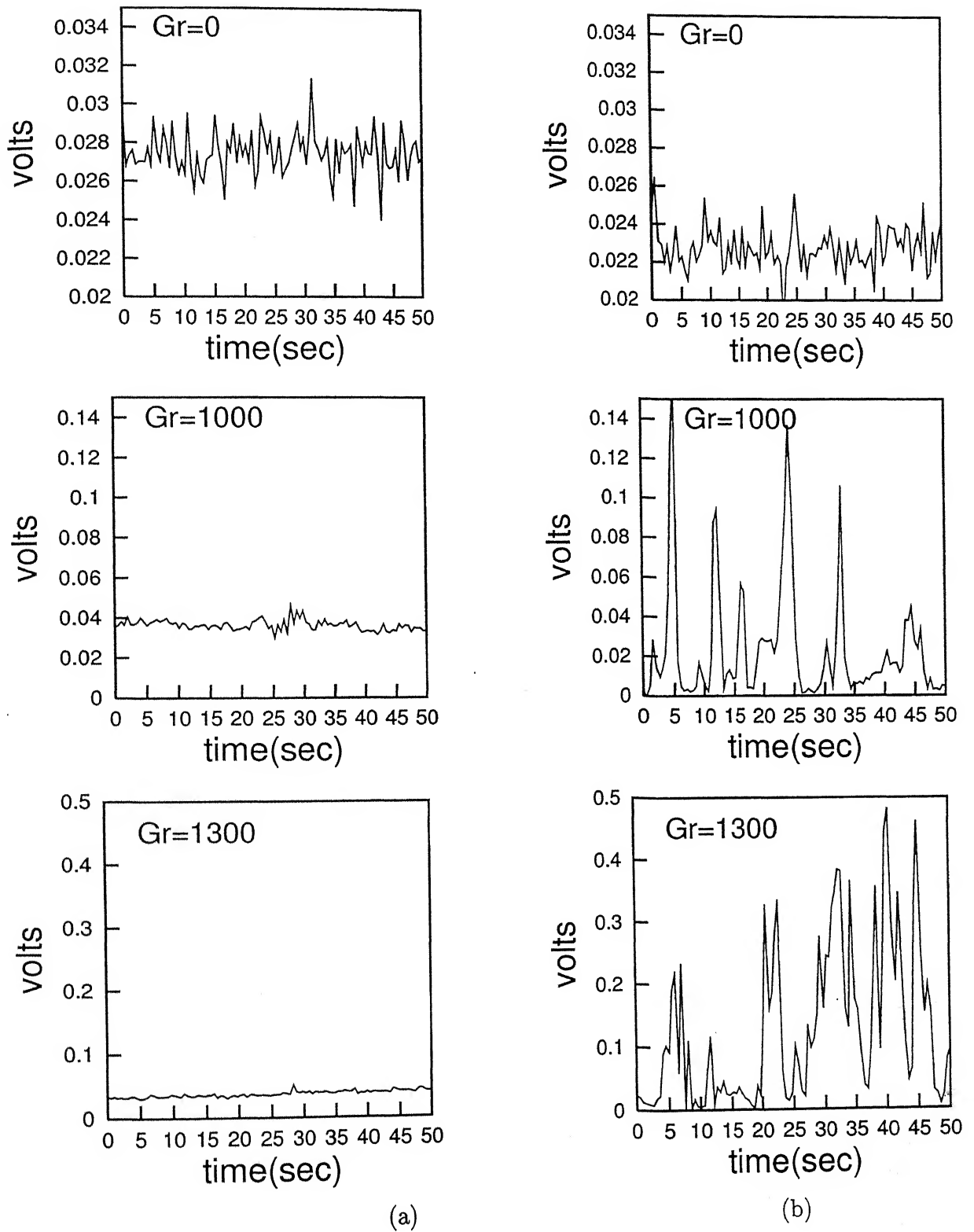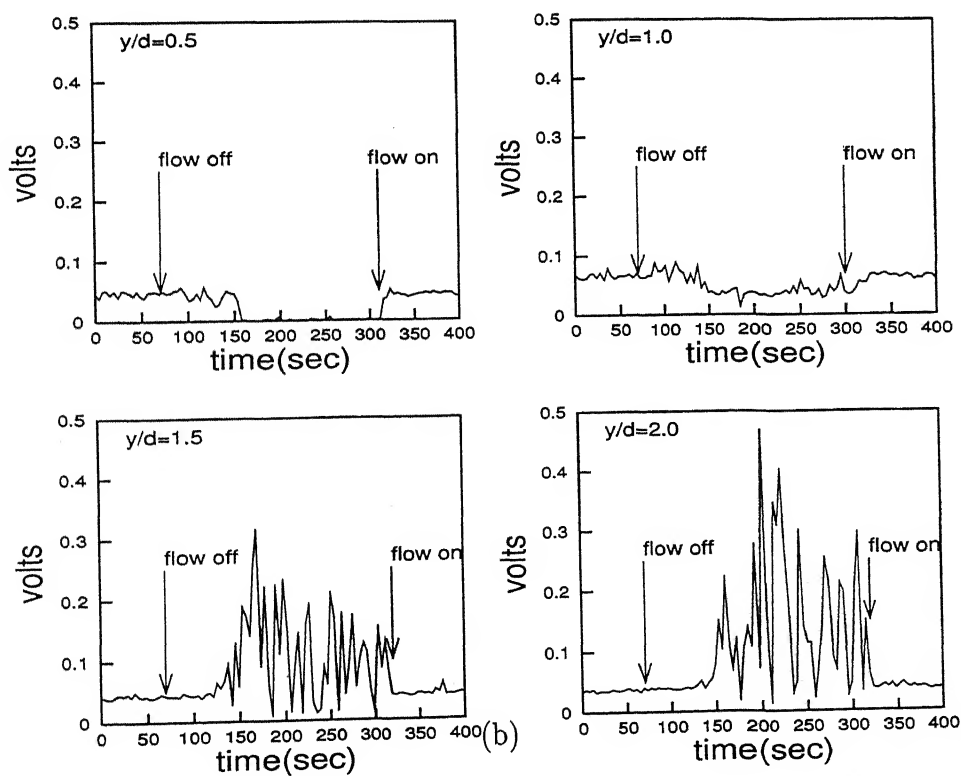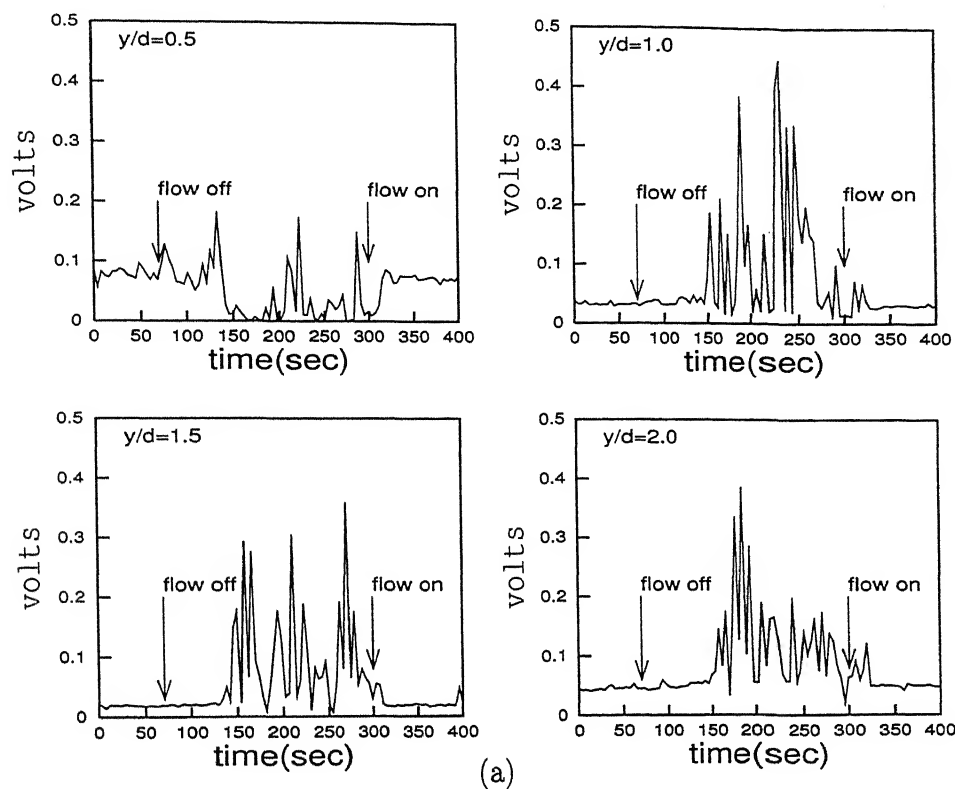
Figure 4.25: Photo diode signal for two knife edge settings, (a) Horizontal, (b) Vertical at $y/d = 1.5$ and $x/d = 5$.
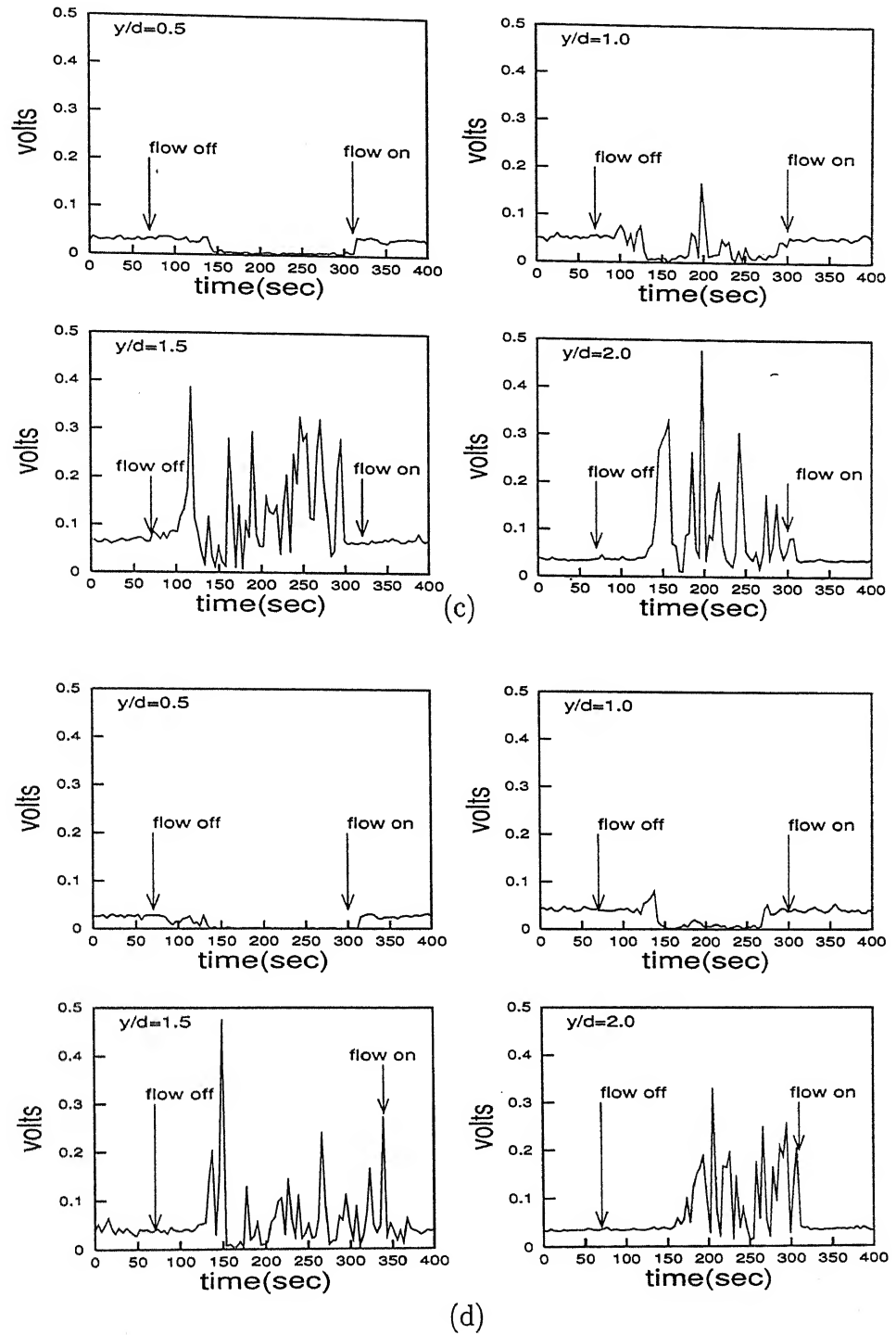
(a)

(b)

Figure 4.26: Photodiode signal for different offset (y/d) locations during the transient blower operation, (a) $x/d = 3$, (b) $x/d = 5$, (c) $x/d = 7$, (d) $x/d = 9$.
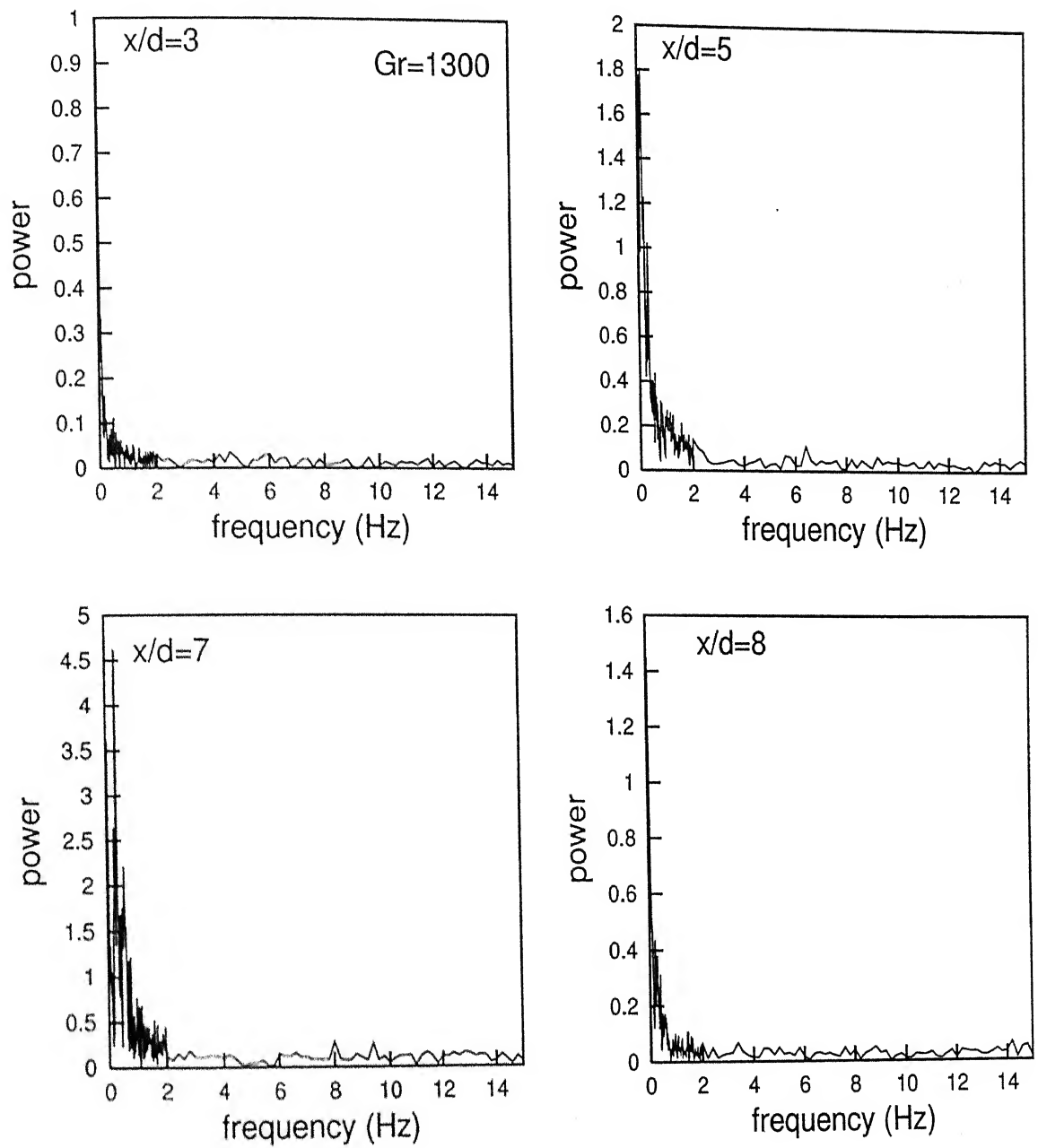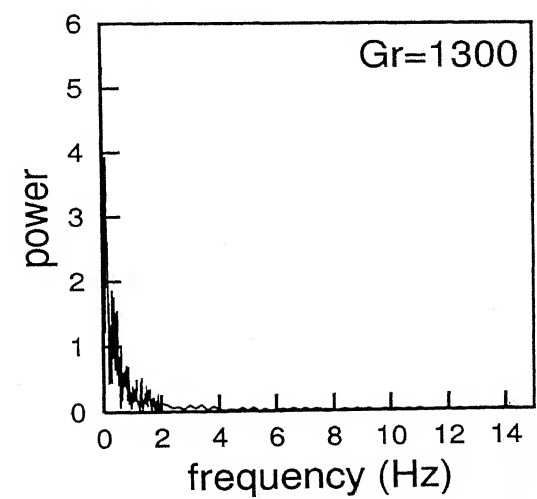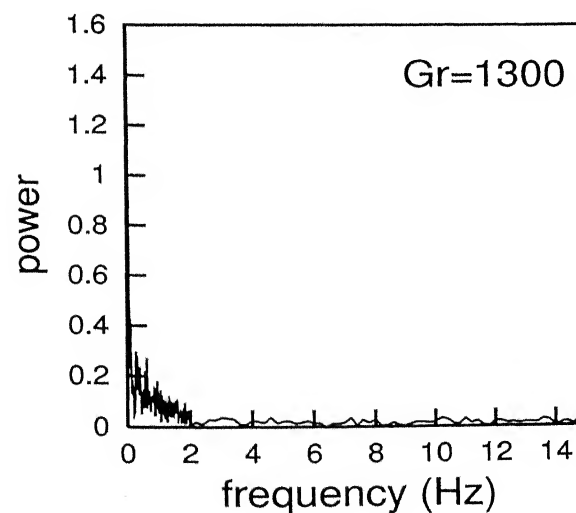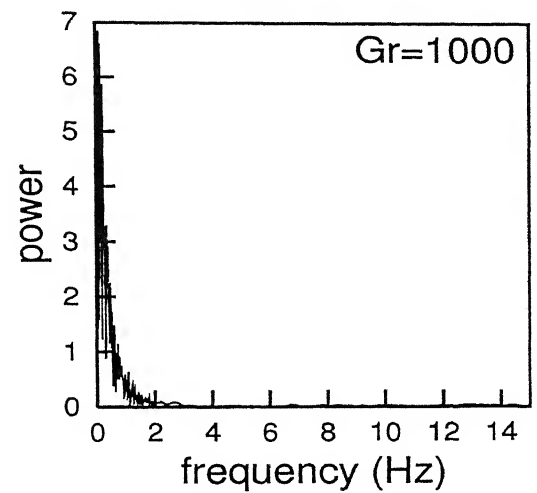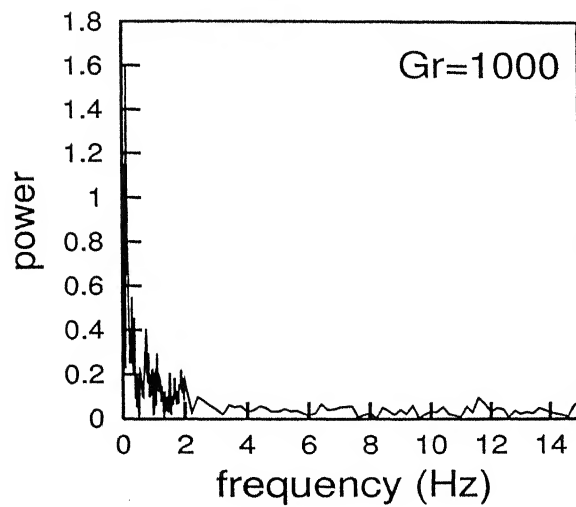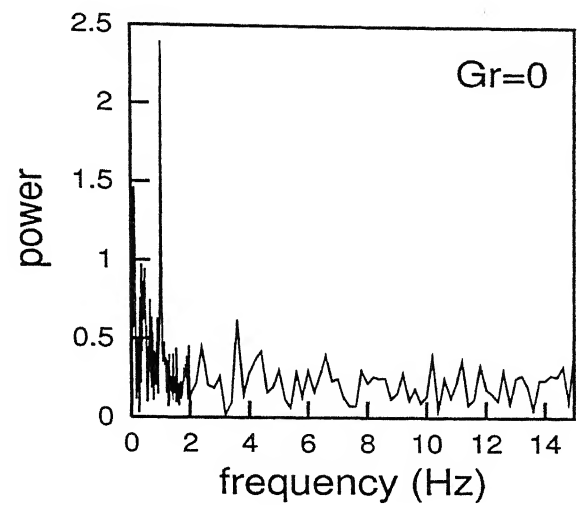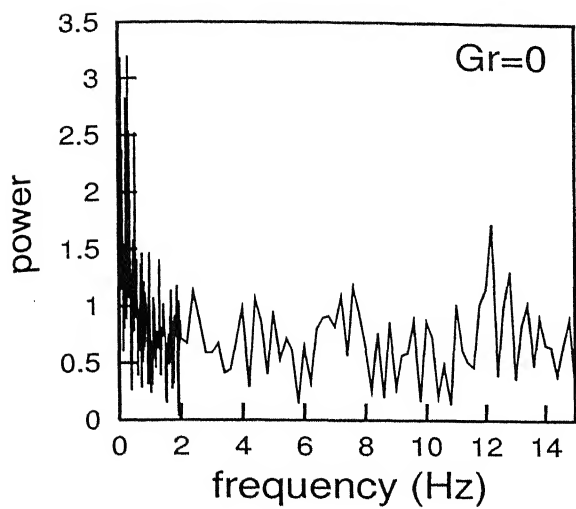
Figure 4.27: The power spectrum of photodiode signal at $y/d = 0.5$ and Gr=1300 with horizontal knife edge setting.

Figure 4.28: The power spectrum of photodiode signal at $y/d = 1.5$ and $x/d = 5$ for (a) Horizontal knife edge setting and (b) Vertical knife edge setting.

Chapter 5

Conclusions

The following conclusions have been arrived at in the present work.

1. For inclinations greater than 0, the points of separation move downstream, the wake size increases, but the separated shear layer rolls up over a shorter distance. These factors lead to a reduced drag coefficient and a higher Strouhal number.

2. The velocity fluctuations decay in the downstream direction. The decay rates depend on Reynolds number, but the role of the cylinder orientation is only secondary. The recovery of the time-averaged velocity components show a similar behaviour. However, the cross-correlation function $\overline{u'v'}$ strongly depends on the cylinder orientation, particularly at Re=4990 and 9980, before diminishing to zero along the wake centerline.

3. At $x= 5$, the spectra of both components of velocity are dominated by the contribution of the vortex shedding frequency. The peaks are sharper in the v-component and persist even at $x = 18$. The spectra at the lowest Reynolds number of 1340 show complex energetic interactions.

4. The wake size in both transverse and stream wise direction for the mixed convection is higher than that of the free convection.

5. The horizontal knife edge setting is more sensitive to transients than that of the vertical knife edge setting.

6. The wake for the mixed convection case is observed to be more stable than that of the free convection case, indicating the stabilizing effect of heating on the instability of the wake.

Bibliography

[1] Bearman, P.W. and Trueman, D.M., An investigation of the flow around rectangular cylinders, Aero. Q., Vol. 23, pp 229-237 (1972).

[2] Chew, Y.T. and Simpson, R.L., An explicit non-real time data reduction method of triple sensors hot-wire anemometer in three-dimensional flow, Trans. ASME, J. Fluid Engg., Vol.110, pp. 110-119 (1988).

[3] Collis, D.G. and Williums, J.J., Two-dimensional forced convection from cylinder at low Reynolds Numbers, J.Fluid Mech., Vol. 6, pp.357-384 (1959).

[4] Courchesne, J. and Laneville, A., A comparison of correction methods used in the evaluation of drag coefficient measurements for two dimensional rectangular cylinders, J. Fluids Engg., Trans ASME, Vol. 101, pp 506-510 (1979).

[5] Davis, R.W. and Moore, E.F., A numerical study of vortex shedding from rectangles, J. Fluid Mechanics, Vol. 116, pp 475-506 (1982).

[6] Franke, R., Rodi, W. and Schonugh, B., Numerical calculation of laminar vortex shedding flow past cylinders, J. Wind Engg. Ind. Aerodyn., Vol. 35, pp 237-257 (1990).

[7] Koch, F.A. and Gartshore, I.S., Temperature effects on hotwire anemometer calibration, Journal of Physics E:Sci.Instruments, Vol.5, pp. 58-61 (1970).

[8] Li, Guoping and Humphrey, Joesph, A.C., Numerical modelling of confined flow past a cylinder of square cross-section at various orientations, Int. J. Num. Meth. in Fluids, Vol. 20, pp 1215-1236 (1995).

[9] Igarashi, T., Fluid flow and heat transfer around rectangular cylinders (the case of a width/height/ ratio of a section of 0.33 - 1.5), Int. J. Heat and Mass Transfer, Vol. 30(5), pp 893-901 (1987).

[10] Kelkar, K.M. and Patankar, S.V., Numerical prediction of vortex shedding behind a square cylinder, Int. J. Num. Meth. Fluids, Vol. 14, pp 327-341 (1993).

[11] Knisely, C.W., Strouhal numbers of rectangular cylinders at incidence: a review and new data, J. Fluids Struct., Vol. 4, pp 371-393 (1990).

[12] Lyn, D.A., Einav, S., Rodi, W. and Park J.-H., A Laser-Doppler Velocimetry study of ensemble-averaged characteristics of turbulent near wake of a square cylinder, J. Fluid Mech., Vol.304, pp. 285-319 (1995).

[13] Nakaguchi, H., Hashimoto, K. and Muto, S., An experimental study of aerodynamic drag of rectangular cylinders, J. Japan Soc. Aero. Space Sci., Vol. 16, pp 1-5 (1968).

[14] Norberg, C., Flow around rectangular cylinders: pressure forces and wake frequencies, J. Wind Engng. Ind. Aerodyn., Vol. 49, pp 187-196 (1993).

[15] Okajima, A., Strouhal number of rectangular cylinders, J.Fluid Mechanics, vol 123, pp 379-398 (1982).

[16] Okajima, A., Nagahisa, T., and Rokugoh, A., A numerical analysis of flow around rectangular cylinders, JSME Int. J Series II, Vol. 33, pp 702-711 (1990).

[17] Saha, A.K., Muralidhar, K., and Biswas, G., Experimental study of flow past a square cylinder at high Reynolds numbers, Experiments in Fluids, Vol. 27, 12 pages (2000a).

[18] Saha, A.K., Muralidhar, K. and Biswas, G., Vortex structures and kinetic energy budget in two-dimensional flow past a square cylinder, Computers and Fluids, Vol. 29, pp 669-694, (2000b).

[19] Sohankar, A., Norberg, C., and Davidson, L., Low Reynolds number flow around a square cylinder at incidence: study of blockage, onset of vortex shedding and outlet boundary condition, Vol 26, pp 39-56 (1998).

[20] Swaminathan, M.K., Rankin, G.W., and Sridhar, K., Evaluation of the basic systems of equations for turbulence measurements using a Monte Carlo technique, J Fluid Mechanics, Vol. 170, pp 1-9 (1986).

[21] Townsend, A.A., The fully developed turbulent wake of a circular cylinder, Aust. J. Sci. Res., Vol. 2, pp 451-468 (1949).

[22] Williamson, C. H. K., Three-dimensional wake transition, J. Fluid Mech., Vol. 328, pp. 345-407 (1996).

[23] Ibers B.W. and Agarwal A.K., Schlieren analysis of an oscillating gas jet diffusion flame, Combustion and Flame, 119, pp 8494 (1999).

[24] Btater S.A, Honma H, Ivanov V.I, Koreeda J, Maeno K, Shugaev F.V, and Yanagisawa H., Density reconstruction from laser schlieren signal in shock tube experiments, Sockwaves, 8, pp. 183-189(1998).

[25] Davis M.R., Measurements in a subsonic turbulent jet using a quantitative schlieren technique". J. Fluid Mech., Vol.46, pp 631-656 (1971).

[26] Fu, S., and Wu, Y., Quantitative analysis of velocity distribution from schlieren images, 8th International Symposium on Flow Visualization, pp 233,1-233,5, (1998).

[27] Greenberg P.S, Klimek R.B. and Buchele R., Quantitative rainbow schlieren deflectometry, Applied Optics, Vol. 34 No. 192 pp. 3811-3822 (1995).

[28] Holder D.W, and North R.J., Schlieren methods, Notes on applied science, No. 31. London Her majesty's stationary office, (1963).

[29] Keun-Shik Chang and Jong-Youb Sa, The efect of buoyancy on vortex shedding in the near wake of a circular cylinder, J. Fluid Mechanics, Vol. 220, pp 253-266, (1990).

[30] Shenoy A.K, Agrawal A.K.and Gollanallic, S.R., Quantitative evaluation of flow computations by rainbow schlieren deflectometry, AIAA Journal, Vol. 36, No. 11, pp. 1953-1960 (1998).

[31] Tabei K. and Shirai H., Temperature and/or density measurements of asymmetrical flow fields by means of the moire-Schlieren Method, ISME International Journal, Vol. 33, No. 2, pp 249-255, (1990).

[32] Walton L. Howes, Rainbow Schlieren and its applications, Applied Optics, Vol. 23, No. 14, pp 2449-2460, (1984).

A 141973

A141973